Hybrid Organic/Inorganic Optical Upconversion Devices

by

Jun Chen

A thesis
presented to the University of Waterloo
in fulfillment of the
thesis requirement for the degree of
Doctor of Philosophy
in
Electrical and Computer Engineering

Waterloo, Ontario, Canada, 2011

AUTHOR'S DECLARATION

I hereby declare that I am the sole author of this thesis. This is a true copy of the thesis, including any required final revisions, as accepted by my examiners.

I understand that my thesis may be made electronically available to the public.

Abstract

The widely available charge coupled device (CCD) and lately CMOS imaging devices have created many applications on a mass scale. However these devices are limited to wavelengths shorter than about 1 μm. Hybrid photon upconversion devices have been developed recently. The end goal is to achieve an alternative technology for imaging in the 1.5-μm region. The hybrid upconversion idea relies on the integration of a photodetector and an organic light emitting diode (OLED). Under a forward bias for the OLED, the detected signal in the Photodetector is sent to the OLED, resulting in an increase in emission at a shorter wavelength and therefore achieving optical up conversion. An OLED device can simply consists of a stack of anode, a hole transport layer (HTL), a light-emitting layer, an electron transport layer (ETL), a cathode layer, and it typically emits visible light. As each organic molecule is a topologically perfect structure, the growth of each organic layer does not require "lattice matching", which has been the fundamental limit for inorganic semiconductor monolithic devices. Thus, integration of an OLED with a III–V compound semiconductor is a highly feasible and desirable approach for making low-cost, large-area, potentially high efficiency devices. This thesis addresses the physics, fabrication and characterization of hybrid near infrared optical upconverters and their imaging application.

Firstly, one novel hybrid optical upconverter structure is presented, which substantially improves the upconversion efficiency by embedding a metal mirror. Efficient carrier injection from the inorganic photodetector to the OLED is achieved by the insertion of a thin Au metal embedded mirror at the inorganic-organic interface. The upconversion efficiency was improved by more than 100%.

Secondly, the overall upconversion efficiency can be increased significantly, by introducing a gain mechanism into the Photodetector section of the upconverter. A promising option to implement gain is a heterojunction phototransistor (HPT). An InGaAs-InP HPT was integrated with an OLED, which converts 1.5-μm Infrared light to visible light with a built-in electrical gain (~94). The overall upconversion efficiency was improved to be 1.55 W/W.

Thirdly, this upconversion approach can also be used to realize a pixelless imaging device. A pixelless hybrid upconversion device consists of a large-area single-mesa device, where the OLED output is spatially correlated with the input 1.5-μm scene. Only the parts receiving incoming photons will emit output photons. To achieve this functionality, photon-generated carriers must flow mainly along the layer-growth direction when injected from the InGaAs light absorption layer into OLED

light emission layer. A prototype of pixelless imaging device based on an i-$In_{0.53}Ga_{0.47}As/C_{60}$ heterojunction was demonstrated, which minimized lateral current spreading.

This thesis presents experimental results of the first organic/inorganic hybrid optical amplifer and the first hybrid near infrared imaging device.

Acknowledgements

I would like to thank my supervisor Professor Dayan Ban for his guide, support and enthusiasm for this work. The personal lessons and professional research skills I have learned while working with him will be invaluable in all of my future endeavors. I would also like to thank all my committee members for their time, interest and suggestions: Professor Hany Aziz, Professor Siva Sivoththaman, Professor John Yeow and Professor Qiying Chen (Memorial University of Newfoundland). I want to thank the University of Waterloo, Waterloo Institute of Nanotechnology Fellowship and Chinese Government Award for Outstanding Self-financed Students Abroad for their financial support. In addition, I must thank some staff from the department: Annette Dietrich, Susan King, Laura Winger and Richard Barber for their help.

There are lots of collaborators who have contributed to my dissertation. I would like to thank Professor Zhenghong Lu, Michael G. Helander, Zhibin Wang at the University of Toronto for their contribution on organic layers research. I also thank Dr. Philips Poole at the National Research Council Canada for providing us very good quality wafers.

I would like to thank all of my present and former colleagues in Professor Dayan Ban's group: Saeed Fathololoumi, Marcel Graf, Somayyeh Rahimi, Sergey Musikhin, Ghasem Razavi, Rudra Dhar, Baolin Tian, Guocheng Liu, Jianchen Tao, Chao Xu, Zhenzhong Li and Hao Wang.

Finally, I would like to thank my family for their unconditional love and understanding. This thesis is dedicated to my parents, my wife and my incoming son.

Table of Contents

List of Figures

List of Tables

List of Abbreviations

NIR	Near infrared
MIR	Mid-infrared
FIR	Far-infrared
2D	Two-Dimensional
CCD	Charge-Coupled Device
CMOS	Complementary Metal-Oxide Semiconductor
SNR	Signal-to-Noise Ratio
FPA	Focal-Plane-Array
ROIC	Read-out Integrated Circuit
QWIP	Quantum Well Infared Photodetector
HPT	Heterojunction Phototransistor
LED	Light-Emitting Device
OLED	Organic Light-Emitting Device
MO	Molecular Orbital
AO	Atomic Orbital
HOMO	Highest Occupied Molecular Orbital
LUMO	Lowest Unoccupied Molecular Orbital
HTL	Hole Transport Layer
ETL	Electron Transport Layer
ITO	Indium Tin Oxide
HIL	Hole Injection Layer

Chapter 1
Introduction

1.1 Infrared Imaging

Since Sir Frederick William Herschel discovered the existence of infrared radiation in 1800, the world has witnessed a revolutionary change in people's consciousness of what infrared is and what benefits it brings us by using the technologies concerning infrared (IR). IR light lies between the visible and microwave regions of the electromagnetic spectrum. IR covers a wavelength range from 760 nm to 1 mm and can be divided further into three sub-ranges: near-infrared (NIR), mid-infrared (MIR) and far-infrared (FIR) as shown in Fig. 1.1. The IR range is of great interest because of their many potential applications. Among the big family of infrared products, infrared imaging represents the largest portion and enjoys the highest growth speed [1]. In terms of utilities, the infrared imaging device market can be divided into military and civil markets, from which many sub-markets are derived e.g. medical inspection, astronomy and aerospace research, surveillance, firefighting, construction, etc [2-5]. In developed countries, infrared imaging device has already been part of the equipment of land force, air force and navy. While there's also a huge need for those developing countries in pursue of the infrared imaging equipments. IR light is useful for these applications for three main reasons. First of all, the blackbody radiant emittance peaks in the IR wavelength range for temperatures $\geq$ room temperature (300 K). Secondly, due to its longer wavelength, IR light does not have the same scattering and absorption characteristics as visible light. Therefore, transparent windows in the atmosphere permit the transmission of IR light. Finally, different chemicals have infrared light absorption characteristics unique to their chemical structures [6]. However, widely-available charge coupled device (CCD) and lately CMOS imaging devices cannot be used in this range because the cut-off wavelength of these devices is only around 1 μm. The typical components of an IR camera system include optics for light collection, a focal plane array for detection and signal processing, and electronics for the digital display of IR images. The detector array converts incident IR light energy to electrical energy, while the silicon read-out circuit collects the detected signal (current or voltage) and performs initial, digital signal processing.

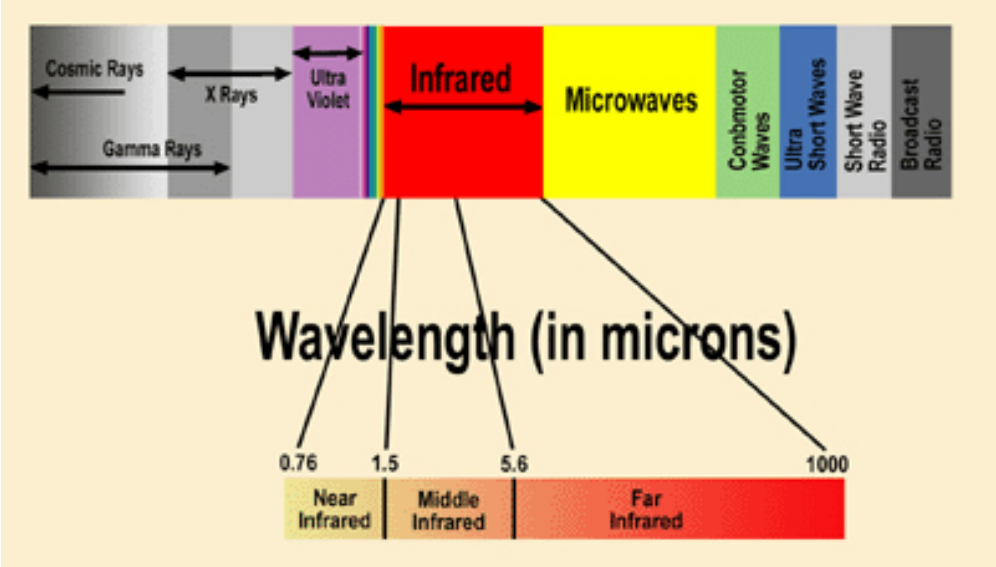

Figure 1.1 electromagnetic spectrum

1.2 Infrared Photodetectors

Infrared detectors perform the function of converting infrared electromagnetic radiation to a useful electrical signal. Depending on their basic operating principles, the various types of infrared detectors can be placed into two categories-thermal detectors and photodetectors (Table 1.1). Photodetectors are classified as opto-electronic devices due to their manipulation of electron-photon interactions, convert optical energy to electrical energy, enabling information transmission, light energy storage, and imaging. This energy conversion is possible due to the electronic bandstructure of bulk compound semiconductors, highlighted by the energy bandgap (E_g). The interaction between light and charge carriers is governed by quantum mechanics, as known as the photoelectric effect. The photons with energies greater than the bandgap can be absorbed to generate electron-hole pairs by raising an electron from the valence band to the conduction band, leaving a hole behind. Photodetectors can be further classified into photoconductive detectors (Fig. 1.2) and photovoltaic detector (Fig. 1.3) [7]. Photovoltaic detectors, also called photodiodes, are made by utilizing a semiconductor *p-n* junction as active region. This device can convert the input radiation into a current or voltage output. While, photoconductive detectors detect infrared radiation by changing their corresponding resistance.

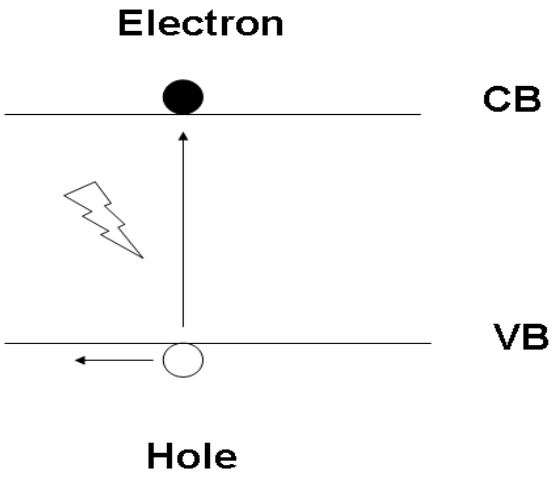

Figure 1.2 Photoconductive-light increases the flow of electrons and reduces the resistance

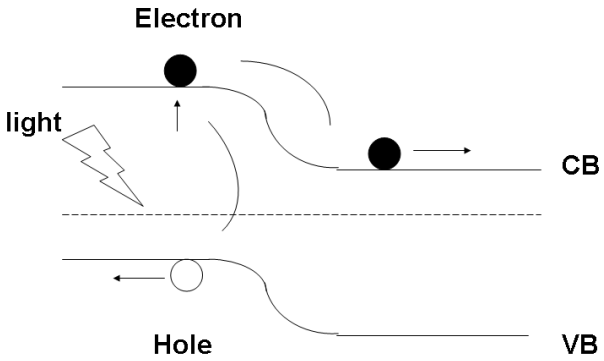

Figure 1.3 Band diagram of a photovoltaic device: photon-generated electrons/holes move between layers, producing a voltage difference at two terminals.

In the detector's history, PbS was the first to be successfully demonstrated with IR sensitivity out to 3 μm in 1940's. Later, silicon became the dominant material in the semiconductor industry mostly because its stable natural oxide is a nearly perfect insulator and enables complex processing. Silicon detectors have also been widely used in the visible and NIR region below 1 μm. It was well known that detectors with very high performance can be fabricated from Si, Ge, GaAs, InSb, InGaAs and HgCdTe [8-10]. Inherent bandgap engineering techniques in compound semiconductor device technology make semiconductor IR detectors superior for many applications. For example, $In_xGa_{1-x}As$ detectors can cover a wide range from 700nm to 3μm by changing the composition from gallium-rich ($x<0.5$) to indium-rich ($x>0.5$). P-i-n (three regions corresponding to p-type doped, intrinsic and n-type doped) photodiodes, MSM (metal-semiconductor-metal) detectors and bipolar phototransistors

are three examples of the wide-range of detector families featuring easy fabrication processes and high performance for particular applications. However, the low bandgap materials appropriate for IR detection are inherently soft and brittle since the corresponding lattice constants are large (indicating weak atomic bonds within the crystalline lattice).Thus, it can be difficult to epitaxially grow and fabricate IR devices with bulk materials active regions. In addition, intrinsic IR photodetectors have limited applicability in the long-wavelength and far IR ranges (≥ 8 μm). In this case, many more options for extending the IR detection ranges of compound semiconductor exist by taking advantages of extrinsic detection schemes. In this case, the detection light wavelength does not correspond to the bandgap energy of the active region ($\hbar\varpi < E_g$). One example of an extrinsic scheme is to detect IR light through absorption from energy levels within the bandgap of the bulk active region. Another method for extrinsic detection is to reduce the dimensionality of the photodetector active region so that intraband photogeneration is possible. Heterostructures confined in one dimension are called quantum wells (QWs), The QW energy levels are occupied with electron through doping. Incident IR radiation excites these localized carriers so that intraband transitions can occur within QWs. For an extrinsic detection scheme using a quantum-confined active region, IR photons with energies equal to the separation between discrete energy levels in a single energy band are absorbed. The photoexcited carriers change the total current flowing through the device.

Table 1.1 Infrared photodetector technology comparison

	Thermal detectors	Photo detectors
Example	Microbolometer, thermopile	Quantum-well detectors
cost	cheap	expensive
Spectral band	Broad	narrow
sensitivity	weak	strong
resolution	low	high
mechanism	Change of capacitance or resistance of materials caused by incident radiation energy	Change of state of electrons in a crystal structure reacting to incident photons
Cooling	no	Mostly required

1.3 Infrared Upconversion

Nowadays, the Focal-plane-array (FPA) system is the most widely used infrared imaging technology. A FPA detector is any detector that has more than one row of detectors. The cooled infrared focal plane arrays benefit from cooling to help mitigate dark current in order to boost the signal to noise ratio (SNR) thus increasing performance and effective standoff range. The industry standard for NIR imaging is based on a FPA in which two-dimensional (2D) InGaAs/InP photodetector pixels interconnected with 2D silicon read-out integrated circuit (ROIC) pixels using indium bump technology (Fig. 1.4). The InGaAs Photodetector and the Si ROIC are grown on different substrates and fabricated into pixel-based devices in separate processes. The photondetection unit (InGaAs Photodetector) and the signal processing unit (Si ROIC) need to be integrated in such a way that the electrodes of the InGaAs Photodetector pixels and the Si ROIC pixels are connected through micrometer-size indium bumps. This indium bump technology is a “one-piece-at-a-time” process and there are many factors that limit its yield and size-scalability. In addition, to fabricate large-area/scale pixel arrays, the size of each individual pixel has to be reduced, imposing stringent requirements on device fabrication. The pixel-based design and indium-bump technology are inherently disadvantageous in terms of device size scalability and lowering manufacture cost.

Because of the limitations of the current infrared imaging device, photon upconversion devices have been developed for several years. The end goal is to achieve an alternative technology for imaging in the 1.5-μm region. There are two main upconversion mechanisms: nonlinear optical process and linear optical process. The nonlinear optical process requires two or more metastable energy states to store the energy of absorbed pump photons. The combined energies of pump photons can lead to the emission of a higher energy photon. Scientists have been doing research on this field for many years to investigate the energy transfer process and fascinating optical phenomenon that occur during an upconversion event, like rare earth-doped bulk phosphors, infrared quantum counters and spectral converters for solar cells [11-12]. This research mainly focuses on the linear optical upconversion. This upconversion idea relies on the integration of a Photodetector and a light-emitting device (LED). The two device components are serially connected. Under a forward bias for the LED, the detected signal in the photo detector is sent to the LED, resulting in an increase in optical emission at a shorter wavelength and therefore achieving optical upconversion. This idea was employed to convert long-wavelength infrared light to near infrared light by Quantum Well Infrared photodetectors (QWIPs) with GaAs-based LEDs (Fig. 1.5) [13].

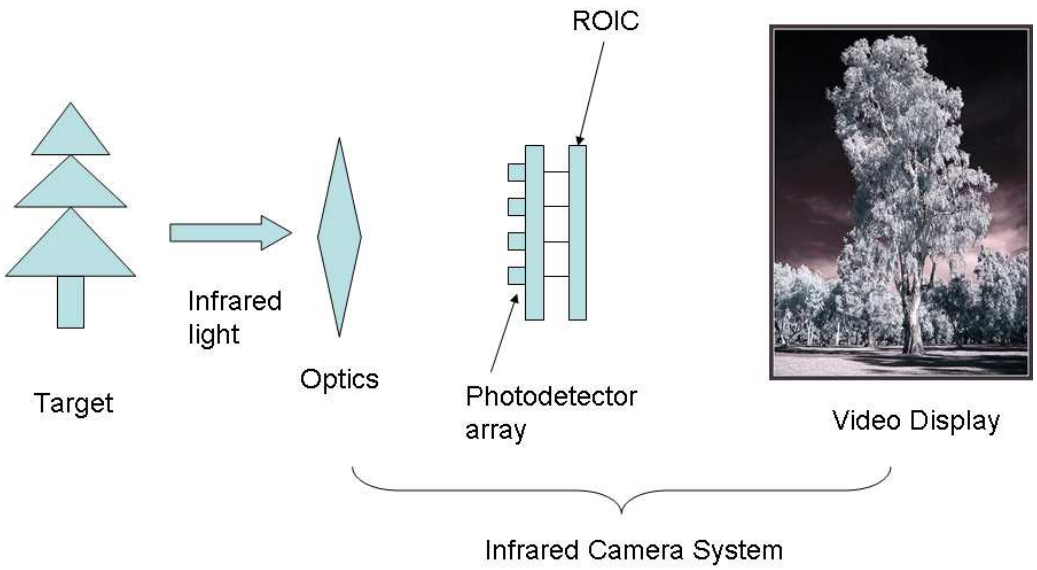

Figure 1.4 Schematic diagram of a typical infrared camera system showing its components

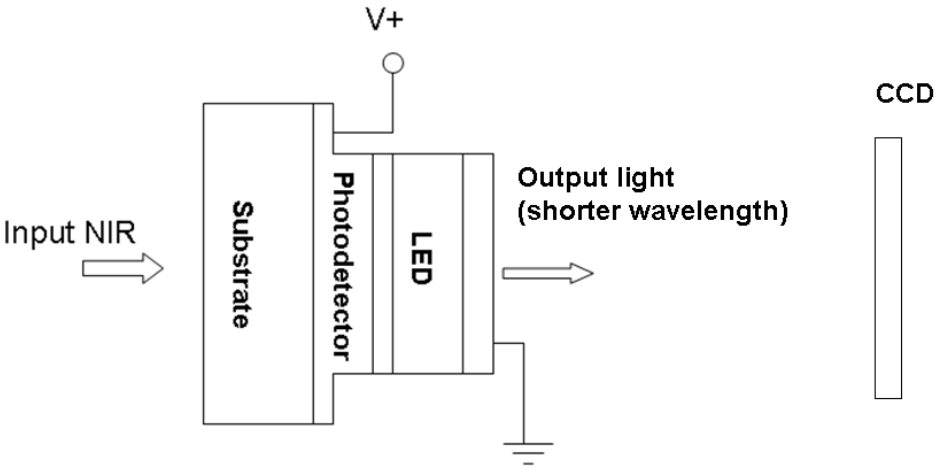

Figure 1.5 Large –area mesa device and a CCD are shown for the device geometry

Liu et al first proposed the concept of optical upconversion device in 1995. Instead of meeting stringent fabrication requirements of indium bump technology and FPA, Liu made use of existed QWIP and LED. As long as the lattice constants of their constituent materials match with each other, a QWIP and a LED can be integrated via direct epitaxial growth integration. Unlike common p-i-n photodetectors, the photon absorption in a QWIP is based on intersubband transition in which electrons are excited from a lower conduction intersubband to a higher intersubband, and the energy

separation of those intersubbands is much smaller than the bandgap of the constituent materials. The narrower energy jumping intersubband transition therefore enables photodetecting for MIR or even FIR. As illustrated in Fig. 1.6, Liu et al took advantage of such property of a QWIP, and integrated it with a LED in series. They chose GaAs/$Al_{0.25}Ga_{0.75}As$ for the QWIP, and InGaAs/GaAs for the LED, and successfully demonstrated upconversion with their device from MIR(~ 9.2 μm) to NIR(~ 927 nm) at around 80K. They improved the LED performance by making the substrate thinner. Their QWIP/LED upconverter was able to detect an incoming light even at an illumination power as low as 1.5 μW. Though the functionality of QWIP/LED upconverter was realized, the overall performance was not very satisfactory. By comparing the output photons per second and input photons per second, Liu et al obtained an external upconversion efficiency of only 0.8%. One main reason for such a low efficiency was the low extraction efficiency of the LED at the air/LED interface due to large refractive index of mismatch. Another reason was the metal ring contact at top blocked 50% outgoing photons. In addition, though the low operation temperature promoted the internal quantum efficiency of InGaAs/GaAs LED to almost 100%, the low operation temperature also limited the applicability of the device.

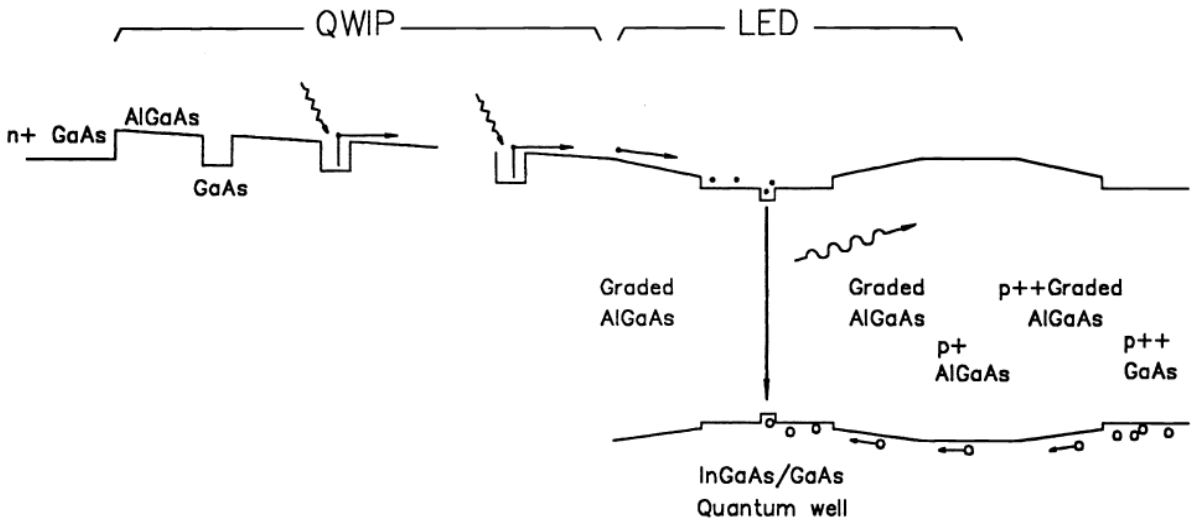

Figure 1.6 Bandgap profile of the proposed integrated QWIP and LED [13].

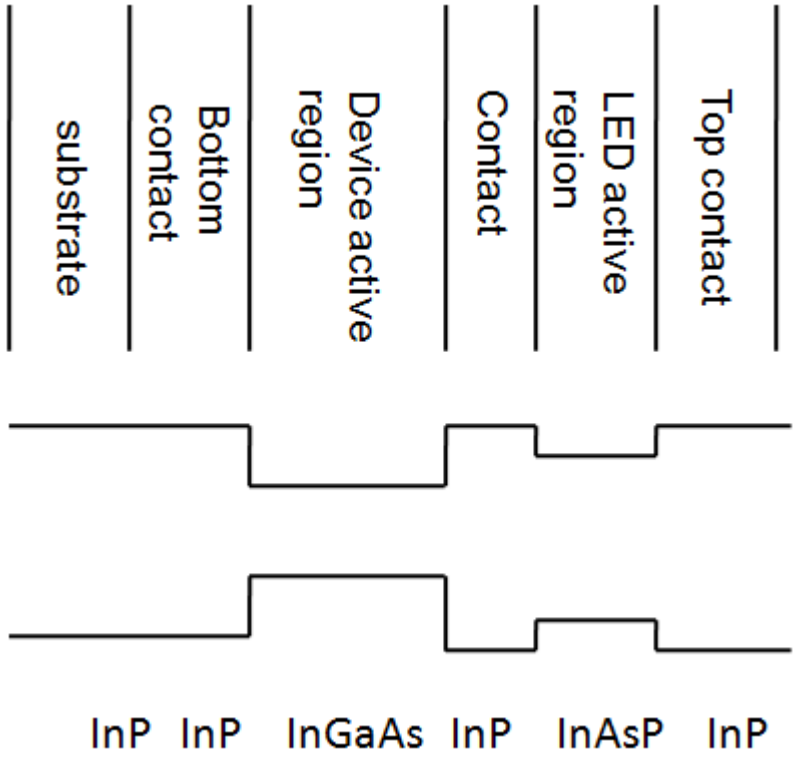

Figure 1.7 Schematic layer structure and band-edge profile of device [14].

In addition to QWIP/LED, NIR upconverters based on the NIR Photodetector/LED are also developed, which is composed of a LED and a narrow bandgap photodetector. NIR Photodetectors using interband transition of narrow bandgap semiconductor materials are much more efficient than their counterparts based on intersubband transition. In the NIR region, InGaAs is the best developed among all III-V compounds. Besides, they can work at room temperature. In 2000, Liu et al reported an optical upconverter, which integrated an $In_{0.53}Ga_{0.47}As$/InP Photodetector with $InAs_{0.1}P_{0.9}$/InP LED, and all layers are directly epitaxially grown on one InP substrate [14]. This upconverter could convert light from 1.5 μm to 1 μm. For all these types of devices, the structures are p-i-n $In_{0.53}Ga_{0.47}As$/InP, which have a very high near-infrared photoresponsivity of 0.5-1.0 A/W (depending on the thickness of the absorption layer and anti-reflection coating). However, the internal quantum efficiency of the

LED is less than 1%. In monolithic devices created by direct epitaxial growth, the bandgap difference between the active region of a LED and the active region of the photodetector is highly restricted due to the stringent lattice-matching requirements imposed by the uninterrupted epitaxial growth of the various layers in the devices. This results in low efficiency and limited range of upconversion from 1.5 μm to 1.0 μm. The upconversion range and quantum efficiency are improved when wafer fusion technology is employed for monolithic integration. For example, monolithic converters created by wafer-fusing a GaAs/AlGaAs LED with an $In_{0.53}Ga_{0.47}As$/InP photodetector can upconvert light from 1.5 to 0.87 μm(Fig. 1.8) [15].

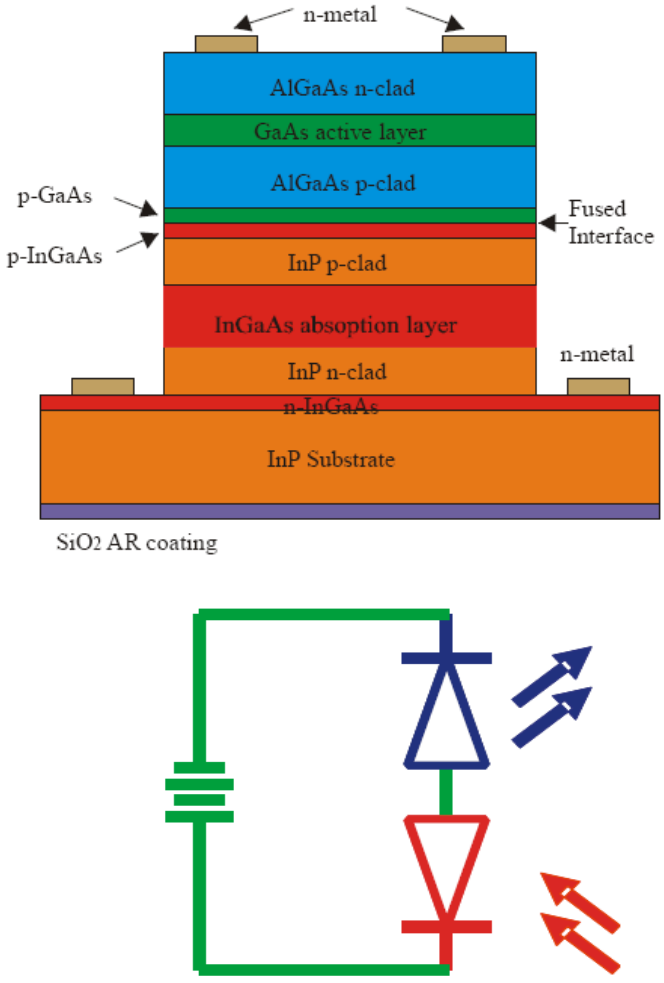

Figure 1.8 Schematic cross section of wafer-bonded p-i-n/LED upconversion device and device operation principle [15].

1.4 Infrared Pixelless Imaging

Soon after the demonstration of upconversion, it was discovered that the output and input images were spatially correlated. As a result, an imaging array consisting of a large number of separated pixels may be replaced by one large-area single-mesa device for achieving the same functionality. Since then significant progress has been made and pixelless imaging has been demonstrated for incoming light with wavelength between 5 to 12 μm. In 1997, pixelless MIR upconversion imaging based on a p-type QWIP-LED upconversion device was demonstrated. For the initial experiment to show the concept, image of a 1000K hot object was captured, shown in Fig. 1.9 [16]. The challenges in pursuit of pixelless upconversion imaging are twofolds: suppressing the lateral carrier diffusion in the common region while preserving effective electrical interconnection between the two constituent components. While there has been much progress in NIR Photodetector-LED upconversion devices, the first 1.5 μm NIR upconversion imaging was not demonstrated until 2004. Due to electric interconnection requirements, the common region between the photodetector and LED components was simply heavily p-doped. This resulted in significant carrier lateral diffusion and no pixelless imaging operation was observed. As such, the layer structures and doping profiles of pixelless upconversion imaging device should be designed carefully. H. Luo et al adopted a three-layer structure (undoped-doped-undoped) in the common region, which minimized the carrier lateral diffusion as well as provided adequate electrical interconnection (Fig. 1.10 (a)) [2]. Another approach is to integrate the photodetector and the LED via wafer fusion. Two wafers were designed and grown with carefully designed doping profiles for the purpose of suppressing lateral carrier diffusion in the common region to achieve pixelless imaging operation(Fig. 1.10(b)) [5]. The upconversion imaging test system consists of an upconversion device which transforms the incoming longer wavelength signal into an outgoing shorter wavelength emission and a conventional CCD camera which captures the emission image.

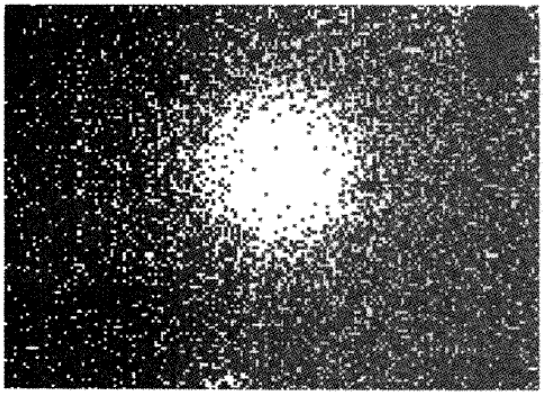

Figure 1.9 1mm-diameter blackbody source imaged by large-area (4× 3 mm^2) QWIP-LED device together with CCD camera [16].

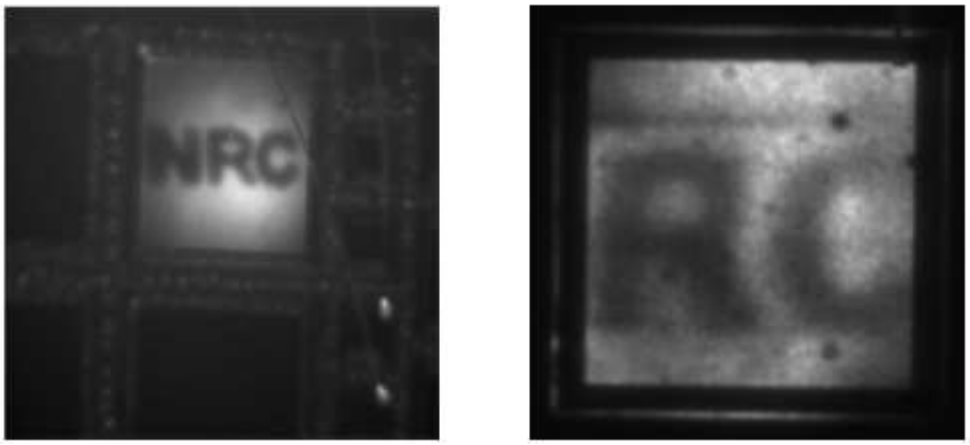

(a) (b)

Figure 1.10 (a) CCD image of letters “NRC” using Luo’s pixelless upconversion device with at room temperature. The mesa device is 1.5 × 1.5 mm^2 in size and the device was biased at -3 V at room temperature [2]. (b) CCD image of letters “RC” using pixelless upconversion device via wafer fusion (1.0×1.0 mm^2 in size). The device was biased at 1.5 V at room temperature [5].

1.5 Operation Principle of Infrared Upconverters

A linear photon upconversion device is fabricated by integrating a Photodetector with a LED in series. Since in most cases the photodetectors and light emitting devices are p-i-n heterojunctions, the whole upconversion device can be regarded as two back to back p-i-n devices. When in operation, external bias is applied on the devices, with which the photodetector is reversely biased, and the light

emitting diode is forward biased. Therefore, the optical-electrical-optical process is turned on within the upconverter, leading to the infrared light upconversion.

1.5.1 Photodetector

The optical-electrical process takes place within a photodiode. A photodiode has a depleted semiconductor region with a high electric field that serves to separate photo-generated electron-hole pairs. The p-i-n photodiode typically consists of three layers, one intrinsic layer sandwiched by one n-doped layer and one p-doped layer. The intrinsic layer is also called absorption/active layer because most of the optical absorption process happens in this layer, and the bandgap of the intrinsic layer hence determines the absorption wavelength, and the thickness of the intrinsic layer is intentionally designed much larger than that of the n-doped and p-doped layers so as to maximize the absorption of incoming photons. In addition, compared with the intrinsic layer, the n-doped and p-doped layers are made of a different material with a wider bandgap so that they will not absorb the incoming photons of desired upconverting wavelength. However, the bandgap difference between layers cannot be too large, since it has to make sure the excited carriers will not be confined by the energetic barrier due to the bandgap difference, and can be successfully injected to the light emitting diode.

Usually, the photodetector internal quantum efficiency, defined as the ratio of excited electron number and incoming photon number, is used to characterize the performance of a photodetector, which with measured power of incoming light and outgoing current can be calculated by

$$\eta_{\text{int}} = \left(I_p / e\right) / \left(P_{opt} / h\nu\right) \qquad (1.1)$$

where I_p is the photogenerated current by the absorption of incident optical power P_{opt} at a wavelength λ (corresponding to a photon energy $h\nu$). On the other hand, the photon absorption efficiency of a p-i-n photodetector, can be calculated by

$$\eta_{abs} = (1-R)(1-e^{-\alpha d}) \qquad (1.2)$$

where R the reflectance at the air/photodetector interface, α the material absorption coefficient decided by doping profile and light frequency, d the absorption layer thickness. $(1-R)$ gives the percentage of photons injected from outside to the photodetector, and $(1-e^{-\alpha d})$ gives the ratio of absorbed photon number over injected photon number. Since it is normally assumed the number of absorbed photons is equal to the number of excited electrons, the multiplication of the two terms yields the photon conversion efficiency. Combining equations (1.1) and (1.2), the output photocurrent can then be calculated by

$$I_p = \eta_{abs}\eta_{\text{int}}(\frac{P}{h\nu})e = (1-R)(1-e^{-\alpha d})\eta_{\text{int}}(\frac{P}{h\nu})e \quad (1.3)$$

Moreover, a related figure of merit is the responsivity, which is the ratio of the photocurrent to the optical power, in a unit A/W. From equation (1.3), we have

$$\text{Responsivity} = (1-R)(1-e^{-\alpha d})\eta_{\text{int}}\frac{e\lambda_{in}}{hc} \quad (1.4)$$

1.5.2 Light Emitting Diodes

In addition to optical-electrical process, the electrical-optical process is equally important, which occurs in the LED part. For a LED, the structure is basically a three-layer p-i-n heterojunction. The middle intrinsic layer has a narrower bandgap, compared to the p-doped and n-doped layers, As a result, injected electrons and holes are confined in the middle intrinsic layer and are expected to recombine to emit photons at the desired wavelength. Since most of electrical-optical process takes place in the middle layer, such intrinsic layer is also called as active layer for the LED.

The performance of a LED is mainly determined by the following processes: the current injection into the active layer of LED, the conversion from electrons to photons, and photon escaping out of the device. The engineers have defined the following parameters to address the above processes, current injection efficiency, η_{inj}, representing the percentage of electrons effectively injected into the LED; internal quantum efficiency, η_{int} the percentage of injected electrons that lead to photon emission; and light-escape probability, η_c, the percentage of photons finally escaping out of the device and to be seen by the observers. The common quantity to measure LED overall performance is the external quantum efficiency, which is defined as the ratio of output light power vs. the input photocurrent, in the unit W/A:

$$\eta_{ext} = \frac{P_{out}}{I_p} = \frac{\#\,photons}{\#\,electrons} \bullet \frac{h\nu}{e} = \eta_{inj}\eta_{\text{int}}\eta_c\frac{h\nu}{e} \quad (1.5)$$

Where P_{out} is the optical output power, and I_p is the injection current, Here the product of η_{inj}, η_{int} and η_c gives the ratio of output photons over injected electrons.

The light-escape probability is closely related to the material used for the air/LED interface, which can be approximately calculated by

$$\eta_c = \frac{1}{4}(\sin\theta_c)^2(1-(\frac{n_s-1}{n_s+1})^2) = \frac{1}{4}(\frac{1}{n_s})^2(1-(\frac{n_s-1}{n_s+1})^2) \quad (1.6)$$

Where θ_c is the critical angle at the semiconductor-air interface, beyond which the total internal reflection is observed, and n_s is the refractive index of semiconductor [4].

1.5.3 Upconversion Efficiency

The upconversion efficiency of the device, which is defined as the ratio of output optical power over input optical power and has a unit of W/W, is strongly affected by internal key processes such as photon absorption, photo-carrier generation, photo-carrier transport and injection, and photon emission. In an optical upconverter without any electrical gain mechanisms, the upconversion efficiency (η_{total}) is determined by the following equations:

$$\eta_{total} = R_{responsivity} \bullet \eta_{ext} = ((1-R)(1-e^{-\alpha d})\eta_{\text{int}-PD}\frac{e\lambda_{in}}{hc}) \bullet (\eta_{inj}\eta_{\text{int}-LED}\eta_c\frac{hv_{out}}{e})$$
$$= (1-R)(1-e^{-\alpha d})\frac{\lambda_{in}}{\lambda_{out}}\eta_{inj}(\eta_{\text{int}-PD}\eta_{\text{int}-LED})\eta_c \quad (1.7)$$

where hv_{out} is the photon energy of output light.

Chapter 2
Hybrid Optical Upconversion Devices

2.1 Organic Semiconductor

Organic electronic and optoelectronic devices have attracted intensive interests in recent years because of the flexibility of depositing organic films on various substrates and the relative ease of processing of organic compounds that are being engineered in numerous research labs. Significant progress has been made in realizing different functions by using organic materials for low-cost devices, such as organic field-effect transistors, organic light-emitting diodes (OLED) and displays, and thin film organic photovoltaic cells, to name a few. OLED technology is one of the most exciting applications of organic semiconductor in opto-electronics. To facilitate the discussion of the working mechanism of an OLED, one must first understand the electronic structure of an organic semiconductor. Organic semiconductors have different bonding systems from conventional inorganic semiconductors, so they operate in a fundamentally different way. Conventional semiconductors are held together by strong covalent bonds that extend three-dimensionally, resulting in electronic bands that give rise to its semiconducting properties. Organic materials have similar intramolecular (within a molecule) covalent bonds but are held together only by weak intermolecular (between molecules) van der Waals interactions. The electronic wave function is thus strongly localized to individual molecules, and the weak intermolecular interactions instigate a narrow electronic bandwidth formed in molecular solids. These molecules have molecular orbitals (MOs) formed from the linear combination of their constituent atomic orbitals (AOs) [17]. However, due to the conservation of the total number of interacting orbitals, for every resultant MO (bonding) that has lower energy than the interacting AOs, there is an corresponding antibonding MO of a higher energy. These molecular orbitals can be classified as σ bonds, π bonds, or δ bonds, with the former two being mostly encountered in organic semiconductors. A σ bond is formed along the bond axis between two nuclei, whereas a π bond is formed on either side of the internuclear axis by the sideway overlapping of the p orbitals (Fig. 2.1). When a C atom is attached to 3 groups, so it is involved in 3 σ bonds, this requires the 3 orbitals in hybrid set (sp2-hybridzation).

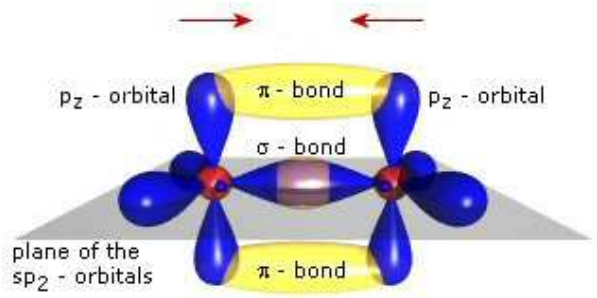

Figure 2.1 Scheme of the orbitals of two sp2-hybridised carbon atoms [18]

The energy distribution of these bonds in benzene molecule is symmetric with respect to the energy of the original AOs before they interact. For example, there will be three π bonds, each filled with a pair of electrons, below the energy of the original AOs; and three π* bonds void of electrons with energy above the original AOs, as shown in Fig. 2.2. The MO into which the last π electron fills is called the highest occupied molecular orbital (HOMO) and the next MO up in energy level is called the lowest unoccupied molecular orbital (LUMO). If carbon atoms form larger molecules, typically with benzene rings as the basic unit, the π-bonds become delocalized and form a π-system which often has the extensions of the molecule. The gap between occupied and empty states in these π-systems becomes smaller with increasing delocalization, leading to absorption and fluorescence in the visible.

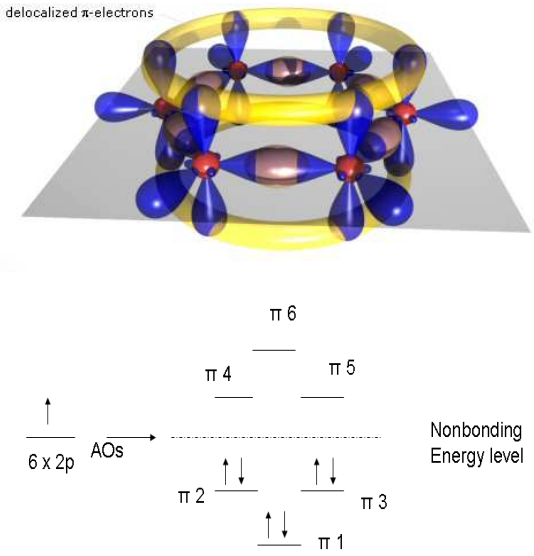

Figure 2.2 Orbital and energy diagrams of a benzene ring [18]

Different from inorganic semiconductors, organic semiconductors do not have strong intermolecular forces because the molecules are bonded by weak van der Waals forces. Therefore, the electronic structures of organic semiconductors are based on discrete molecular orbitals rather than on extended energy bands. As a result, the transport of charge within organic semiconductor relies on the transport across the discrete molecular orbitals of each molecule. Due to the large intermolecular distance, overlap between molecular wavefunctions is insignificant (i.e. no band formation). Intermolecular electron transport proceeds by jumping (hopping) from one molecule to the next over an energy barrier ΔE. This barrier is caused by the intermolecular separation and self-induced polaronic effect. This mechanism involves a chain of electric field driven redox processes where the electron and the hole are exchanged between the neutral molecules and the anion or cation radicals. When the cation and the anion radicals "hop" to the vicinity of each other, the electron and the hole recombine to form an electron-hole pair called Frenkel exciton [19]. The radius of a Frenkel exciton is comparable to the size of the molecule (typically < 0.5 nm), or is smaller than the intermolecular distance. Because of the relatively smaller dielectric constant for organic materials, the Coulomb interaction between the electron and hole is very strong [20]. In contrast, with the much larger dielectric constant in traditional inorganic semiconductors, a significant potential overlap between neighboring lattice points in such materials tends to reduce the Coulomb interaction between the electron-hole pair, resulting in a much larger-radius Mott-Wannier exciton (4-10 nm) that is many times the size of the lattice constant. To compare, a Mott-Wannier exciton usually has binding energy ~10meV [21], whereas that of a Frenkel exciton can be as large as 1eV.

2.2 OLED Working Mechanism

An OLED is a light emitting device composed of several organic semiconductor layers sandwiched between electrodes. The first organic electroluminescence phenomenon was discovered by Pope in 1963 [22]. He applied bias with a magnitude of several hundred volts to Anthracene crystal. About twenty years later, C.W. Tang et al invented the first practical OLED device in 1987 [23]. They incorporated two small molecule organic layers between a metal cathode and a transparent ITO anode. The low driving voltage of less than 10V required to achieve a brightness of above 1000 cd/m^2 provided OLED with great commercialization potential. Ever since then, great research interest has been driven by its promising application in lighting systems and thin film displays. Some of cutting-edge research focuses on the lifetime improvement of OLED display, which can pave the way for wide commercialization of OLED displays [24-25]. An typical OLED device consists of a

simple stack of an anode, a hole transport layer (HTL), a light-emitting layer, an electron transport layer (ETL) and a cathode layer. Since there is no intrinsic charge carrier in organic semiconductors, electrons and holes need to be injected into the device from the cathode and anode, respectively (Fig. 2.3). When an electrical bias is applied between the two electrodes, injected electrons and holes migrate toward the oppositely charged electrode and recombine in the light-emitting layer to form excitons, whose energy is then released in the form of light.

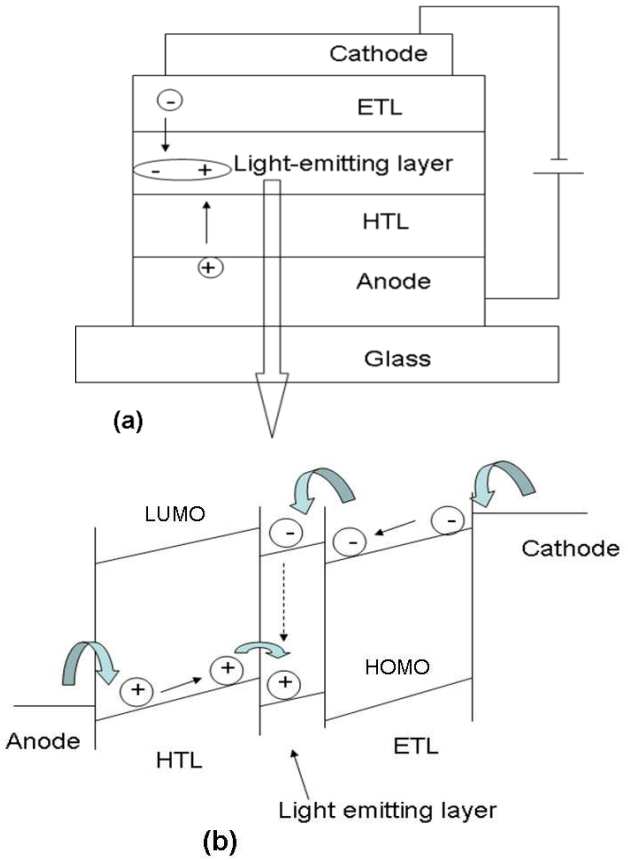

Figure 2.3 (a) Schematic diagram of OLED structure. (b) Energy diagram of a OLED

From the working mechanism discussed above, we see that the interface between each layer is very crucial to carrier injection and transport, and consequently to the device performance. To modify the interface and assist carrier injection from the electrodes, the three layers based device structure has evolved into a multilayer structure as shown (Fig. 2.4). A hole injection layer (HIL) is inserted to reduce the hole injection barrier between the anode Indium tin oxide (ITO) and HTL interface. The HIL's HOMO lays between the work function of ITO and the HOMO of HTL. Copper phthalocyanine (CuPc) is one of most widely used HIL to promote hole injection [26]. To match the

LUMO of ETL, metal with low work function is desirable. LiF/Al bilayer cathode is currently the most commonly used cathode structure. The underlying mechanisms for improved electron injection are still under investigation [27-28].

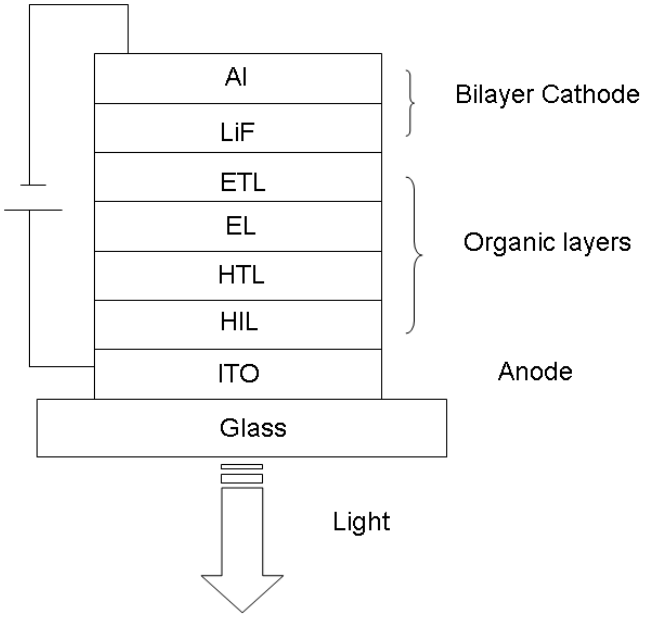

Figure 2.4 A schematic drawing of a multilayered OLED device structure, HIL is inserted to reduce the hole injection barrier between the anode Indium tin oxide (ITO) and HTL interface. EL is light-emitting layer and ETL is electron transport layer, respectively. LiF/Al bilayer cathode is currently the most commonly used cathode structure.

2.3 Organic Photodetector-LED Upconverters

Organic optoelectronic devices have been developing rapidly, and also have been applied for NIR up-conversion. Organic optoelectronic devices are appropriate for NIR up-conversion due to two reasons. Firstly, they can be flexibly disposed on various substrates with ease. One fundamental limitation of semiconductor optoelectronic devices is the need for lattice match between different layers. For example, an InGaAs/InP Photodetector has different a lattice constant from that of a GaAs/AlGaAs LED, making it impossible to grow them on top of each other. In contrast to standard semiconductor devices, every organic optoelectronic molecular is a topologically perfect structure. The fabrication process can be simplified, and the cost can be reduced. Secondly, the emission

wavelength of OLED can be easily tuned to cover the NIR and visible region, while a GaAs or InP based LED can only emit NIR.

All organic upconversion devices can be realized by integrating an OLED with an organic Photodetector. Yase et al reported fluorescent OLEDs with titanyl phthalocyanine (TiPc) as a photosensitive hole injection layer exhibited NIR-to-blue as well as red-to-green upconversion [29-30]. However, the devices showed very low photon-to-photon conversion efficiencies, typically less than 0.05%. The low conversion efficiencies were due to the low efficiency OLEDs as well as low efficiency photodetectors. More recently, Kim et al from the University of Florida has improved all-organic up-conversion devices by integrating a fac-tris(2-phenylpyridinato)iridium(III) (Irppy3) phosphorescent OLED and a tin phthalocyanine (SnPc):C_{60} bulk heterostructure NIR photodetector [Fig.2.5]. Compared to the earlier devices, these devices showed a significantly higher photon-to-photon conversion efficiency due to the high efficiency phosphorescent OLEDs used in the devices. However, neither small molecular nor polymers with low bandgaps are currently available for the manufacture of efficient photodiode in the spectral region above 1 μm, and the maximum reported upconversion efficiency of the organic NIR upconversion device was only 2.7 % under 830 nm infrared light illumination [32].

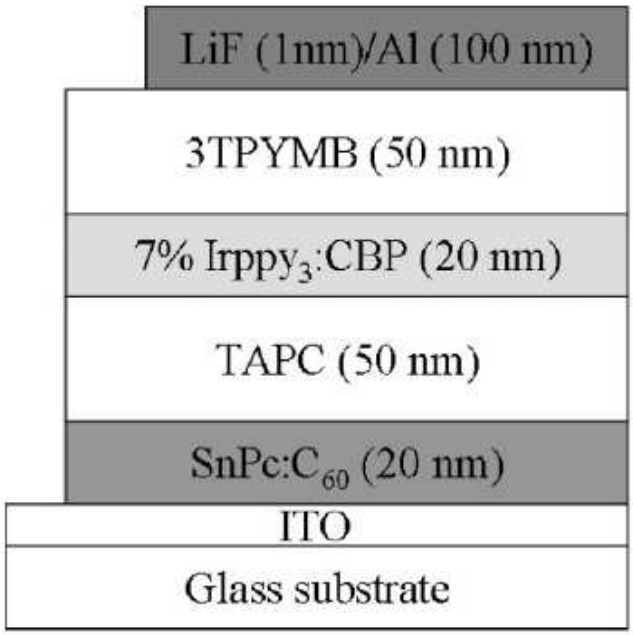

Figure 2.5 Schematic cross-section view of the IR-to-green light upconversion device [31]

2.4 Organic-Inorganic Hybridization

The hetero-integration of organic materials with inorganic functional substrates has yet to be demonstrated to achieve multiple functions from a single device, which could greatly enhance the technological impact of organ-electronics and potentially open up new areas of the applications for organic materials and devices [33-37].

Organic-inorganic materials also enable the integration of useful organic and inorganic characteristics within a single molecular-scale composite. The flexibility of organic chemistry enables the formation of organic molecules with useful luminescent and conducting properties. Inorganic materials enable the design of materials with better thermal/mechanical stability and higher electrical mobility, as a result of the stronger covalent and ionic bonding. OLED emission wavelength can be easily varied across the entire visible spectrum by utilizing different emissive organic materials. Hybrid organic and inorganic materials have been synthesized and fabricated to devices in the past. Thus exploiting the tremendous progress in OLEDs and integrating OLED on a III-V compound semiconductor becomes a highly feasible and desirable approach for making low-cost, large-area and potentially high-efficiency devices.

In these hybrid electronic and optoelectronic devices, the carrier transport process and energy transfer between the organic and inorganic materials play a vital role in enabling the integration of functioning units. Thus, the elucidation of the interfacial electronic structure is of crucial importance to the understanding and improvement of hybrid devices. X-ray photoelectron spectroscopy (XPS) and ultraviolet photoelectron spectroscopy (UPS) are both surface sensitive techniques best suited for the study of interfacial electronic structures. For example, the C_{60} /InP (001) interface formation and energy band diagram has been studied by a number of surface sensitive techniques [37].

2.5 Hybrid Organic-Inorganic Optical Upconverter

2.5.1 Device Structure

In 1995, Liu et al successfully realized NIR upconversion through direct epitaxial integration, which grew epitaxially an $InAs_{0.1}P_{0.9}$ LED on top of an $In_{0.53}Ga_{0.47}As$/InP NIR photodetector. Due to the lattice-matching requirements in semiconductor monolithic growth and due to limited choices of semiconductor materials for wafer fusion process, 1.5 μm NIR light was converted only down to 0.87 μm with reported devices. The organic-inorganic hybrid upconverter works on the same concept, except that the LED is replaced with an OLED [38-39]. Fig. 2.6 shows the actual device structure of

an organic-inorganic hybrid upconverter, as reported by Ban et al. In this hybrid device, the p-doped top layer of the p-i-n Photodetector functions as the anode of the OLED. As there is no intrinsic charge carrier in the organic molecules, all charge carriers have to be injected from the cathode (electrons) and the anode (holes). The injection of holes from p-InP layer of the p-i-n detector (anode for OLED) is modulated by incoming 1.5-μm light. The interfacial layer between the organic and inorganic layers is crucially important in such heterointegration of organic over inorganic devices.

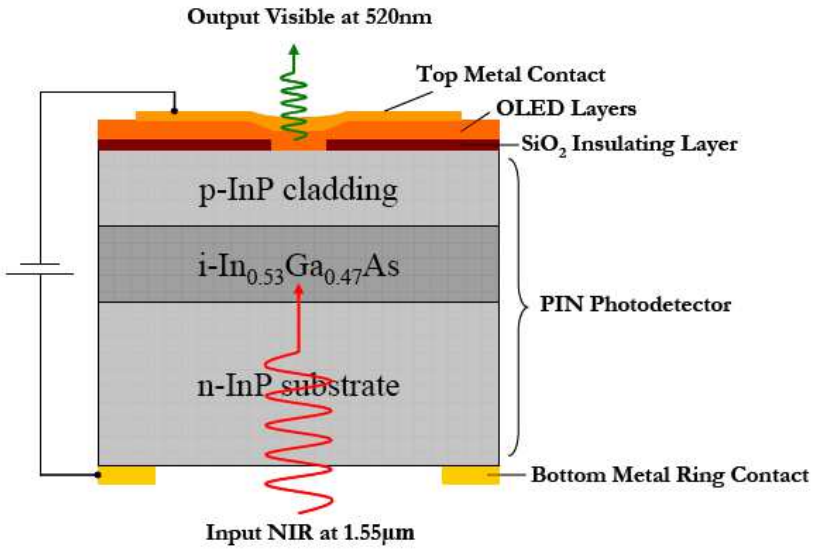

Figure 2.6 Organic-inorganic hybrid upconverter device structure[39]

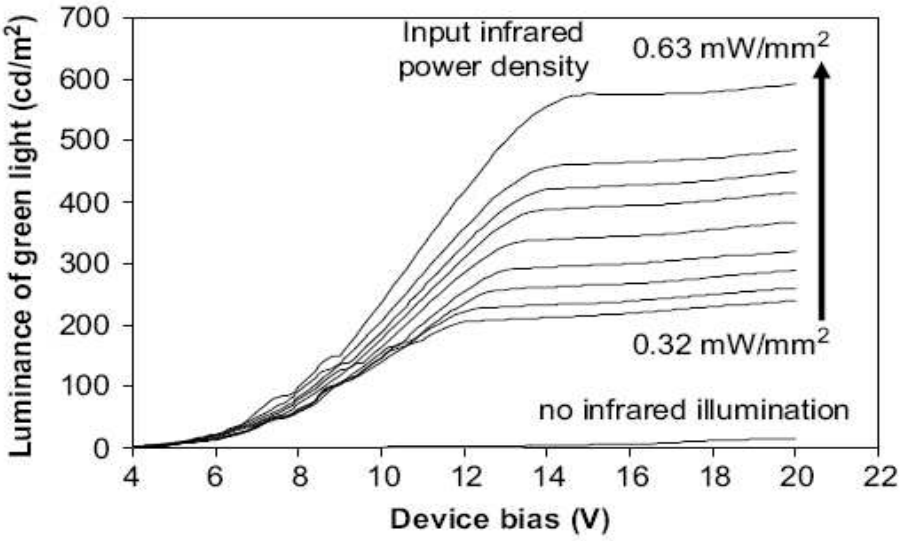

Figure 2.7 Experimental result of organic-inorganic hybrid upconverter [39]

Under a normal bias condition as shown schematically in Fig. 2.6, the OLED component is under forward bias and the p-i-n InGaAs/InP detector component is under reverse bias. Without NIR illumination, the OLED luminance induced by dark current upon the application of bias voltage was very small. The NIR light was absorbed by the InGaAs layer of the detector component, generating photocarriers. The photocarriers then crossed the organic/inorganic interface and were injected into the OLED layers, where visible light at 520 nm was emitted (Fig. 2.7). Efficient hole injection from semiconductor to organic layers was achieved, and the inorganic–organic interface had an excellent electrical connection due to the insertion of a thin C_{60} layer and a CuPc layer at the interface. Room-temperature optical upconversion from 1.5 μm to 520 nm was achieved with this prototype device. However, the performance of the device (in particular external efficiency ~0.7% W/W) needs to be further improved before it can be used for practical applications.

2.5.2 Device Fabrication and Characterization

Device fabrication starts with epitaxial growth of the inorganic photodetector wafer, which is typically an $In_{0.53}Ga_{0.47}As$/InP p-i-n structure. The InGaAs/InP structure is grown by metal organic chemical vapor deposition (MOCVD) on a n-type InP substrate, consisting of a 1.5-μm-thick intrinsic $In_{0.53}Ga_{0.47}As$ absorption layer sandwiched by n-type (below) and p-doped (above) InP layers. Major device fabrication steps are schematically illustrated in Fig. 2.8. The first step of the device fabrication is to pattern and etch square mesas onto the Photodetector substrate (step a). The p-InP layer is also the anode for OLED in the hybrid devices, the formation of the mesa structures in this layer creates electrical isolation among neighboring devices, which would significantly reduce dark current density of each individual device. A SiO_2 layer is then grown on the top surface of the InGaAs/InP sample using plasma-enhanced chemical vapor deposition (step b). This is for the purpose of preventing short circuits between the top electric contact and the underlying semiconductor substrate since the OLED layers would be only ~100 nm thick. Square windows are patterned using photolithography and chemically etched onto the SiO_2 layer (step c). The chemical etching goes through the entire SiO_2 insulation layer to expose the semiconductor square mesa areas, on top of which the OLED layers would be deposited in the second stage of device growth to form the upconversion devices. A ring metal contact (Cu/Cr) is deposited onto the backside of the n-substrate of the InGaAs/InP sample (step d), serving as the common bottom contact for the upconverter devices and allowing 1.5-μm light being shone from the back.

The InGaAs/InP sample is then cleaned with acetone, methanol, and deionized water and thereafter is ready for the second stage of the device growth. Immediately before being loaded into Kurt J.Lesker cluster tool for OLED layer deposition, the InGaAs/InP substrate is merged into $(NH_4)_2S$ water solution for 1 min at room temperature followed by deionized water rinse and N_2 gas blow dry. This surface passivation treatment was found to effectively reduce the dangling bond states on the semiconductor surface, enhancing the hybrid device performance. All molecular films are deposited sequentially through a shadow mask over the entire top surface of the InGaAs/InP sample (step e). Cathode metal electrodes are deposited right on the top of the mesa structures using a second shadow mask (step f). The top cathode layer is typically made of LiF/Al/Ag, which has an adequate sheet conductance and is partially transparent to green light as well.

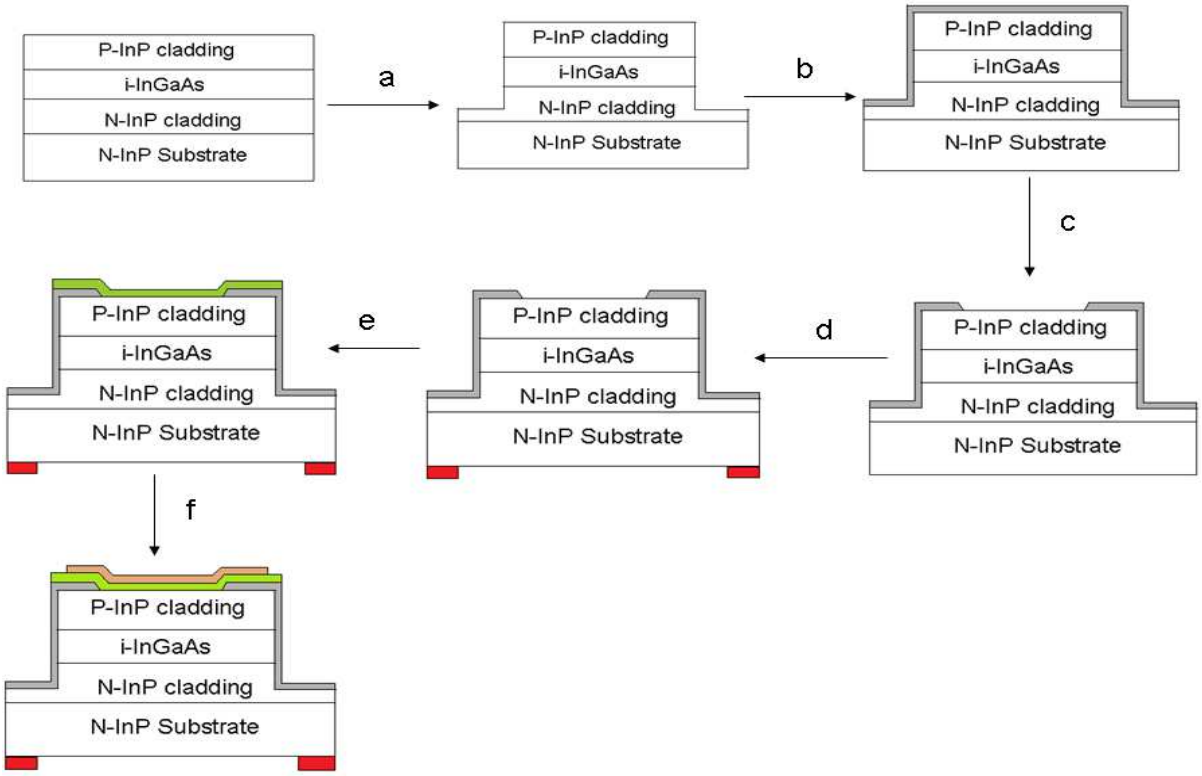

Figure 2.8 Schematic diagram of fabrication process of hybrid upconverter a) Mesa etching; b) SiO_2 deposition; c) SiO_2 window opening ; d) Bottom contact deposition; e) OLED layer deposition. F) Top metal contact deposition.

A Kurt J. Lesker OLED cluster tool is capable of plasma treatment, sputtering, and evaporation of organic and metallic layers (base pressure of 10^{-8} Torr). It can process 2 or 4 inch square substrates

with good layer uniformity, repeatability, and reliability. As shown in Fig. 2.1, five chambers are arranged around a central distribution chamber (CDC). The sample holder together with the stainless steel shadow masks to define the device structure, as seen in Fig. 2.2, is loaded into the entry/lock chamber to pump down. Subsequently the sample is transferred to the organic chamber via CDC. After deposition, the sample can be transferred to the entry/lock chamber to receive another mask, then to the metallization chamber, or to any other chamber until it has received all specified layers. At the completion of the process of device fabrication the sample can be loaded out from the entry/lock chamber. Generally, evaporation of thin films for OLEDs only involves in the organic chamber and metallization chamber.

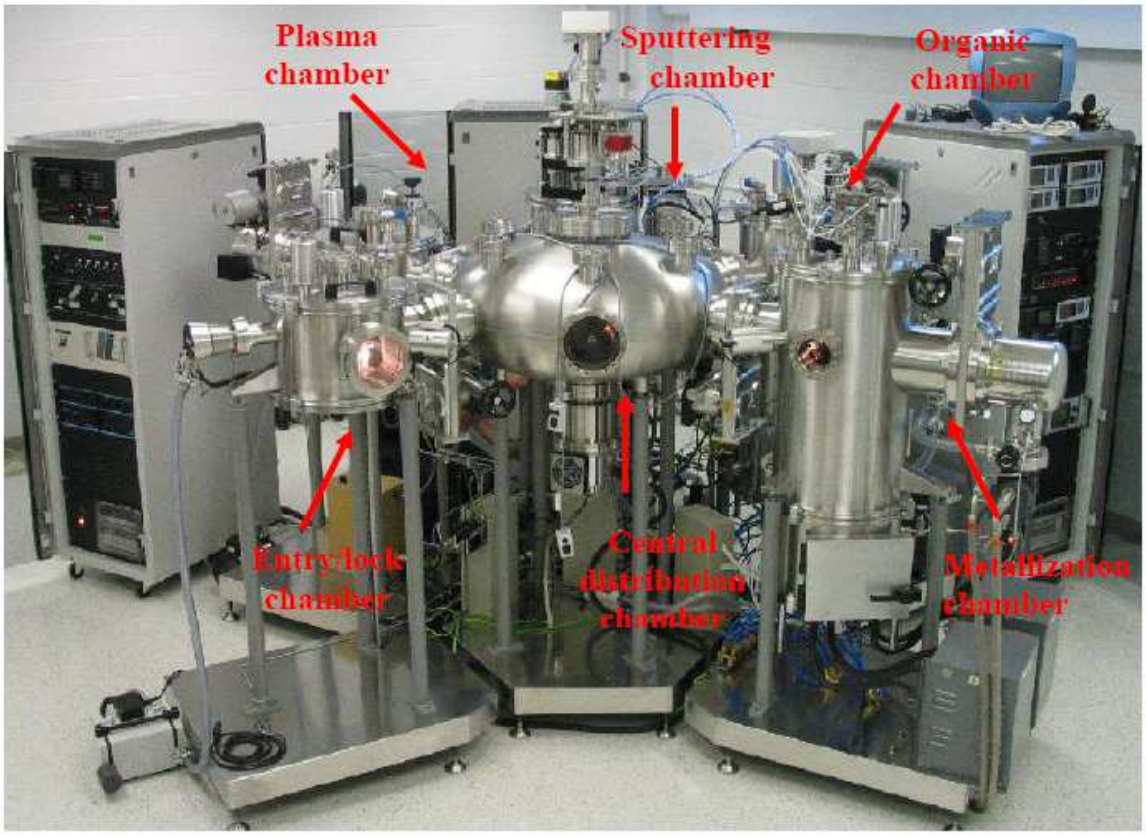

Figure 2.9 A Kurt J. Lesker OLED cluster tool with six chambers [40].

Figure 2.10 A sample holder (left) and a mask holder (right) [40].

Current–voltage (*I*-*V*) characteristics are measured using an HP4140B pA meter. Luminance-voltage (*L*-*V*) measurements are taken using a Minolta LS-110 luminance meter. The input 1.5-μm light is from an EXPO optical test system (IQ203). The EL spectra in the visible range were recorded by a USB2000 miniature fiber optic spectrometer. The USB2000 spectrometer couples a low-cost, high-performance 2048-element linear CCD-array detector The USB2000 works the same way as other spectrometers in that it accepts light energy transmitted through single-strand optical fiber and disperses it via a fixed grating across the linear CCD array detector, which is responsive from 350-1100 nm. All measurements are conducted at room temperature and in atmospheric condition [Fig 2.11]. The dwell time of each data point in the *I*-*V* and *L*-*V* measurements is 3 seconds.

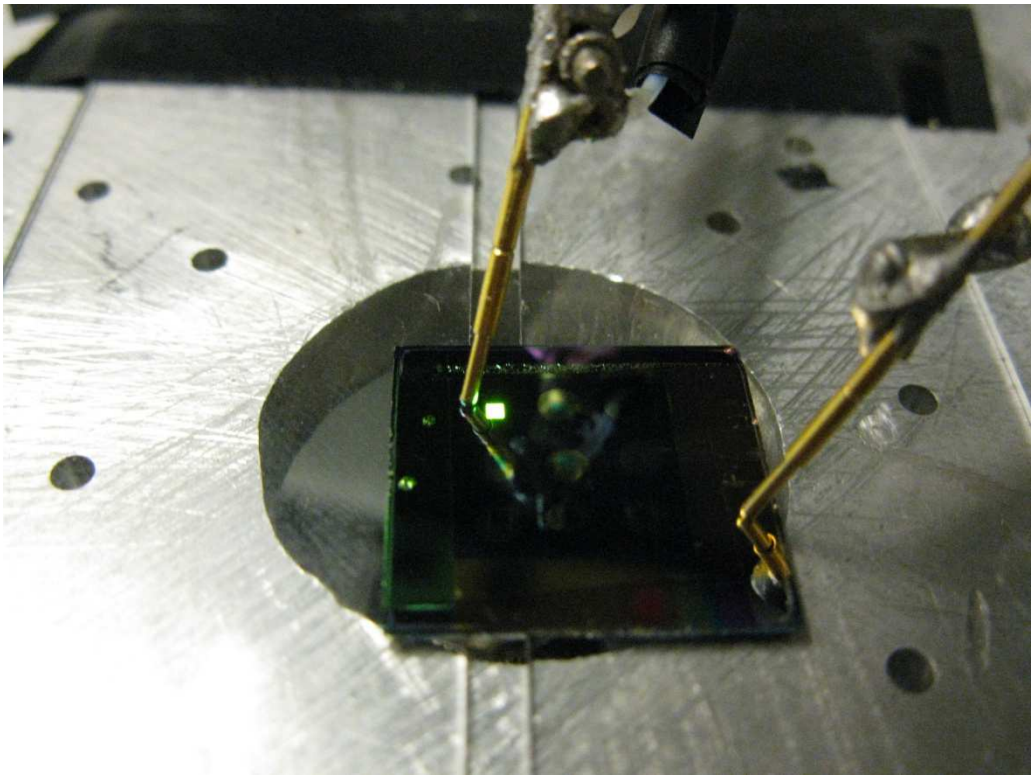

Figure 2.11 Current-voltage-luminance measurement stage

2.6 Challenges and Thesis Overview

The proposed research is aimed towards addressing some of the current challenges in making large-area, low-cost and high-perfomance hybrid upconversion device by focusing on the following aspects:

1. The investigation of the interfacial phenomena at the organic/inorganic interface to aid the design and improvement of the integration layer structures. The output photons emitted downward from OLED would penetrate into underlaying InP layer and make no contribution to the useful optical output. New structure must be introduced to collect the photons that are being wasted.

2. Performance improvement of single-mesa hybrid optical upconverters. By introducing a gain mechanism into the photodetector section of the upconverter, the overall upconversion efficiency can be increased significantly. A promising option to implement gain is a heterojunction photo transistor (HPT). The electrical gain of this HPT design could be as high as 100 to 500. With the incorporation of the electrical gain, the hybrid device will function not only as a wavelength converter, but also as an optical amplifier

3. Demonstration of large-area hybrid imaging devices. High performance 1.5 μm imaging devices is of great interest to imaging industry and important for many military and civilian applications. Finally, real-time imaging operation is expected by the integration of upconversion imaging devices and Si CCD.

This thesis can be outlined as follows.

Chapter 1 and Chapter 2 comprehensively review the infrared imaging and the progress in newly emerged optical upconversion research field.

Chapter 3 first describes two novel hybrid optical upconverter structures, which substantially improve the upconversion efficiency by embedding a metal mirror and/or replacing the photodetector with a heterojunction phototransistor.

Chapter 4 presents the simulation and fabrication of hybrid optical amplifier based on the optimized heterojunction phototransistor with OLED

Chapter 5 first presents the obstacles for pixelless operation. Solutions are proposed in order to achieve pixelless operation with novel device design and fabrication. A hybrid optical upconverter based on Schottky junction will be presented.

Chapter 6 gives a conclusion of this thesis.

Chapter 3
Novel Hybrid Optical Upconverter Structure

In chapter 2, hybrid optical upconverter was introduced, which was made by direct tandem integration of an inorganic InGaAs/InP photodetector with an OLED. Incoming 1.5 μm light was absorbed by the InGaAs/InP photodetector to generate photocurrent. The photo-induced charge carriers were then injected into the emission layer of the OLED to emit visible light (green). This is a linear relationship between the intensity of output green light and the intensity of input infrared light. This hybrid upconverter can be a standalone device to convert invisible infrared scenes into the visible range, which is observable to naked human eyes. However, the performance of the device needs to be further improved before it can be used for practical applications. The reported external efficiency was only 0.7% at a device bias of 20 V. Based on the understanding gained from the chapter 2, the device performance was limited by the photocarrier generation, carrier injection efficiency and the OLED efficiency. In this chapter, novel organic/inorganic hybrid devices for infrared to visible light upconversion will be designed, fabricated and characterized. In the first design, by inserting a metal layer between the InGaAs/InP Photodetector and the OLED, the carrier injection efficiency and OLED efficiency could be improved. In the second design, the InGaAs/InP Photodetector will be replaced by an InGaAs/InP HPT, which could introduce electrical gain to enhance the photocarrier generation. The outcomes of this task will make further advances into performance optimization and fabrication simplification of the hybrid optoelectronic devices. Two structures will be discussed in detail – an upconverter with an embedded mirror and an upconverter with an integrated p-n-p HPT.

3.1 Hybrid Optical Upconverter with an Embedded Mirror

3.1.1 Motivation

Flexibility in material integration, in particular, an electrically floating electrode with a primary function as an optical mirror and also electron injection layer has been proposed and demonstrated. Based on the same idea, a highly reflective metal mirror is proposed to be placed between the photodetector and the OLED. The immediate benefit of the insertion of a metal layer between the OLED component and the photodetector component comes from its high optical reflectivity in the near-infrared and visible light range. As shown in Fig. 1.10, the spontaneous emission in OLED layer

has random radiative directions. Photons that are emitted upward may escape from the top surface and contribute to useful light output. In the absence of a metal layer, photons that are emitted downward may get lost and would not contribute to the top output. With a high-reflectivity metal layer underneath the OLED, the photons that are originally emitted downward will be bounced back at the OLED/metal interface (see Fig. 3.1). After changing directions, this portion of photons can also contribute to the top emission of the device thus enhancing OLED efficiency. The reflectivity of Ti/Au contact is higher than 95% for the light of wavelength ~520 nm [41]. The absorption efficiency on the photodetector side can be enhanced as well with the insertion of such a metal layer. The input infrared light, if not being completely absorbed by the absorption layer, would be reflected back at the metal/photodetector interface and passes through the absorption layer again. With these two-fold enhancements (on light emission and light absorption), it is expected that the overall optical upconversion efficiency would be substantially improved through the integration of such an embedded mirror (the metal layer). On the other hand, metal layer also can improve the carrier injection from the inorganic to organic layers. In these hybrid electronic and optoelectronic devices, the carrier transport and energy transfer between the organic and inorganic materials play a vital role in enabling the integration of functioning units. Our preliminary results reveal how strongly the device performance was affected by different organic-inorganic interfaces. The embedded metal is supposed to reduce the surface state density of inorganic semiconductor and the energetic barriers between organic/inorganic materials to permit continuous flow of charge carriers across the interface, and for enhancing device performance.

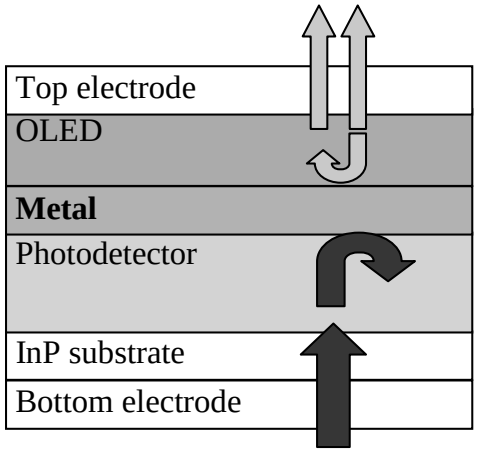

Figure 3.1 The insertion of a highly reflective metal layer as an embedded optical mirror can improve the absorption and emission efficiency.

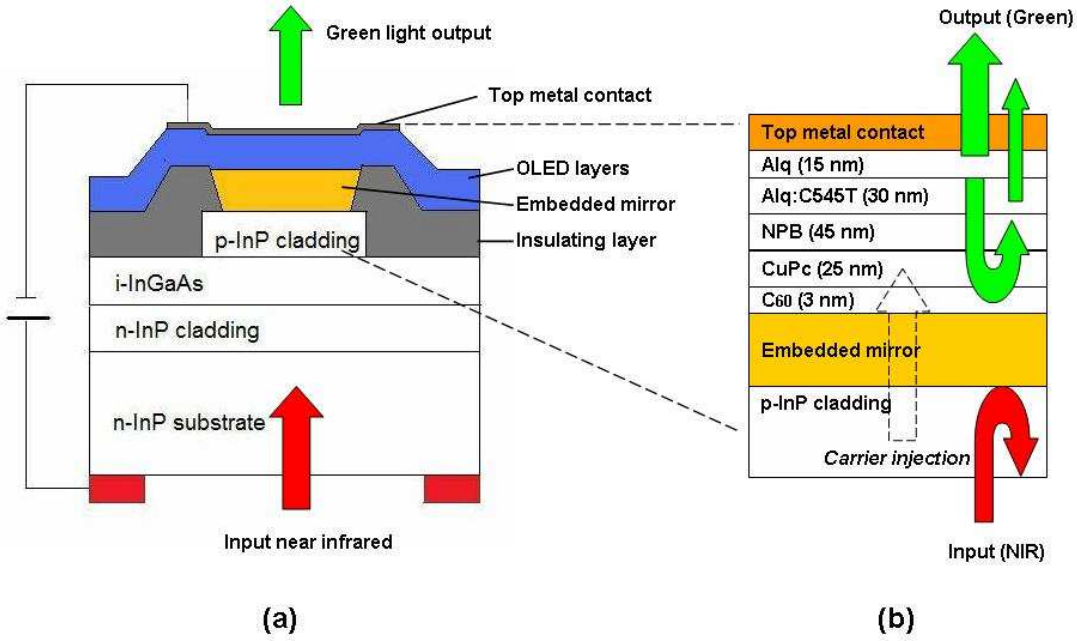

Figure 3.2 (a) Schematic cross section of an inorganic-organic upconverter device. (b) Schematic configuration of the OLED layers of the integrated devices and the embedded mirror. The layer thickness is not to the scale. C_{60} is Carbon fullerene. CuPc stands for Copper phthalocyanine. NPB is N, N'-di(naphthalene-1-y1)-N,N'-diphenyl-benzidine, Alq:C545T is light emission layer. The embedded mirror layer consists of 20 nm Ti and 200 nm Au. The top metal contact consists of LiF (1 nm)/Al (5 nm)/Ag (20 nm).

3.1.2 Device Fabrication and Analysis

As there is no intrinsic charge carrier in the organic molecules, all charge carriers have to be injected from the cathode and the anode into the emission layer of the OLED component. The holes from the p-InP layer of the p-i-n detector need to cross the embedded Au mirror layer before injection into OLED. The embedded mirror layer thus plays a vital role in such heterointegration of organic on inorganic devices. As will be shown, the embedded metal mirror is found to be crucial in forming a good contact, facilitating efficient hole injection across the organic–inorganic interface. Device fabrication process can mostly be referred to Fig. 2.8. The only alteration is the deposition of a metal layer (20 nm Ti / 200 nm Au) – between the step c and d – onto the top of the opening windows of the mesas. Two types of hybrid devices are fabricated to examine the effect of the embedded mirror. Device A is prepared with an embedded metal mirror (20 nm Ti/ 200nm Au) before loading it into the cluster tools for OLED layer deposition. Device B is prepared without such a metal mirror. Other than this embedded mirror, all procedures are identical in processing and fabrication.

Under bias condition as shown schematically in Fig. 3.2(a), the OLED component is under forward bias and the p-i-n InGaAs/InP detector component is under reverse bias. Without NIR illumination, the OLED luminance, induced by dark current upon the application of bias voltage was very small. Fig. 3.3 (a) shows the *I-V-L* curves of device A under 1.5 μm infrared illumination. The input NIR power density was around 0.67 mW/mm^2. The input infrared light was absorbed by the InGaAs layer of the detector component, generating photocarriers. The current density (photocurrent density plus dark current density) started to rise at a low bias (~3.2 V). This shows that efficient hole injection from the semiconductor to the organic layers was achieved. As the device bias continued to increase, the current density increased rapidly up to 270 mA/cm^2. The rapid increase of the current density is mainly due to the increase of the photocarrier collection efficiency, which was enhanced by the additional external voltage that dropped across the p-i-n detector. At biases above 11.5 V, the current density exhibited a plateau with a slow increase due to the dark current. This indicates that beyond this point almost all of the photocarriers that were generated by the absorption of the input NIR illumination were collected and contributed to the electrical current. Correspondingly, the output luminance of the green emission from the OLED exhibited a rapid increase with the device bias until saturation at around 1580 cd/m^2 at 11.5 V with an input infrared power density of 0.67 mW/mm^2. This NIR-induced luminance is around two orders of magnitude higher than that of a control device (Device B, without an embedded mirror, luminance of ~11cd/m^2 at 11.5 V, see Fig. 3.5).

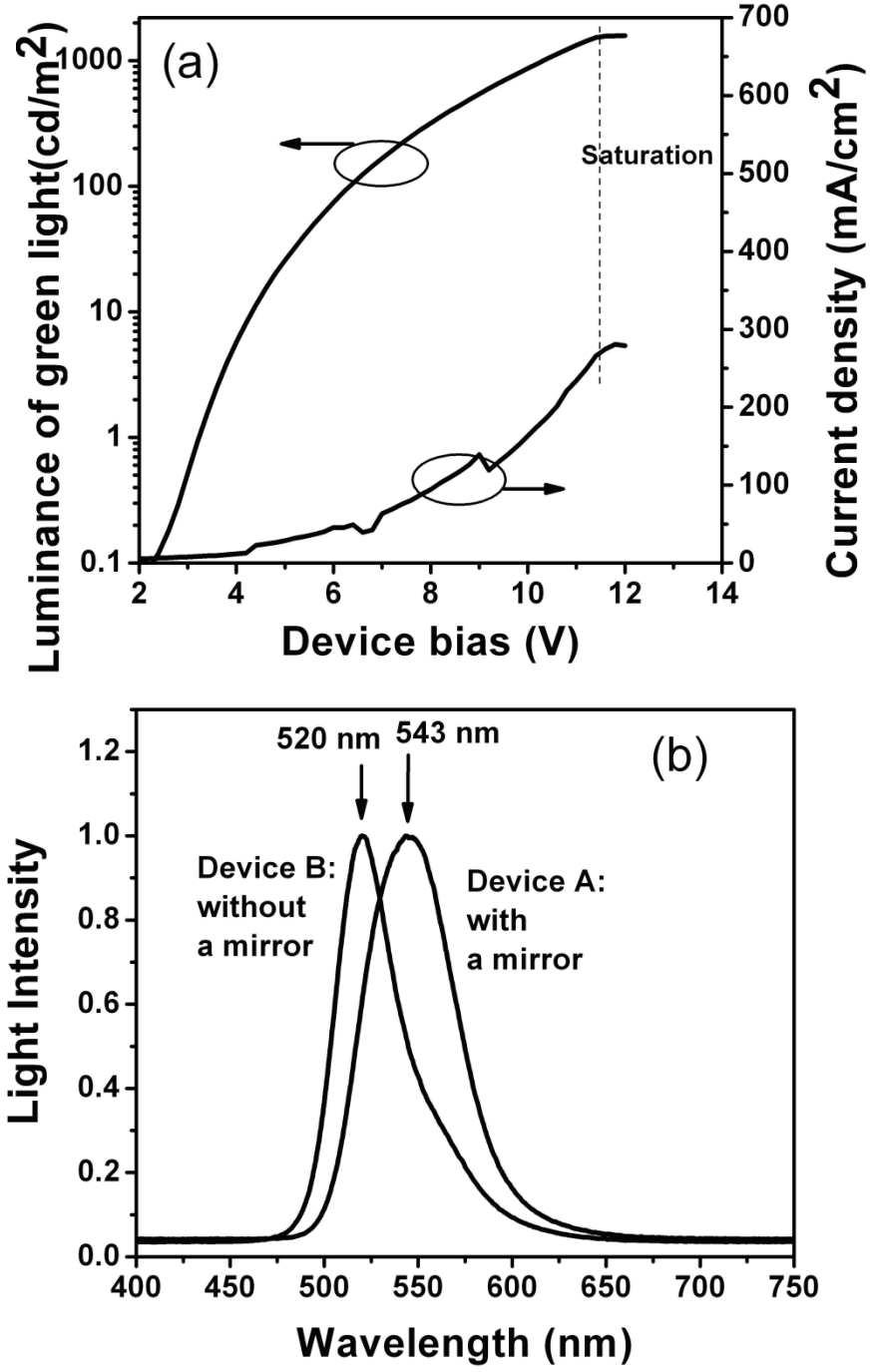

Figure 3.3 (a) I-V-L curves of device A under 1.5-μm infrared illumination, with NIR power density of 0.67 mW/mm^2; (b) Emission spectrum from the OLED of the integrated upconverter device A and device B.

The luminance efficiency (cd/A) can be converted to OLED external efficiency (W/A) by assuming that the upconverter device is a Lambertian source and using 488 lm/W as the power conversion constant [38]. The 488 lm/W is the effective power conversion constant that is normalized by the OLED emission spectrum). The optical power efficiency (W/A) is calculated by luminance efficiency (lm/A) × π/488 (lm/W). The overall external upconversion efficiency can then be calculated by multiplying the detector responsivity (A/W) and the OLED optical power efficiency (W/A). This approach ensures that the calculation of the upconversion efficiency excludes any contribution from the dark current. By the same method, the overall external upconversion efficiency of device A is calculated to be ~1.5% W/W at a bias of 11.5 V. This is an improvement of more than 100% when compared to the first reported device in chapter 2.5. The improved device performance can be attributed to the insertion of the embedded mirror, which enhances the light emission and light absorption by bouncing back the photons, as discussed earlier in section 3.1.1. In addition, the highly-reflective embedded Au mirror, in combination with the top metal contact (partially transparent), forms a microcavity. This confines the OLED spontaneous emission, and could alter the emission spectrum. Fig. 3.3 (b) shows the emission spectra from the OLED of devices A and B. The output emission spectrum of device A (with a microcavity) is peaked at 543 nm, while that of device B (without a microcavity) is peaked at 520 nm. The ~23-nm redshift in peak wavelength can be attributed to microcavity effects [42-43].

To demonstrate the NIR's visible light upconversion operation, the intensity of the output OLED emission was measured with different input NIR power densities. The results of device A are plotted in Fig. 3.4(a). In the dark, (i.e., no input NIR illumination), the luminance of the green light emission from OLED is very low; i.e., only up to 10 cd/m^2 at a bias of 12 V, due to the dark current. With NIR illumination, the output luminance of the device became evident at a bias of less than 4 V, and saturated at biases of 10-12 V (depending on the input NIR power density). As the NIR input power density increased from 0.34 to 0.67 mW/mm^2, the saturation values of the output luminance increased from ~600 to ~1580 cd/m^2, clearly demonstrating the upconversion operation of the hybrid device at room temperature. Fig. 3.4(b) shows the NIR induced green light emission of device A at a bias of 12 V under different NIR input power densities. A fairly linear relation between the input and output powers is observed. It is worth noting that the NIR-induced green light luminance – device bias curves almost overlap with one another at low biases (0-10 V) for different input power densities, as shown in Fig. 3.4(a). This indicates that under low device biases (<10 V) the device performance was mainly reduced by inadequate photo-carrier collection and charge carrier injection efficiency.

It is important to maximize the NIR-induced luminance output while simultaneously minimizing the dark-current-induced luminance. Fig. 3.4(c) shows the ratio of the NIR-induced luminance with an input power density of 0.67 mW/mm^2 versus the dark-current-induced luminance (device A) as a function of the device bias (light-to-dark ratio). One can see that the ratio first exhibits a rapid increase with increasing the device bias, and reaches a peak value of over 550 at ~5.5 V. As the device bias continues to increase, it gradually decreases to ~100 at 12 V. The variation of this light-to-dark ratio can be attributed to the competition between the photocurrent and the dark current of the device, as both strongly depend on the bias voltage.

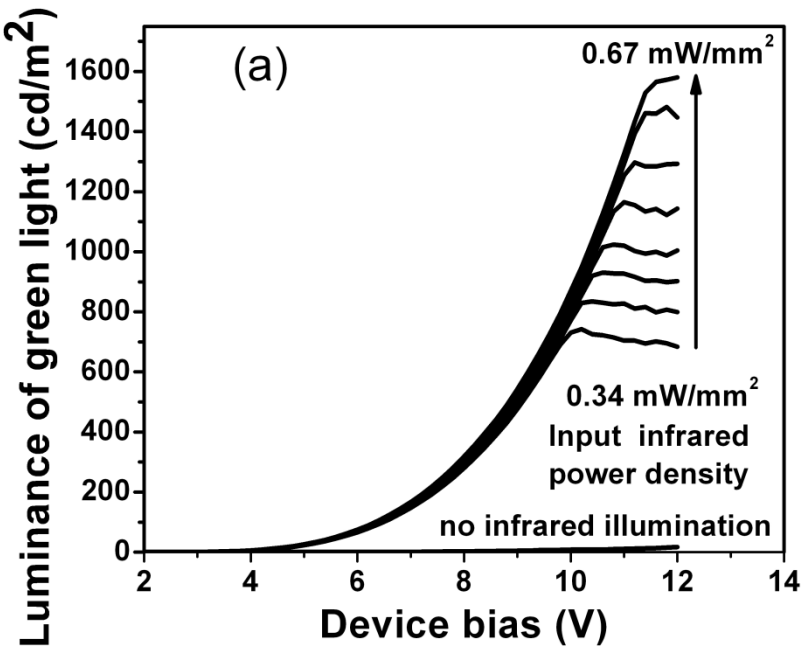

Figure 3.4 (a) NIR-induced green light luminance as a function of device bias different illumination conditions (device A).

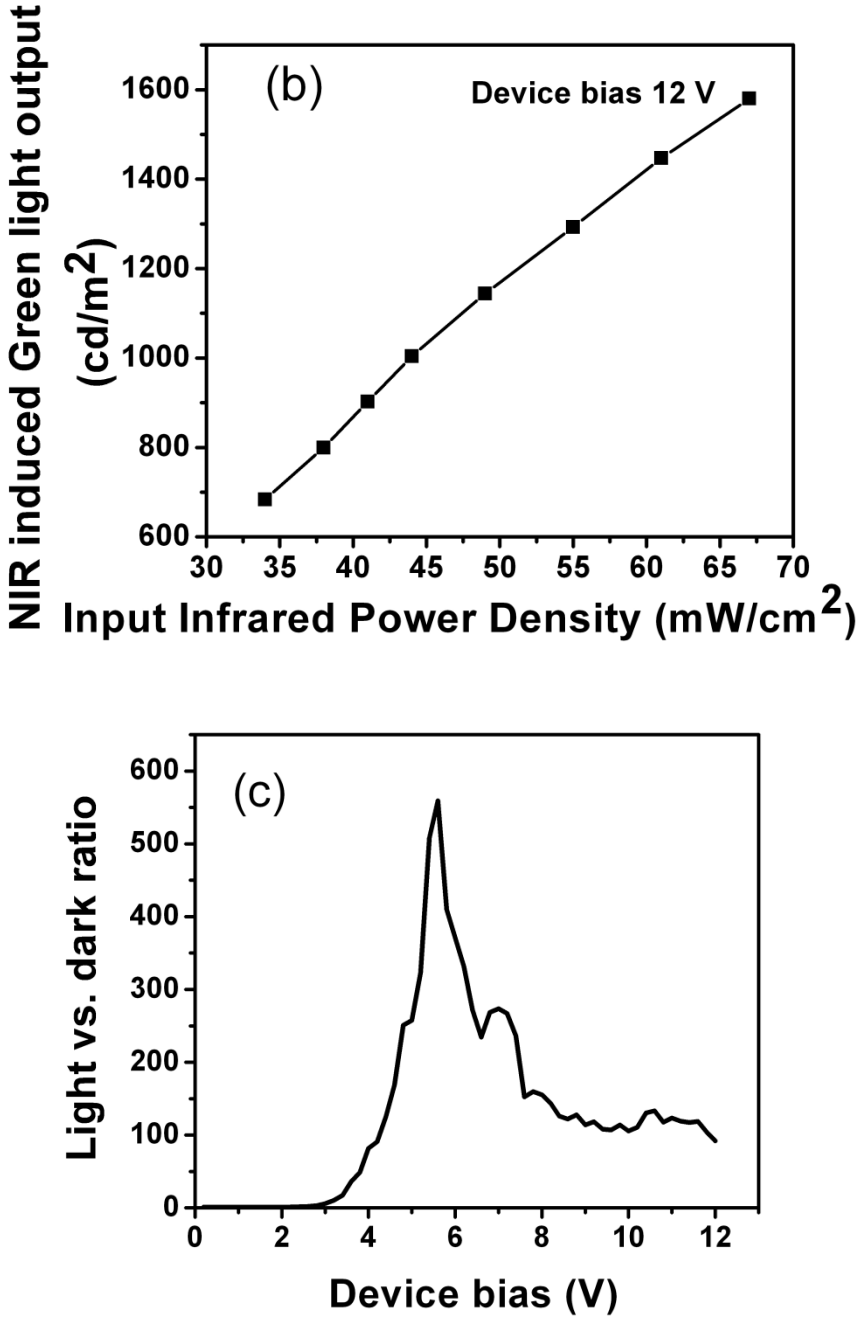

Figure 3.4 (b) NIR-induced green light luminance as a function of input NIR power densities at a device bias of 12 V; (c) Calculated ratio of the NIR-illumination-induced luminance (at 0.67 mW/mm^2) versus dark-current-induced luminance as a function of device bias (device A).

At low biases, the collection efficiency of the photocurrent is low, leading to low NIR-induced luminance. The collection efficiency of the photocurrent starts to increase at ~3.0 V. In consequence, the NIR-induced luminance, as well as the light-to-dark ratio, increases dramatically. The dark current also increases with the device bias, but at a much slower rate than that of the photocurrent at this initial biasing stage. At a bias above ~5.5 V, the increase of the dark current surpasses that of the photocurrent, leading to the decrease of the light-to-dark ratio. When the bias is over ~11.5 V, the photocurrent becomes saturated (the top curve in Fig. 3.4 (a)) but the dark current continues to grow. This leads to an accelerated decline of the light-to-dark ratio (Fig. 3.4 (c)). It is therefore concluded that the optimum device bias for the up conversion operation of device A is ~11-11.5 V, at which the NIR-induced luminance reaches its saturation value, and the light-to-dark ratio is sufficiently high (~130).

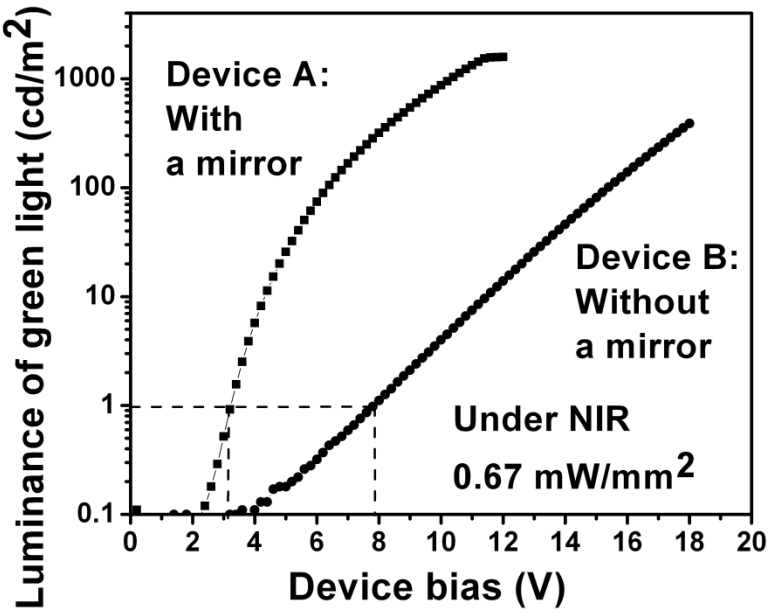

Figure 3.5 Luminance vs. voltage curves of up conversion with or without an embedded mirror, both devices were with NIR illumination power density of 0.67 mW/mm^2.

Device A (with an embedded mirror) and device B (without an embedded mirror) were tested under the same experimental conditions. The two devices showed distinct differences in their turn-on voltages; i.e., device A at ~3.2 V, device B at ~7.8 V for an output luminance of 1cd/m^2 (Fig. 2.4). As the devices biases continues to increase, the NIR-induced luminance of the two devices increases rapidly, with device A exhibiting a faster slope than device B. This is indicative of an enhanced

efficiency for device A. Clearly, the performance of device B is reduced by inadequate carrier injection efficiency. The insertion of a metal mirror is crucial in reducing the turn-on voltage and improving the charge carrier injection efficiency, which causes orders of magnitude improvement in specific voltage bias. The reduction in the turn-on voltage from ~7.8 V (device B) to ~3.2 V (device A) could be explained as follows. For convenience, the charge injection and transport can be divided into three steps: step 1, hole transfer from p-type InP to Ti/Au; step 2, hole transport from Au to C_{60}; step 3, hole transport in C_{60} and transfer from C_{60} to CuPc. For step 1, Ti/Au has been commonly used as a p-InP ohmic contact metallization, and the contact resistance is very low [44-45]. For step 2, the efficient hole injection across Au/C_{60} bilayer has been demonstrated in many experimental studies. The *d*-band energy matches well with HOMO band of the C_{60}. Under an external electric field, the C_{60} HOMO electrons may tunnel to these empty *d* states thus lead to generation of holes in the C_{60} [42]. For step 3, the hole will transport in C_{60} and transfer from C_{60} to CuPc at the interface. This process is also known experimentally to be highly efficient in many devices, such as C_{60}/CuPc solar cells.

Efficient carriers injection from the inorganic Photodetector to the OLED was achieved by the insertion of a thin Au metal embedded mirror at the inorganic-organic interface. The NIR-induced green-light luminance reached as high as 1580 cd/m^2 at a bias of 11.5 V with an input 1.5-μm NIR power density of 0.67 mW/mm^2. The optimization of the embedded metal mirror structure of the hybrid devices lowered the turn-on voltage to 3.2 V for an output luminance of 1.0 cd/m^2. This special structure could significantly improve the performance of single devices by recycling the lost emitting light and improving the integration of organic and inorganic layers, so it is excellent for the imaging device based on pixelated array, but is not applicable for pixelless imaging devices.

3.2 Hybrid Optical Upconverter based on HPT/OLED

3.2.1 Motivation

In section 3.1, a hybrid NIR optical upconverter with an embedded metal mirror was successfully fabricated. With the insertion of metal mirror, the device performance has an improvement of more than 100% in terms of efficiency. However, the overall external upconversion efficiency is still low, only around 1.5% W/W. A higher overall upconversion efficiency is surely desired in order for the upconversion scheme to be more attractive.

In this section, a new structure with a built-in gain mechanism will be proposed and fabricated, a hybrid optical upconverter that integrates a p-n-p InGaAs/InP HPT and an OLED. A HPT is basically

a heterojunction bipolar transistor with a light sensitive collector and base region. A p-n-p InGaAs/InP HPT consists of a p-typed InP layer as emitter, a thin n-type $In_{0.53}Ga_{0.47}As$ layer as base and a p-type $In_{0.53}Ga_{0.47}As$ layer as collector (Fig. 3.6(a)) [46]. P-InP is window layer and its bandgap energy is higher than the photo energy of 1.5 μm light. So the input light 1.5 μm passes through the n-InP emitter and then is absorbed in the narrow bandgap collector and base region, producing electron-hole pairs (Fig. 3.6(b)). Subsequently, electrons accumulate in the base and these extra charges forward bias the base-emitter junction, causing more holes to be injected from the p-InP emitter, leading to an electrical gain (see Fig. 3.6(a)). The amplification process is the same as that in a transistor, except that the base-emitter forward bias is provided by the optical absorption process rather than a metal contact [47]. The holes generated in the HPT component will be injected into the OLED component to emit green light. With the incorporation of a sufficient high electrical gain, the optical output power could exceed the input signal and thus the optical upconverter device would potentially function as an optical amplifier.

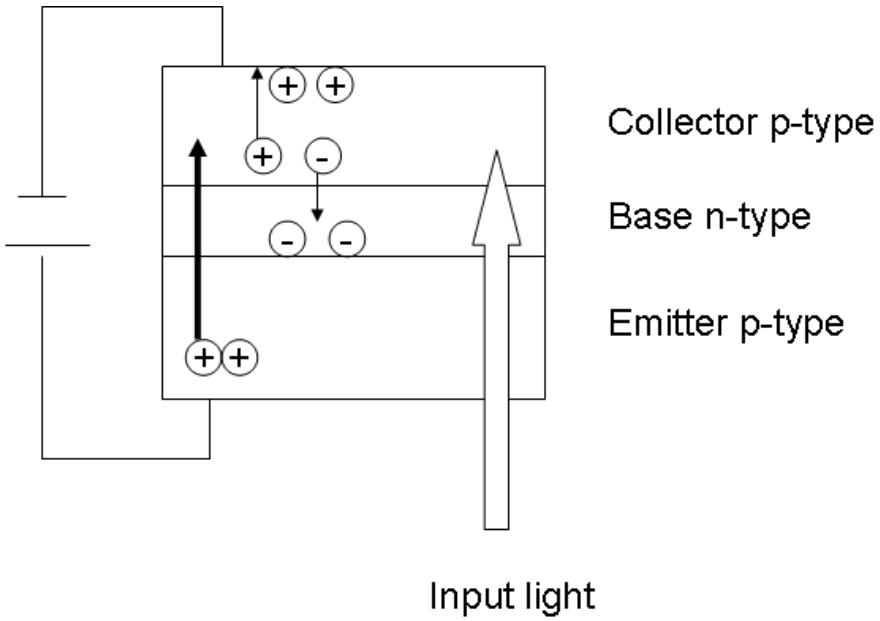

(a)

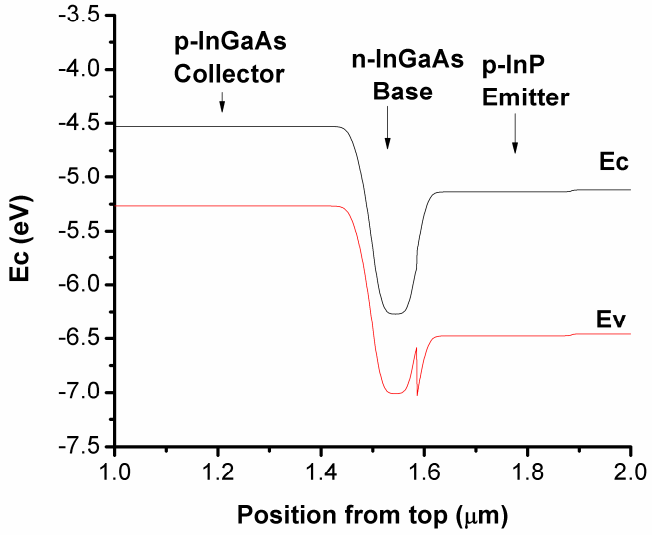

(b)

Figure 3.6 (a) Schematic diagram of p-n-p HPT structure; (b) Band diagram of InGaAs/InP p-n-p HPT (Forward-bias emitter-base junction and reverse-bias collector-base junction)

3.2.2 Device Fabrication

The HPT structure was grown by chemical beam epitaxy (CBE) on a p-type InP substrate. As shown in Fig. 3.7(a), the wafer growth started with an 500 nm InP emitter contact (p^+, 1×10^{18} cm^{-3}) and a 300-nm InP emitter layer (p, 5×10^{17} cm^{-3}). The growth continued with a 10-nm undoped InGaAs spacer and a 75 nm InGaAs base layer (n, 1×10^{18} cm^{-3}). Then came a 1 μm InGaAs collector layer (p, 5×10^{17} cm^{-3}). The structure was capped with a 500-nm InGaAs contact layer (p^+, 1×10^{18} cm^{-3}).

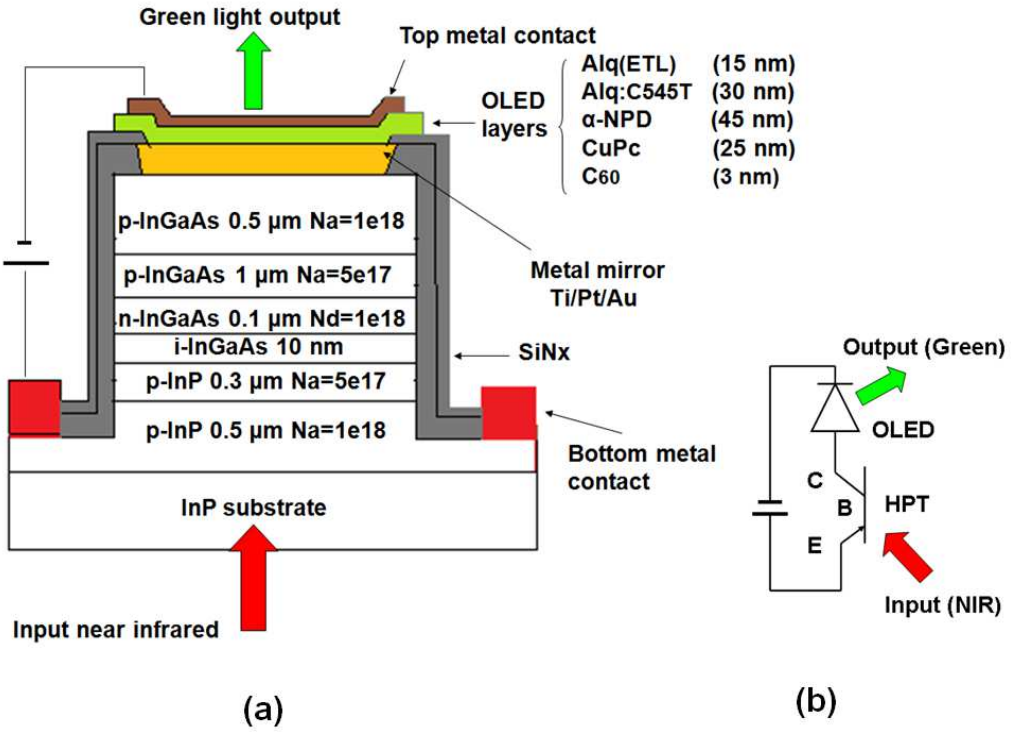

Figure 3.7 (a) Schematic cross section of hybrid optical upconverter device integrated by InGaAs/InP HPT and OLED (Note that the thickness of the organic and inorganic layer is not to the scale). (b) Schematic of the operation of the hybrid upconversion device.

The first step of the device fabrication was to pattern and etch square mesas (1×1 mm^2) onto the p-InP emitter. Square mesas were patterned using standard photolithography. A solution of H_2SO_4: H_2O_2: H_2O (1:8:160) was used to etch the InGaAs layer (~1.6 μm thick) and another solution of H_3PO_4: HCl (10:1) was used to etch part of the p-InP layers (~0.5 μm thick) to complete the square mesas. A 200 nm SiN layer was then grown on the top surface of the InGaAs/InP sample using plasma-enhanced chemical vapor deposition. The SiN outside of the square mesa was etched off to form an open area, where a metal layer (Ti/Pt/Au) was deposited to serve as a common bottom

contact. Square windows with a size of 0.9 × 0.9 mm^2 were patterned using photolithography on top of the square mesas and chemically etched onto the SiN layer. The etching went through the entire SiN insulation layer to expose the semiconductor square mesa areas, on top of which an embedded metal mirror (Ti 25 nm/ Pt 55 nm/Au 120 nm) was deposited using electron-beam evaporation. A second SiN layer was deposited to bury the metal mirror and was later partially etched off to expose a smaller window (0.8 × 0.8 mm^2) right on the top of the metal mirror. The second SiN layer was mainly for minimizing potential leakage current, which could significantly degrade device performance. The InP substrate was polished down to ~100μm thick and then glued to a piece of NIR transparent glass to allow NIR light access from the back side of the sample (Fig. 3.7(a)).

The InGaAs/InP substrate was then ultrasonically cleaned with a standard regiment of chloroform, acetone and methanol followed by ultraviolet (UV) ozone treatment for 30 minutes. Thereafter the sample was loaded into a Kurt J. Lesker cluster tool for deposition of the OLED. The layer structure of the OLED is shown in Fig. 3.7(a). All molecular films were deposited sequentially through a shadow mask (35 × 35 mm^2 opening) over the entire top surface of the substrate. The HIL of the OLED was a 3 nm thick layer of C_{60}. The HTLs consisted of copper phthalocyanine (CuPc) (25 nm) and N,N'-diphenyl-N,N'-bis-(1-naphthyl)-1-1'-biphenyl-4,4'-diamine (α-NPD) (45 nm). The 30 nm thick emission zone was tris-(8-hydroxyquinoline) aluminum (Alq_3), doped with 1 wt.% 10-(2-benzothiazoly)-1,1,7,7-tetramethyl-2,3,6,7-tetrahydro-1H, 5H, 11H-[1]benzo-pyrano [6,7,8-ij]quinolizin-11-one (C545T). The ETL was made of an addition 15 nm thick Alq_3 layer. Semi-transparent cathode metal electrodes (1.2 mm in diameter) were deposited on the top of the square mesa structures using a second shadow mask. The top cathode layer was made of LiF (1.0 nm)/Al (5.0 nm)/Ag (15 nm), which has an adequate sheet conductance, and is partially transparent to green light (520-540 nm). Finally a 45 nm thick Alq_3 layer was deposited, which could provide a better index of refractive-index matching from the LiF/Al/Ag to air. The device characterization setup was the same as that in section 2.5.2. All measurements were conducted at room temperature, and under normal atmospheric condition.

3.2.3 Device Analysis

Under bias condition as shown schematically in Fig. 3.7(b), the OLED component is under forward bias and the p-n-p InGaAs/InP HPT is under normal operating conditions (forward-biased emitter junction and reverse-biased collector junction). Fig. 3.8 shows the *I-V-L* curves of device under 1.5 μm infrared illumination. The input NIR power density was around 1 mW/mm^2. The input infrared light was absorbed by the InGaAs layer of the HPT component, generating photocarriers. The photocarriers were then amplified in the HPT component. The current density (photocurrent density plus dark current density) started to rise at a low bias (~4 V). This shows that efficient hole injection from the semiconductor to the organic layers was achieved via the floating metal contact (also the embedded mirror). As the device bias continued to increase, the current density increased rapidly up to 800 mA/cm^2 at 12V. The rapid increase of the current density is mainly due to the increase of the photocarrier collection efficiency and the internal electrical gain, which was enhanced by the additional external voltage that dropped across the HPT component. Correspondingly, the output luminance of the green emission from the OLED exhibited a rapid increase with the device bias, up to 25000 cd/m^2 at 12 V with an input infrared power density of 1 mW/mm^2. This NIR-induced luminance is around 15 times higher than that of the device in section 3.1. The inset of Fig. 3.8 shows the emission spectra from the OLED of device. The output emission spectrum of device is peaked at 545 nm, which has ~25-nm redshift in peak wavelength comparing with normal OLED emission. This red-shift again, is attributed to the aforementioned microcavity effects formed by the partially-reflective top metal contact and the metal mirror.

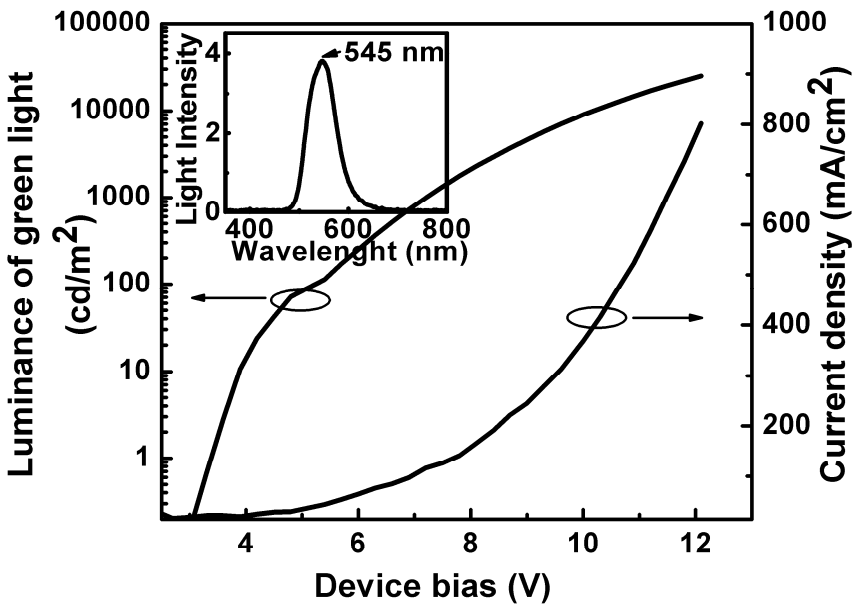

Figure 3.8 I-V-L curves of the upconversion device under 1.5-μm infrared illumination, with NIR power density of 1 mW/mm^2. The inset shows the emission spectrum from the OLED of the integrated upconverter device (peaked at 545 nm).

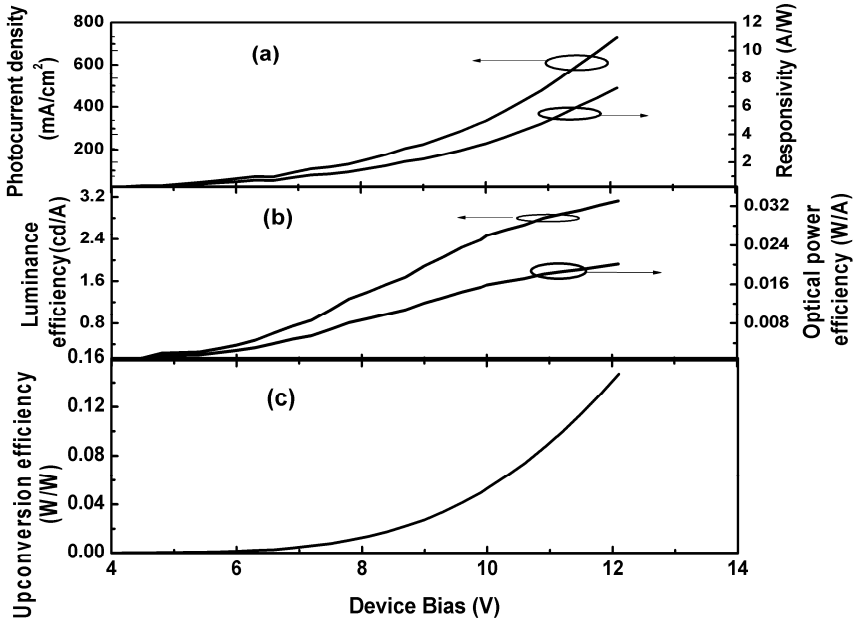

Figure 3.9 (a) Measured photocurrent density (mA/cm^2) as a function of device bias under 1.5 μm infrared radiation of 1 mW/mm^2 and the calculated responsivity (A/W) of the HPT component. (b) Measured luminance efficiency (cd/A) of the OLED component of the integrated upconverter and the calculated optical power efficiency (W/A). (c) Overall external upconversion efficiency (W/W) as a function of device bias calculated by multiplying the responsivity of the HPT part (a) and the OLED power efficiency (b).

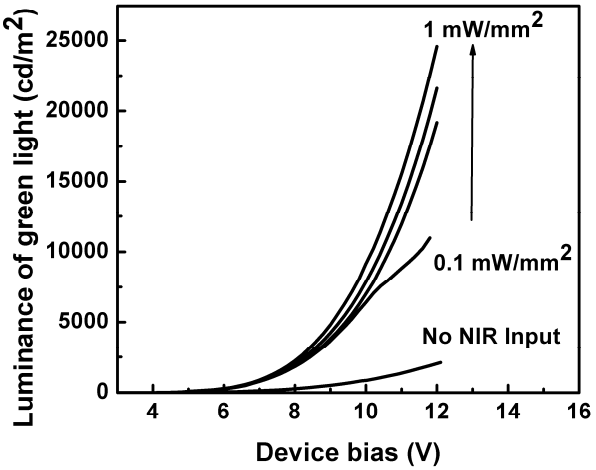

Figure 3.10 NIR-induced green light luminance as a function of device bias under different NIR illumination conditions (0.1 mW/mm^2, 0.4 mW/mm^2, 0.7 mW/mm^2, 1 mW/mm^2).

To obtain the responsivity of HPT component and overall external upconversion efficiency, the photocurrent density(total current density minus dark current density) and OLED current-luminance efficiency were measured in the same way as described in section 3.1. Fig. 3.9(a) shows the measured photocurrent density as a function of device bias under 1.5 μm infrared radiation (1 mW/mm^2), together with the calculated responsivity of the HPT component. The responsivity started to rise at 5V and gradually increased with further increase of the device bias. At 12 V bias, the responsivity was 7.5 A/W under input infrared radiation of 1 mW/mm^2. In comparison, the responsivity of an InGaAs/InP *p-i-n* photodetector with similar absorbing layer thickness is only 0.5 A/W [47]. The electrical gain of the HPT component of the hybrid upconverter was therefore estimated to be 15. Fig. 3.9(b) shows the measured current efficiency of the OLED part of the hybrid upconverter. The luminance efficiency (cd/A) can be converted to OLED external power conversion efficiency (W/A) by assuming that the upconverter device is a Lambertian source and using 488 lm/W as the power conversion constant. The calculated optical power efficiency is also plotted in Fig. 3.9(b) with a maximum value of 0.020 W/A. The overall external upconversion efficiency can then be calculated by multiplying the detector responsivity (A/W) and the OLED optical power efficiency (W/A), and the results are plotted in Fig. 3.9 (c). It shows that the overall external upconversion efficiency started to become perceivable at a bias of around 5 V. It increased up to around 0.15 W/W at a bias of 12 V, which represents one order of magnitude improvement comparing to similar upconverter that relies on *p-i-n* Photodetector for light detection. To further confirm the optical upconversion from 1.5 μm to 545 nm, the output green light was measured over a device bias range of 2–12 V, under different NIR input power (see Fig. 3.10). A clear correlation between the output green light and the input NIR light is observed.

In this section, we have presented the design, fabrication, and characterization of a hybrid optical upconverter through direct tandem integration of a HPT and an OLED. A built-in electrical gain of 15 from the HPT was demonstrated and an overall external upconversion efficiency of 0.15 W/W was measured at room temperature.

3.3 Conclusion

The hybrid upconverter structure by the integration of OLED with InGaAs/InP photodetector has great potential application in night vision, search and rescue, however, the reported external upconversion was only 0.7%. In this chapter, new structures were proposed to improve the upconversion efficiency by enhancing OLED efficiency, carrier injection efficiency and photodetector efficiency. Firstly, with the insertion of an embedded metal mirror between the OLED layers and p-i-n InGaAs/InP inorganic photodetector. This special structure could significantly improve the performance of single devices by enhancing the photocarrier injection efficiency and the OLED efficiency, the upconversion efficiency of the hybrid organic/inorganic device was improved by more than 100%. Secondly, The incorporation of electrical gain through the integration of an HPT device and an OLED further enhanced the overall efficiency of the device by one order of magnitude. Nevertheless, there exists room for further improvement of device performance by optimizing the HPT design and device fabrication and by improving the OLED extraction efficiency [48-49]. The next goal is to achieve an overall upconversion efficiency of 1W/W or higher, leading to the use of the upconversion devices in practical imaging applications.

Chapter 4
Hybrid Optical Amplifier based on Optimized HPT/OLED

In chapter 3, NIR upconverters based on the integration of HPT and OLED were fabricated and characterized. The power efficiency was around 0.15 W/W, which had one order improvement over the device based on the integration of p-i-n PD with OLED. However, for detecting ultra-low intensity infrared scenes, the NIR upconverter with the capability of light amplification is attracting more interest. A light amplifier would become a key device for detecting, sensing and processing optical signals. In these devices, a high gain HPT is primarily required to drive an LED integrated on a substrate. In this chapter, we report a new upconverter structure which integrates a high gain p-n-p InGaAs/InP HPT and an OLED. Similar to previous hybrid upconverter devices, incoming 1.5 μm light is absorbed by the HPT component. The generated photocarriers are significantly amplified in the HPT before pumping into the OLED to emit visible light (green). With the incorporation of sufficient internal gain, the intensity of output visible light could be greater than that of the input NIR light.

The light amplification can be expected when the following condition is satisfied. The light amplification gain $G_0=P_{output}/P_{input}$ is written as

$$G_0 = \frac{(i/e)}{(P_{input}/h\nu_{input})} \bullet \frac{(P_{output}/h\nu_{output})}{(i/e)} = G\eta \qquad (4.1)$$

where, $P_{input,}$ and P_{output} denote the input and output light power, respectively, $G=(i/e)/(P_{input}/h\nu_{input})$ is the optical gain of the phototransistor, *and* $\eta=(P_{output}/h\nu_{output})/(i/e)$, the external quantum efficiency of OLED. Here, i denotes the current induced by the input light, e the magnitude of hole charge, h planck's constant, and ν the frequency of the light. We should have $G > 1/\eta$ to achieve a net positive gain $G_0 > 1$. By taking the loss of electron-hole pairs into account, G should be required to be much higher than $1/\eta$.

4.1 HPT Simulation

An HPT is basically a heterojunction bipolar transistor with a light sensitive collector and base region. Fig. 3.6 shows the schematic diagram of a p-n-p InGaAs/InP HPT structure. The incident light

on the device passes through the wide bandgap emitter and is absorbed in the base, base-collector depletion region and collector. The electron-hole pairs generated in the base/collector depletion region and within the diffusion lengths of the minority carriers in the base and collector will be separated and collected by the field of base/collector junction leading to a current flow in the external circuit. The electrons are swept into the base and are accumulated there due to a large potential barrier in the conduction band until they recombine with injected holes from emitter. To maintain the charge-neutrality condition in the base, a large injection of holes occurs from the emitter into base.

The overall optical gain can be expressed as follows,

$$g = \frac{I_C}{q}\frac{h\nu}{P_{in}} = \eta(1+\beta) \qquad (4.2)$$

here $h\nu$ is the photon energy at the incident light wavelength, P_{in} incident light power, I_C collector current, η the quantum efficiency, and β the common emitter current gain, which is governed by emitter injection efficiency and base transport factor,

$$\beta = [\cosh(\frac{w_B}{L_n}) - 1]^{-1} \qquad (4.3)$$

$$\eta = (1-R)[1 - \frac{\exp(-\alpha w_B - \alpha w_{BC})}{\alpha L_p + 1}] \qquad (4.4)$$

where w_B is the base width, w_{BC} base-collector depletion width, R reflection at the InP-air interface, α absorption efficiency and L_P is the hole diffusion length in the base layer. In this case, the current gain is determined by the base width (w_B) [50-51]. The exponential term in (4.3) and (4.4) suggests that for high g and η, most of the incident photon flux should be absorbed in the base and base-collector depletion region. The presence of L_p indicates that the hole-diffusion length should be large for efficient collection of holes. The thinner the base layer, the higher the current gain β. However, the η will decrease and therefore the absorption of the input signal must be taken into account. The signal must be absorbed in the base or base-collector depletion region in order to be electro-optically amplified. The optimal choice of w_B will be a compromise in which the base layer yields sufficient gain and sufficient optical absorption simultaneously. The second device structure optimization point of this work is achieved by adopting double emitter layers (high-low doping profiles) to suppress recombination current at the interface of the emitter/base, so that the hole injection efficiency could be improved. It is well known that in the high-current region, the recombination current is negligible

compared with the diffusion current; but at low optical power, the photocurrent gain of a typical HPT is mainly limited by recombination, so the suppression of the major recombination source is key to the improvement of the sensitivity of HPTs. The design of the emitter/base heterojunction can be classified into two categories: composition-graded and composition-abrupt junction. Ideally, the insertion of a composition-graded region at the emitter/base junction can eliminate the potential energy spike at the emitter side and thus increase the emitter injection efficiency. However, the recombination current is also greatly enhanced in this case. The recombination current at the emitter/base can be reduced by placing "composition-abrupt" double emitter layers with high-low carrier concentration profiles [52].

The initial device simulation study was done using SimWindows, a drift-diffusion simulator. Analysis was achieved by self-consistent numerical solution of the Poisson, carrier continuity and current density equations subject to the device's geometry and boundary conditions imposed by the device's contacts and biasing conditions [53]. Three structures were designed and simulated for optimizing the device performance [Fig. 4.1]. In structure 1, the thickness of the base layer is 50 nm and the emitter is formed by high-low doping double layers, which are expected to reduce the recombination current (leakage current). Structure 2 has a thicker base (100 nm), but with the same high-low doping double emitter layers as structure 1 for studying the effect of base thickness. Structure 3 has a higher doping profile in the second emitter layer and the thickness of the base layer is 100 nm. Other parameters are the same. Fig. 4.2(a) shows the simulated current-voltage (I-V) characteristics of the three structures under 1.2 mW/cm^2 infrared illuminations. At 1 V bias, the responsivities were 59 A/W, 50 A/W and 10 A/W for structure 1, structure 2 and structure 3, respectively. Comparing structure 1 and structure 2, the improved device performance could be attributed to the reduced thickness of the base layer. By the formation of a high-low composition abrupt junction in emitter layers, structure 2 exhibits 3 times improvement over structure 3. The high-low double emitter layers could reduce the recombination current at the interface of the emitter/base to improve the optical gain of the HPT significantly. Simulated I-V characteristics of structure 1 under different input optical illumination conditions are shown in Fig. 4.2(b). For bias below 0.6 V, device current increased rapidly with bias. After that, device current increased slowly with bias and the saturation current was controlled by the input optical power. Based on the simulated results, structure 1 was chosen as the optimized HPT.

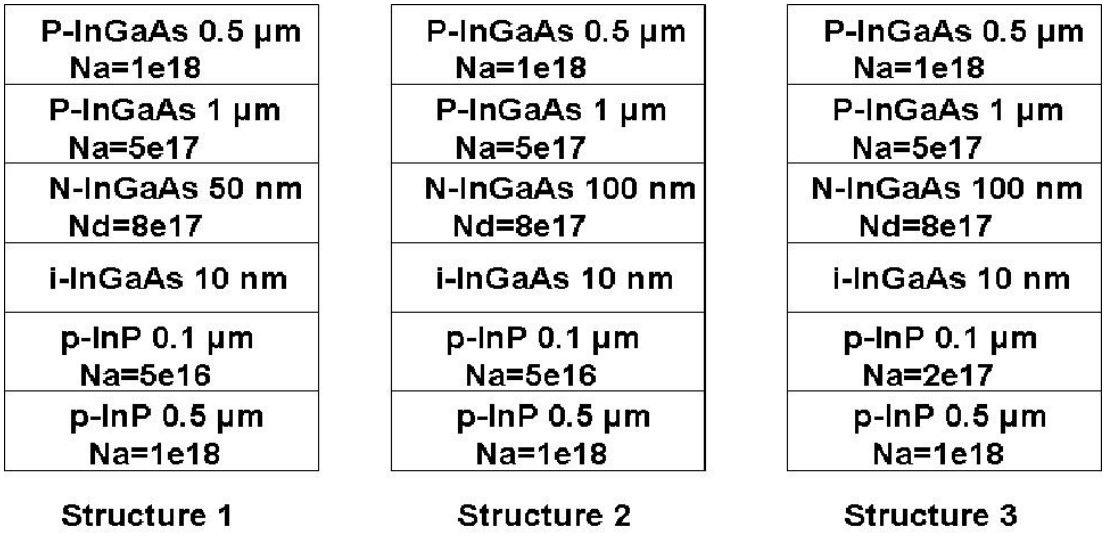

Figure 4.1 Schematic diagram of the three configurations of p-n-p InGaAs/InP HPT (structure 1, structure 2 and structure 3).

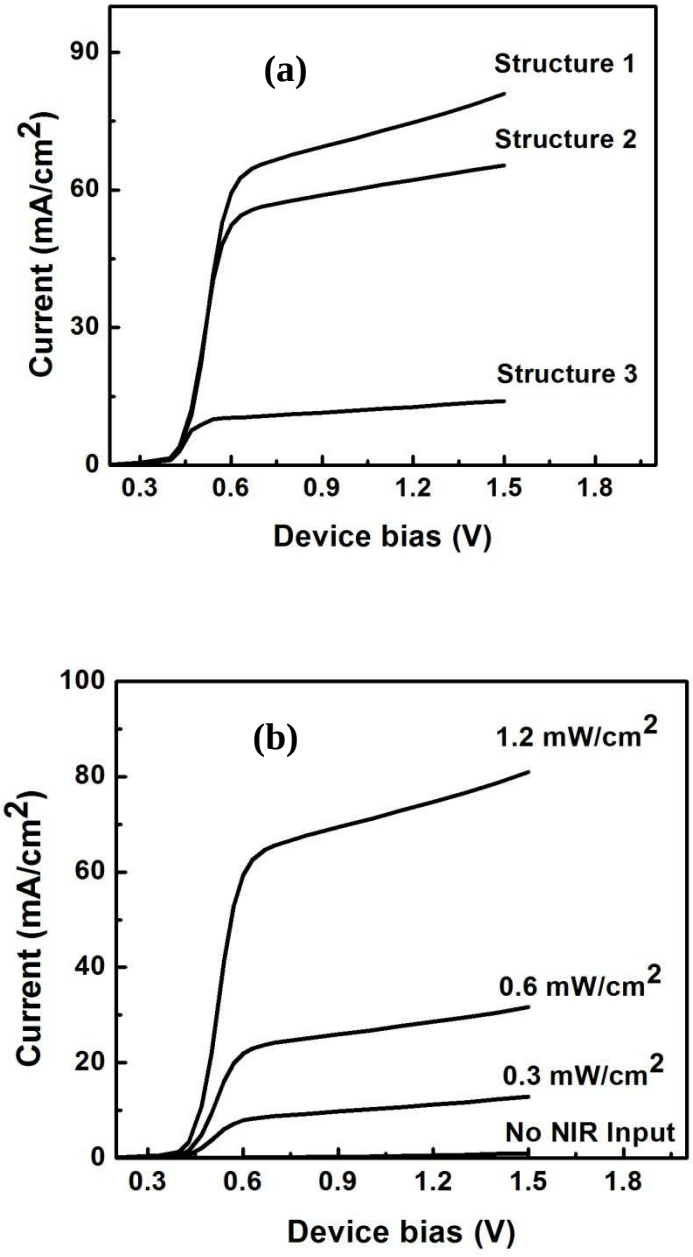

Figure 4.2 (a) Simulated I-V relationships of three HPT structures under NIR illumination of 1.2 mW/cm^2; (b) Simulated I-V relationships of HPT (structure 1) under different NIR illumination conditions (1.2 mW/cm^2, 0.6 mW/cm^2, 0.3 mW/cm^2 and no NIR).

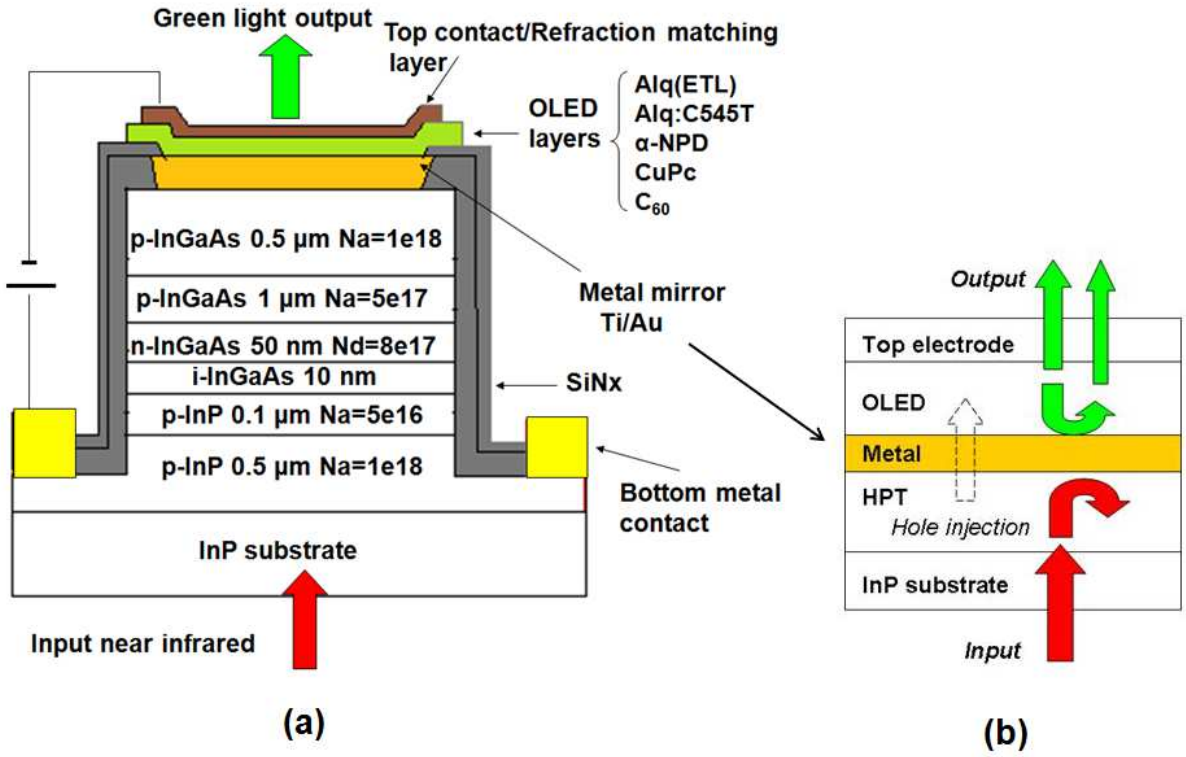

F

Figure 4.3 (a) Schematic cross section of hybrid optical upconverter device with integrated InGaAs/InP HPT and OLED. Note that the thickness of the organic and inorganic layers is not to scale. The embedded mirror layer consists of 20-nm Ti and 100-nm Au. The hole injection layer (HIL) of the OLED was a 3-nm thick layer of fullerene (C_{60}). The hole transport layers (HTLs) consisted of copper phthalocyanine (CuPc) (25 nm) and N,N'-diphenyl-N,N'-bis-(1-naphthyl)-1-1'-biphenyl-4,4'-diamine (α-NPD) (45 nm). The 30 nm thick emission zone was tris-(8-hydroxyquinoline) aluminum (Alq), doped with 1 wt.% 10-(2-benzothiazoly)-1,1,7,7-tetramethyl-2,3,6,7-tetrahydro-1H, 5H, 11H-[1]benzo-pyrano [6,7,8-ij]quinolizin-11-one (C545T). The electron transport layer (ETL) was made of an additional 15 nm thick Alq layer. The top metal contact consists of LiF (1 nm)/Al (5 nm)/Ag (15 nm). Finally a 45-nm thick Alq layer was refractive-index matching layer. No antireflection coating was applied to the back side of the InGaAs/InP sample. (b) The insertion of a highly reflective metal layer as an embedded optical mirror could improve the absorption and emission efficiency.

4.2 Device Fabrication

The optimized HPT was grown by chemical beam epitaxy (CBE) on a semi-insulting InP substrate and integrated with an OLED to form a hybrid upconversion device [Fig. 4.3(a)]. The wafer growth started with an 500-nm InP emitter contact (*p*+, 1×10^{18} cm^{-3}) and a 100-nm InP emitter layer (*p*, 5×10^{16} cm^{-3}). The growth continued with a 10-nm undoped InGaAs spacer and a 50-nm InGaAs base layer (*n*, 8×10^{17} cm^{-3}). Then came a 1-μm InGaAs collector layer (*p*, 5×10^{17} cm^{-3}). The structure was capped with a 500-nm InGaAs contact layer (*p*+, 1×10^{18} cm^{-3}). Si was used as the n-type dopant and Zn was used as the p-type dopant for the epilayers.

The first step of the device fabrication was to pattern and etch square mesas (1×1 mm^2) onto the p-InP emitter. Square mesas were patterned using standard photolithography. A solution of H_2SO_4: H_2O_2: H_2O (1:8:160) was used to etch the InGaAs layer (~1.6 μm thick) and another solution of H_3PO_4: HCl (10:1) was used to etch part of the p-InP layers (~0.2 μm thick) to complete the square mesas. A 150-nm Si_3N_4 layer (SiN) was then grown on the top surface of the InGaAs/InP sample using plasma-enhanced chemical vapour deposition (PECVD). The SiN outside of the square mesa was etched off to form an open area, where a metal layer (Ti/Au) was deposited to serve as a common bottom contact. Square windows with a size of 0.9×0.9 mm^2 were patterned using photolithography on top of the square mesas and chemically etched onto the SiN layer. The etching went through the entire SiN insulation layer to expose the semiconductor square mesa areas, on top of which an embedded metal mirror (Ti 20 nm/ Au 100 nm) was deposited using electron-beam evaporation [Fig. 4.3(b)] to form a good contact and also to enhance input light absorption efficiency as well as output light emission efficiency. A second SiN layer was deposited to bury the metal mirror and was later partially etched off to expose a smaller window (0.8×0.8 mm^2) right on the top of the metal mirror. The second SiN layer was mainly for minimizing potential leakage current, which could significantly degrade device performance.

The InGaAs/InP substrate was then ultrasonically cleaned with a standard regiment of chloroform, acetone and methanol followed by ultraviolet (UV) ozone treatment for 30 minutes. Thereafter the sample was loaded into a Kurt J. Lesker LUMINOS® cluster tool for deposition of the OLED. All molecular films were deposited sequentially through a shadow mask (15×15 mm^2 opening) over the entire top surface of the substrate. Semi-transparent cathode metal electrodes (1.2 mm in diameter) were deposited on the top of the square mesa structures using a second shadow mask, without breaking vacuum. The top cathode layer was composed of LiF (1.0 nm)/Al (5.0 nm)/Ag (15 nm),

which has an adequate sheet conductance, and is partially transparent to green light. Finally a 45 nm thick Alq3 layer was deposited, which could provide a better index of refractive-index matching from the LiF/Al/Ag to air. Current-voltage-luminance (I-V-L) characteristics of the fabricated devices were measured with an HP 4140B picoammeter and a Minolta LS-110 luminance meter. The input 1.5 μm light was from a MPS-8033 precision fiber optic source. All measurements were conducted at room temperature, and under normal atmospheric condition.

4.3 Device Analysis

Fig. 4.4 shows the luminance-voltage (L-V) curve of this upconversion device under 1.5 μm infrared illumination with a power density of 1.2 mW/cm^2. Incoming 1.5 μm optical radiation was absorbed by the HPT, generating an amplified photocurrent. The resultant photocurrent drove the OLED that emits green light. The integrated device started to turn on at a low bias (~6 V). This shows that efficient hole injection from the semiconductor to the organic layers was achieved via the floating metal contact (also the embedded mirror). The inset of Fig. 4.4 is the image of the hybrid upconverter operating at 15 V with input NIR from bottom. As the device bias continued to increase, the output luminance of the green emission increased rapidly up to 9000 cd/m^2. The rapid increase of the luminance is mainly due to the increase of the photocarrier collection efficiency and internal electrical gain, which was enhanced by the additional external voltage that dropped across the HPT component.

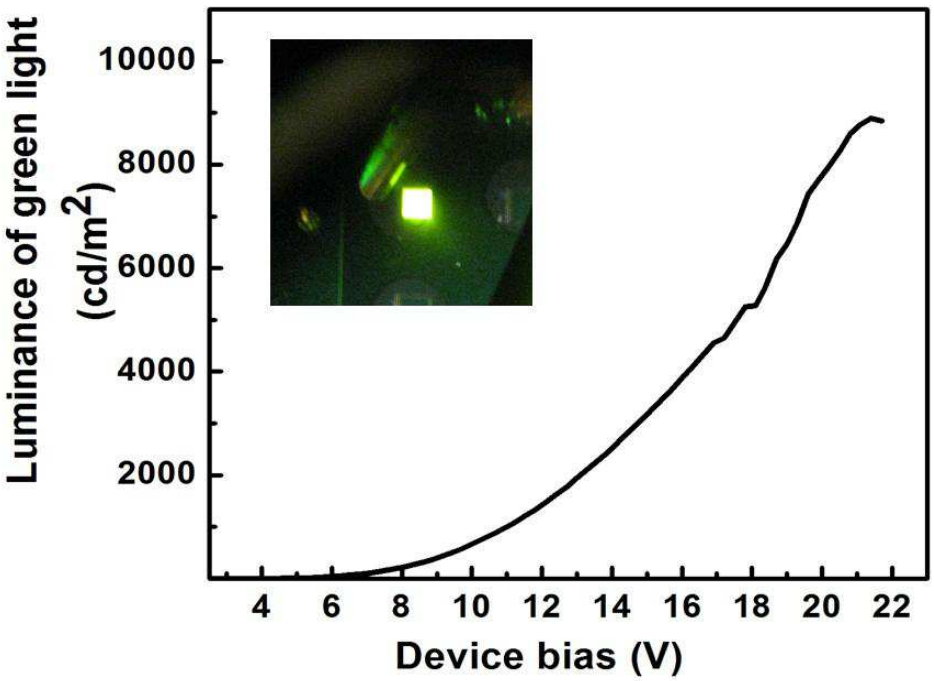

Figure 4.4 Luminance-voltage (L-V) curve of upconverter under 1.5-μm infrared illumination, with NIR power density of 1.2 mW/cm^2 [inset: image of hybrid upconverter operating at 15 V with input NIR from bottom].

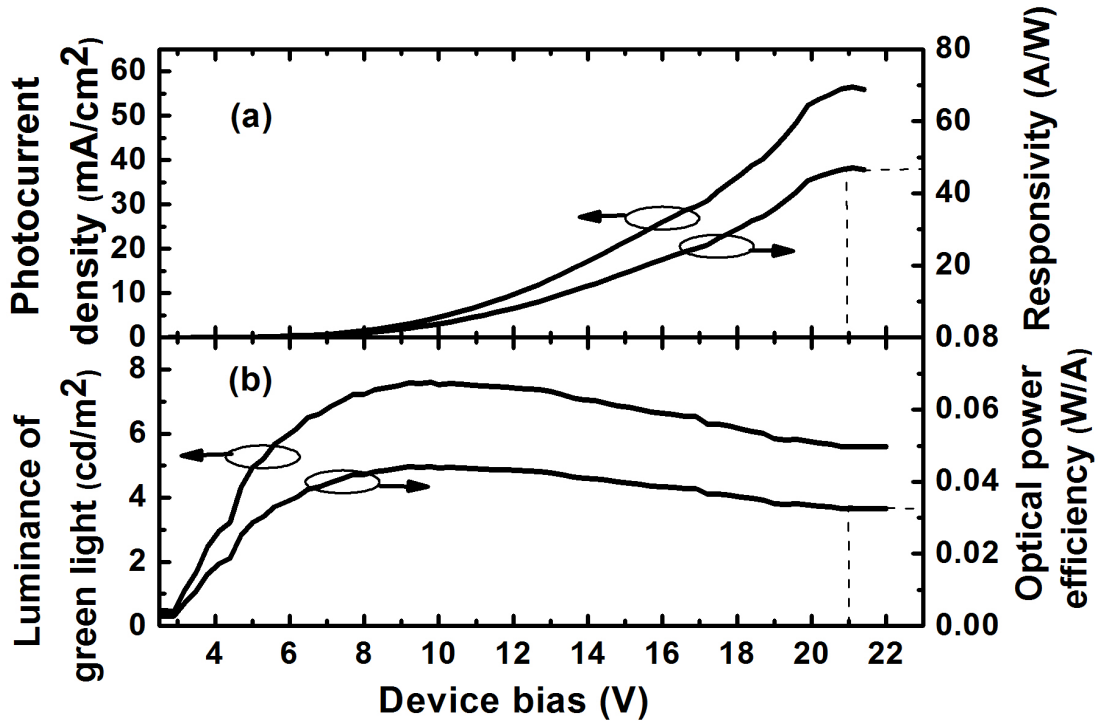

Figure 4.5 (a) Measured photocurrent density (mA/cm^2) as a function of device bias under 1.5-μm infrared radiation of 1.2 mW/cm^2 and the calculated responsivity (A/W) of the HPT component. (b) Measured luminance efficiency (cd/A) of the OLED component of the integrated upconverter and the calculated optical power efficiency (W/A).

Fig. 4.5(a) shows the measured photocurrent density (total current density minus dark current density) as a function of device bias under 1.5 μm infrared radiation (1.2 mW/cm^2), together with the calculated responsivity of the HPT component. The responsivity started to rise at 6 V and gradually increased with further increase of the device bias. At 21 V bias (the total voltage dropped across the HPT component and the OLED component), the responsivity was measured to be 47 A/W under input infrared radiation of 1.2 mW/cm^2. In comparison, the responsivity of an InGaAs/InP p-i-n PD with similar absorbing layer thickness is around 0.5 A/W at a bias of ~1-2 V. The electrical gain of the HPT component of the hybrid upconverter was therefore estimated to be 94. Fig. 4.5(b) shows the measured current efficiency of the OLED part of the hybrid upconverter. The luminance efficiency first increased with the device bias. At ~10 V, it reached a maximum value of 7.6 cd/A, and then it decreased slowly with further increasing device bias. The luminance efficiency (cd/A) can be converted to OLED external power conversion efficiency (W/A) by assuming that the upconverter device is a Lambertian source and using 540 lm/W as the power conversion constant. The calculated optical power efficiency is also plotted in Fig. 4(b) with a value of 0.033 W/A under 21 V bias. The overall external upconversion efficiency can then be calculated by multiplying the detector responsivity (A/W) and the OLED optical power efficiency (W/A), so the calculated value is 1.55 W/W at a bias of 21 V, which means the power of the output green light is 1.55 times of the input infrared light. The device exhibits optical upconversion with a power amplification. The NIR-to-visible photon conversion efficiency (η_{con}) can be calculated as follows,

$$\eta_{con} = \frac{\#of\ output\ photon}{\#of\ input\ photon} = \frac{\frac{P_{vis}}{h\nu_{vis}}}{\frac{P_{NIR}}{h\nu_{NIR}}} = 1.55(W/W) \times \frac{h\nu_{NIR}}{h\nu_{vis}} \qquad (4.5)$$

where P_{NIR} is the input light power, P_{vis} the output visible-light optical power, $h\nu_{NIR}$ the NIR photon energy (=0.83 eV), and the averaged output visible photon energy, which is weighted by the relative emission spectrum intensity.

Fig. 4.6 shows the OLED emission spectrum of the integrated upconverter, which is peaked at 2.2 eV (the corresponding wavelength is 564 nm). The spectrum covers a wide range from 1.6 eV to 2.8 eV in photon energy. The averaged output photon energy is calculated by weighting the photon energy with the relative intensity of the emission spectrum, as shown below

$$\overline{h\nu_{output}} = \frac{\int_{1.6eV}^{2.8eV} h\nu \bullet Spectrum\_Intensity \bullet d(h\nu)}{\int_{1.6eV}^{2.8eV} Spectrum\_Intensity \bullet d(h\nu)} = 2.18 \text{ eV} \qquad (4.6)$$

η_{con} is calculated to be 2.18 eV, and the NIR-to-visible photon conversion efficiency is 59%.

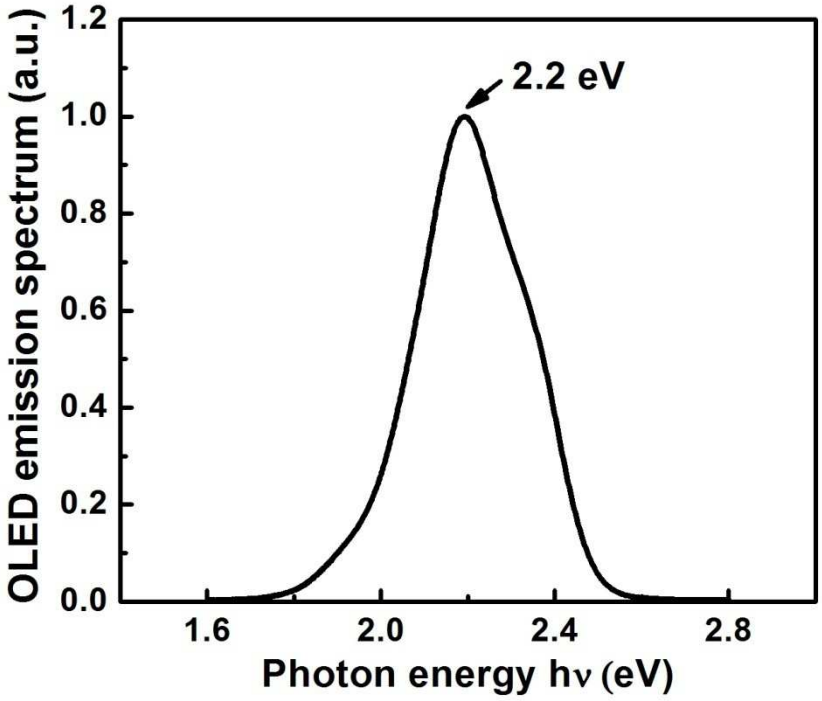

Figure 4.6 the emission spectrum of output visible light

To demonstrate the NIR-to-visible light upconversion operation, the intensity of the output OLED emission was measured with different input NIR power densities. The results are plotted in Fig. 4.7. Under dark condition (i.e., no input NIR illumination), the luminance of the green light emission from OLED is very low below a bias of 12 V. It increased above 12 V due to the amplified dark current by the HPT component. Possible origins of the dark current are structural defects from wafer growth and interface states formed at the integration of the HPT with the OLED, which needs to be clarified and suppressed for further improvement in device performance. With NIR illumination, the output luminance of the device became evident at a bias of ~9 V. As the NIR input power density increased from 0.12 to 1.2 mW/cm^2, the values of the output luminance at 21 V increased from ~4100 to ~9000 cd/m^2, clearly demonstrating the upconversion operation of the hybrid device at room temperature.

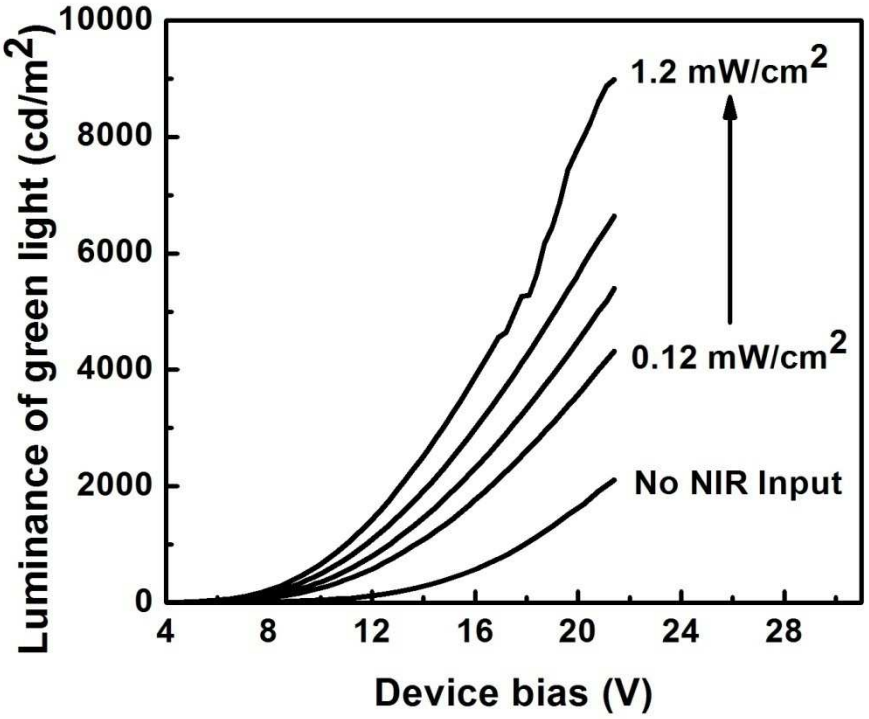

Figure 4.7 NIR-induced green light luminance as a function of device bias under different NIR illumination conditions (0.12 mW/cm^2, 0.3 mW/cm^2, 0.6 mW/cm^2, 1.2 mW/cm^2).

4.4 Conclusion

A NIR (1.5 μm) to visible light (green) electrooptical upconverter with amplified power gain has been designed and demonstrated. The device was fabricated by direct tandem integration of an OLED with an inorganic InGaAs/InP HPT. A built-in electrical gain of 94 from the HPT was achieved and an overall external power efficiency of 1.55 W/W was measured at room temperature. This demonstration gives us strong confidence to exploit the utility of organic/inorganic hybrid semiconductor system in making low-cost, large-area and high-efficiency NIR upconversion imaging devices. With the upconversion approach, imaging device can be realized with the tandem integration of an inorganic pixelated HPT array and a large-area single-element OLED. The continuous OLED layers on top of the HPT pixel array are expected not to cause significant lateral current spreading due to their poor lateral electrical conductivity and very thin thickness (~100-200 nm). The spatial resolution of the imaging device is mainly limited by the pixel size of the HPT part. The visible light emission from each individual pixel is triggered by the detection of input NIR radiation.

4.5 Further Improvement

From section 4.3, in contrast to Photodetector, HPT is highly advantageous for obtaining higher sensivity since it has the amplification function of photocurrent. However, the dark current could also be amplified same as photocurrent so that the dark current becomes the source of noise and reduces the sensitivity of photodetection. Therefore, suppressing the dark current is very important for realizing a highly sensitive HPT. Here, the dark current generated in the reversely biased base-collector junction is discussed, which drifts to the base layer and then is amplified. This dark current is dominated by the minor carriers density in collector layers. If we increase the doping of first p-InGaAs collector layer from 5×10^{17} cm^{-3} to 1×10^{18} cm^{-3}, the minor carriers density in that layer will decrease. The initial device simulation study is done using SimWindows. Two structures are simulated for reducing the dark current by changing collector doping levels [Fig. 4.8]. Fig. 4.8(b) shows the simulated current-voltage (I-V) characteristics of the two structures under no illumination and (c) under 2.2 mW/cm^2 infrared illuminations. At 1.4 V bias, dark current was reduced from 0.77 mA/cm^2 to 0.35 mA/cm^2 [Fig. 4.9]. Comparing structure 1 and structure 2, while the total current was increased from 200 mA/cm^2 to 265 mA/cm^2 [Fig. 4.10]. The simulated responsivity was 120 A/W and signal to noise ratio was 760 at the applied bias of 1.4 V. There are also other some possible origins of the dark current including structural defects from wafer growth and interface states formed at the integration of the HPT with the OLED.

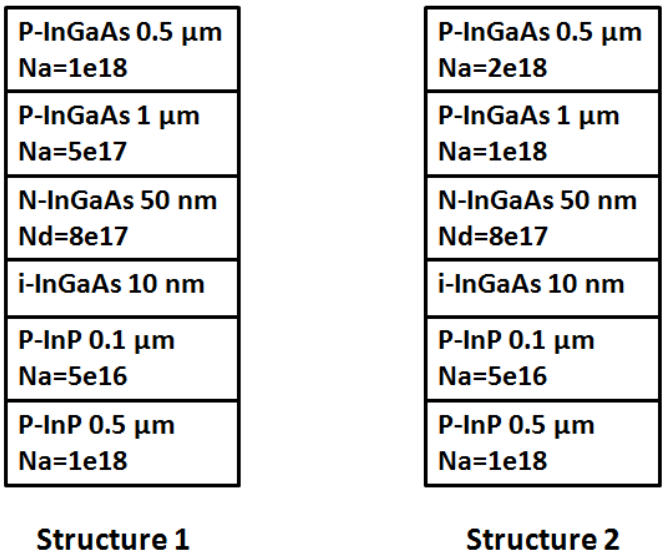

Figure 4.8 Schematic diagram of the two configurations of p-n-p InGaAs/InP HPT structure 1 (the structure in section 4.2) and structure 2.

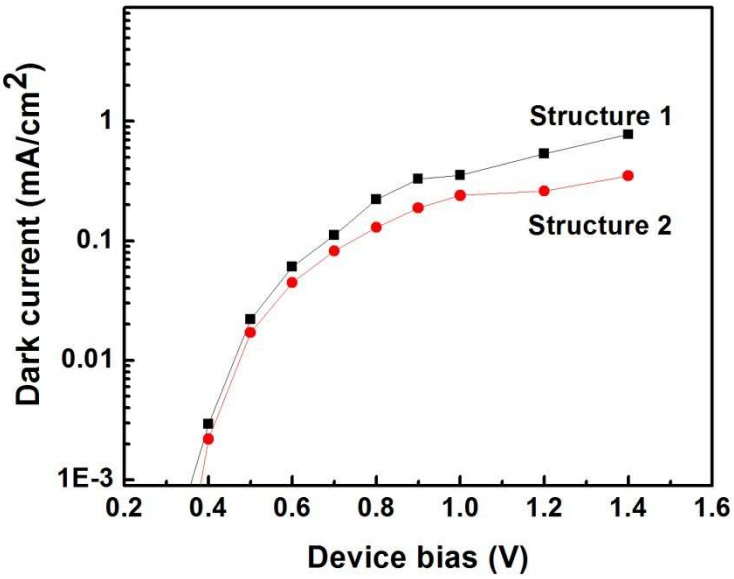

Figure 4.9 Simulated I-V relationships of two HPT structures under no NIR illumination.

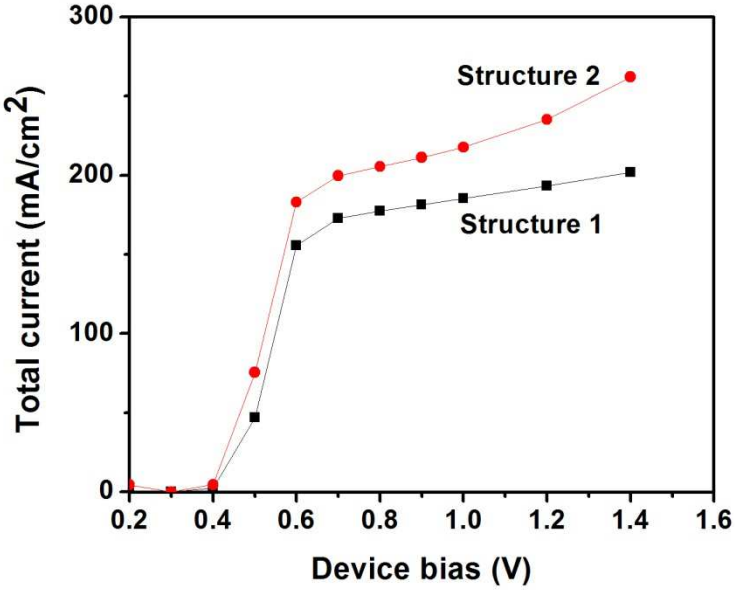

Figure 4.10 Simulated I-V relationships of two HPT structures under 2.2 mW/cm^2 NIR illumination.

Chapter 5
Hybrid Upconversion Imaging Devices

5.1 Motivation

Imaging devices in the NIR have become increasingly important in many applications, such as night vision, biomedicine, homeland security and semiconductor wafer inspection. A typical imaging device comprises a two-dimensional array of photodetectors in combination with a Si ROIC. Unfortunately, the process technology for NIR detector materials is incompatible with the technology to process the ROIC. Consequently two separate chips are required to form a hybrid imaging device by indium bumps in a one-to-one correspondence. This indium bump technology is a "one-piece-at-a-time" process and there are many factors that limit its yield and size-scalability. Indium bump bonds increase the power consumption and also the pixel-to-pixel capacitance thereby increasing the array noise. In addition, to fabricate large-area/scale pixel arrays, the size of each individual pixel has to be reduced, imposing stringent requirements on pixel alignment. To overcome the limitations of the current infrared imaging device, photo upconversion devices have been proposed and developed for several years, which converts NIR radiation to a shorter wavelength (e.g., 1 μm or below) that can be effectively detected by a conventional silicon (cutoff wavelength about 1 μm) CCD. Such an optical up-converter combines with a commercially available CCD functions as an ordinary infrared camera. There are several up-conversion techniques developed by now, including thermally excited upconversion, rare-earth upconversion, Photodetector- LED.

Kim et al. reported an all organic infrared upconversion device realized by integrating a tin phthalocyanine (SnPc):C_{60} bulk heterostructure NIR Photodetector and a fac-tris(2-phenylpyridinato)iridium (III) (Irppy3) phosphorescent organic light-emitting diodes (OLEDs). While the upconversion process was simplified, these organic NIR Photodetectors have no infrared sensitivity beyond 1 μm. More recently, the same group reported a hybrid organic/inorganic upconversion device with infrared sensitivity up to 1.5 μm by using an inorganic colloidal PdSe nanocrystals as a NIR sensitizer [54]. These upconverter can be a standalone device to convert invisible infrared light into the visible light, however, they are difficult to be operated in combination with Si CCD, since the input NIR and the output visible light are in the same side. Moreover, they are still single-element device, which cannot accomplish two dimensional NIR imaging upconversion. In chapter 4, the maximum reported hybrid NIR-to-visible photon conversion efficiency was up to 60% by an InGaAs/InP heterojunction phototransistor with an OLED, which had electrical gain (~94) in

HPT component. However, the interconnection region between the NIR Photodetector and OLED was heavily p-doped InP or metal layer, which could result in substantial lateral current spreading. Therefore, these layer structures can be used in imaging devices only in a two dimensional pixel array format, in which each single pixel consists of a photodetector and an OLED, and neighboring pixels are electrically insulating. It is, however, complicated and costly to fabricate two dimensional pixelated arrays.

5.2 Hybrid Pixelless Imaging Device

In this section, targeting to make low-cost, large-area upconversion device which operates in the 1.5 μm region (e.g. covering 1.2-1.6 μm) and also can combine with a Si CCD, a novel organic/inorganic hybrid pixelless upcoversion imaging device is discussed, which consists of a single-mesa large-area hybrid upconversion device, where the OLED output is spatially correlated with the input 1.5 μm scene. This hybrid imaging device was realized by the integration of an i-$In_{0.53}Ga_{0.47}As/C_{60}$ hybrid photovoltaic junction and an OLED. The i-$In_{0.53}Ga_{0.47}As/C_{60}$ hybrid junction could absorb input 1.5 μm NIR scene while also drastically reduce lateral carrier diffusion since the interconnection region is completely depleted under operating bias. The results clearly show room temperature up-conversion operation and a pixelless image was captured using a Si CCD. This device is the first organic/inorganic hybrid infrared imaging device reported so far.

5.2.1 Device Working Mechanism

A pixelless hybrid upconversion device consists of a single large-area mesa, where the OLED output is spatially correlated with the input 1.5 μm scene. Only the parts receiving incoming photons will emit output photons (see Fig. 5.1). Therefore the challenge in fabricating a NIR Photodetector/OLED pixelless imaging device is to suppress the lateral carrier diffusion in the interface while preserve effective electrical interconnection between the Photodetector and OLED. To achieve this functionality, photon-generated carriers must flow mainly in the vertical direction when injected from the InGaAs light absorption layer, through the top InP cladding layer, into OLED light emission layer. The injection of holes from the InP layer of detector component is modulated by incoming 1.5 μm light. The result is an upconversion of a near infrared signal to a visiable light. The visible output can then be imaged by a well developed device such as a Si CCD camera [16].

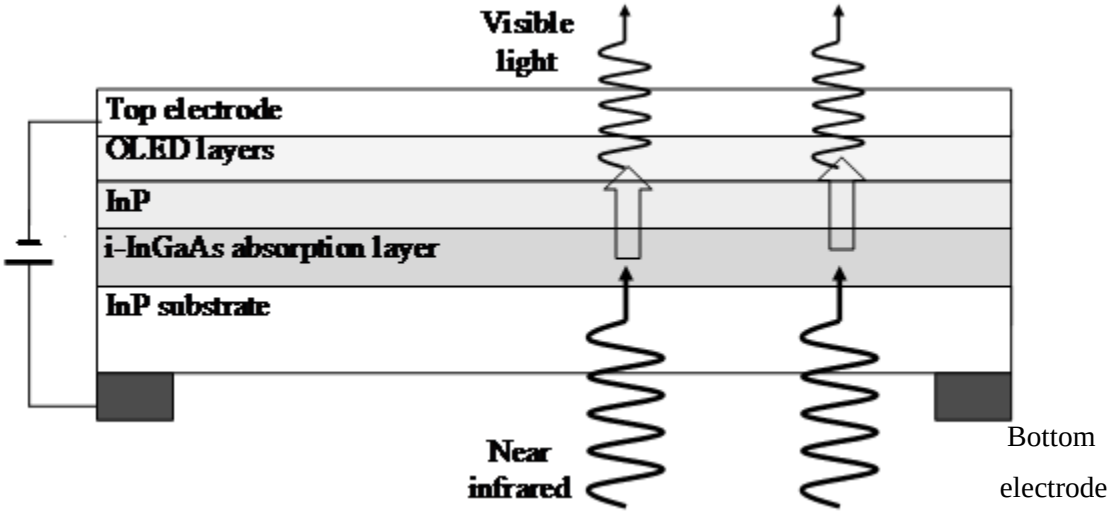

Figure 5.1 Schematic structure of the cross-section of a pixelless device.

The benefit of this approach is its simplicity in device structure and device fabrication: no pixel array needs to be fabricated into the InGaAs/InP wafer. The successful demonstration of pixelless imaging operation will allow us to grow and fabricate large-area (10×10 mm^2 or larger) upconversion imaging devices for low cost.

Besides the reduction of lateral carrier diffusion in Photodetector part, the lateral electrical conductivity in OLED layers is also very important element in pixelless operation. The continuous OLED layers across the pixel arrays are not expected to cause significant lateral current spreading due to their poor lateral electrical conductivity and very thin thickness (~100-200 nm).

The fabrication of large area pixelless device requires high uniformity. The pixel uniformity is mainly determined by uniformity of photodetector part and OLED layers. The uniformity of film thickness can be characterized by the following formula:

$$[(\text{Max}-\text{Min})/(\text{Max}+\text{Min})] \times 100\% \qquad (5.1)$$

where Max and Min in the equation are the maximum and minimum values of film thickness, respectively. Utilizing formula 5.1, we can characterize the uniformity of film thickness. It is well known that the III-V compound semiconductor material epitaxial growth technology is mature and a typical three inch wafer is very uniform. Detailed measurements show thickness variation across a three inch wafer is smaller than 1%. The doping concentration nonuniformity is also typically within 1%. So the intrawafer uniformity is expected to be very excellent.

The enlargement of substrates requires the improvement of the evaporation system design to control the uniformity of the organic film thickness for large substrates. Many investigations have been done to optimize the uniformity of such thickness in substrates for a sputtering process, pulsed arc process, and other processes. Also process simulation model was developed to predict the film thickness distribution by understanding system design parameters that affect the uniformity of film thickness. Based on those methods, the uniformity of the thickness in an organic layer was successfully controlled [55].

5.2.2 Photovoltaic Effect of the i-InGaAs/C_{60} Schottky Junction

A novel hybrid optical upconversion device is proposed for the first time, which integrates an i-$In_{0.53}Ga_{0.47}As/C_{60}$ heterojunction with an OLED. This new structure is expected to minimize lateral current spreading. In this section, a single-mesa small area device (0.8×0.8 mm^2) is fabricated and characterized to demonstrate the photovoltaic effect.

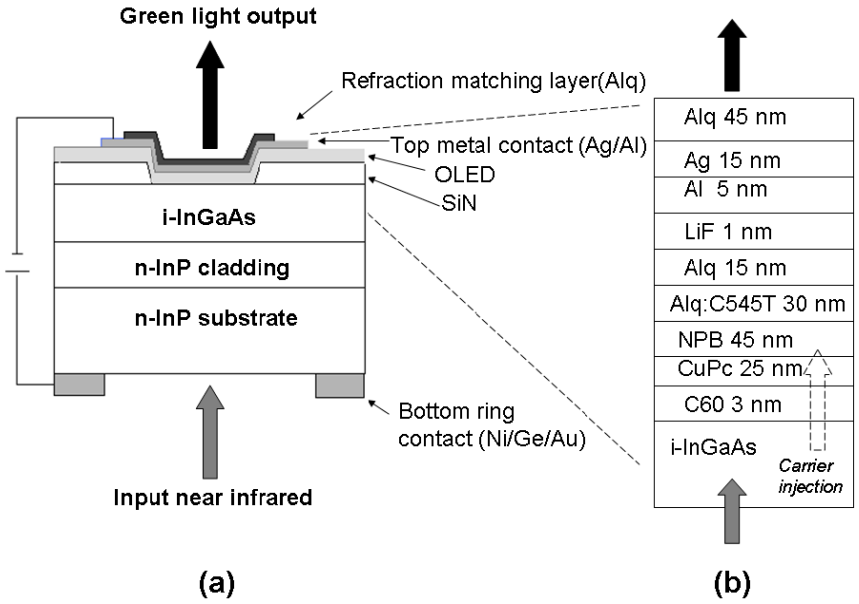

Figure 5.2 (a) Schematic cross section of an inorganic-organic upconverter device; (b) Schematic configuration of the OLED layers. The layer thickness is not to the scale. C_{60} is carbon fullerene. CuPc stands for copper phthalocyanine. NPB is N, N'-di(naphthalene-1-y1)-N,N'-diphenyl-benzidine, Alq is tris-(8-hydroxyquinoline) aluminum. Alq:C545T is the light emission layer.

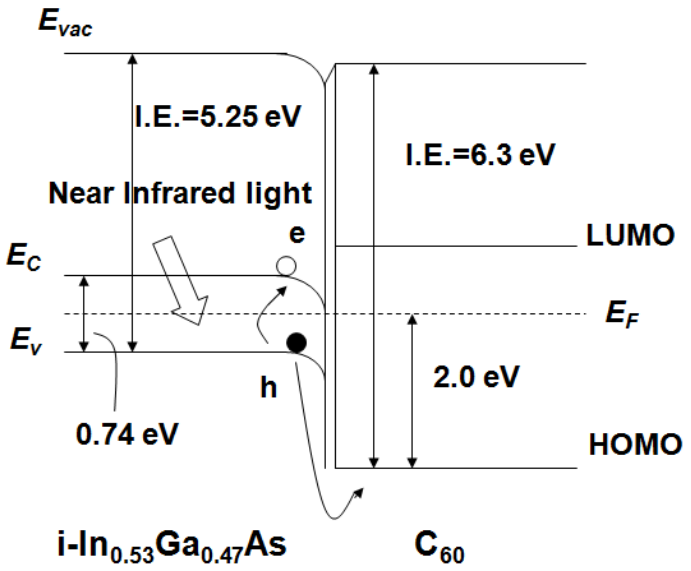

Figure 5.3 Schematic band diagram across the interface

Fig. 5.2 shows a schematic diagram of the cross section of one fabricated device and Fig. 5.3 is the schematic band diagram of the cross section. The 1-μm-thick intrinsic $In_{0.53}Ga_{0.47}As$ was grown on an n-type InP substrate by MOCVD. A SiN insulating layer (~200 nm) was first deposited on the top surface of InGaAs, followed by patterning and etching square windows with a size of 0.8×0.8 mm^2, where the OLED layers were later-on deposited. A ring metal contact (Ni/Ge/Au) was deposited on the back side of the n-InP substrate as a common bottom contact. The OLED layers were deposited using a Kurt J. Lesker Cluster Tool. All measurements were conducted at room temperature, and under normal atmospheric condition.

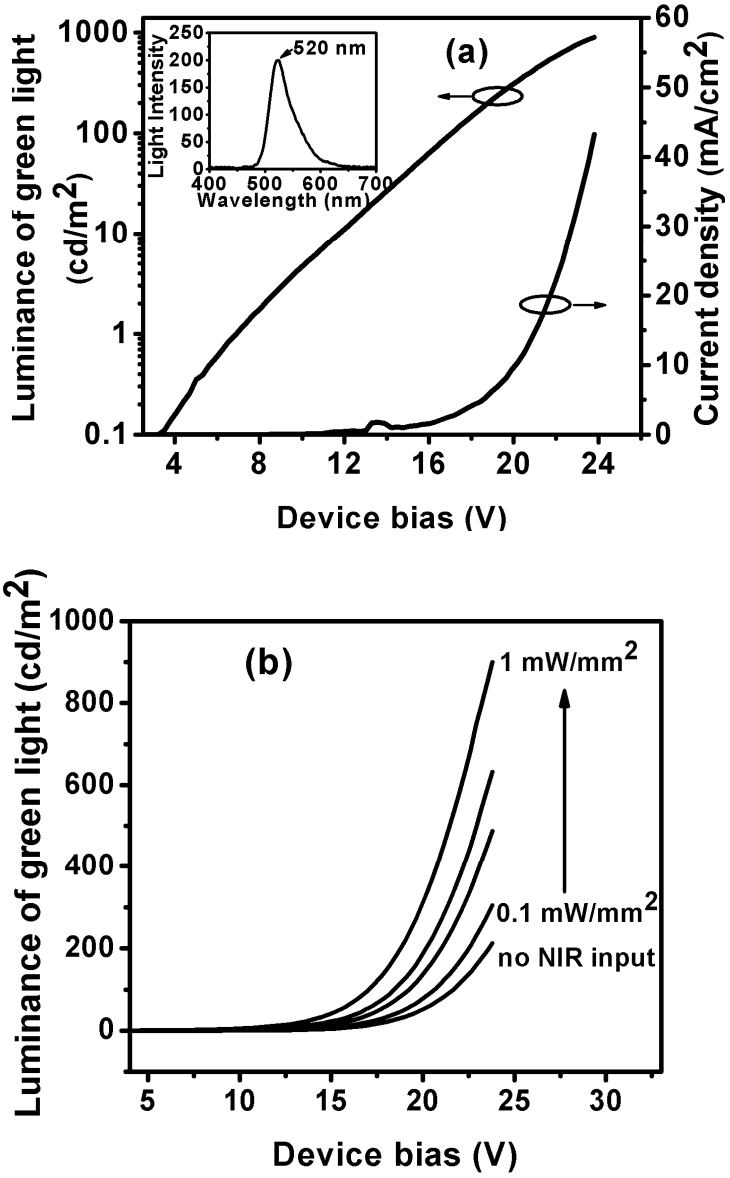

Figure 5.4 (a) Current-voltage-luminance (I-V-L) curves of the upconversion device under 1.5 μm infrared illumination (input power density 1 mW/mm^2); the inset shows the emission spectrum from the OLED of the integrated upconverter peaked at 520 nm in wavelength (green light); (b) NIR-induced green light luminance as a function of device bias under different illumination conditions.

Fig. 5.4 (a) shows that the current density (photocurrent density plus dark current density) started to rise at a bias of around 12 V and the output luminance of the green emission increased up to 930 cd/m^2 at 24 V under an input infrared power density of 1mW/mm^2. This luminance is around 4 times higher than that under a dark condition (no NIR input) at 24V. The photoresponse and light intensity dependence clearly show the photovoltaic effect of i-$In_{0.53}Ga_{0.47}As/C_{60}$ heterojunction under external bias. Incoming 1.5 μm light was absorbed by the i-$In_{0.53}Ga_{0.47}As/C_{60}$ heterojunction to generate photocurrent and the photo-induced charge carriers were efficiently injected into the emission layer of the OLED to emit green light. This photovoltaic effect has already been observed in other similar inorganic/C_{60} hybrid semiconductor junctions [56]. The separation between the HOMO and LUMO of C_{60} is 2.6 eV. The HOMO and LUMO levels can be set at -1.82 eV and 0.78 eV, respectively, with respect to the Fermi level (E_F) [57]. Bandgap calculation results show that the hole injection energetic barrier from the i-$In_{0.53}Ga_{0.47}As$ to C_{60} is around 1.4 eV. This large energetic barrier could be the reason that the turn-on voltage of this device is approximately 1-2 V higher than that (~10V) of an OLED integrated with p-i-n InGaAs/InP Photodetector [Fig. 5.3]. The overall external upconversion efficiency of this device is measured to be ~0.4% W/W at a bias of 24 V (under 1 mW/mm^2 NIR illumination), derived from experimental data by multiplying the detector's responsivity (A/W) and the OLED optical power efficiency (W/A).

To demonstrate NIR's visible light upconversion operation, the intensity of the output OLED emission was measured under different input NIR power densities (Fig. 5.4(b)). Under the dark condition (no NIR input), the luminance of the green light emission from OLED is around 200 cd/m^2 at a bias of 24 V due to a relatively large dark current (collected from an area of i-InGaAs which is much wider than the square window opening). As the NIR input power density increased from 0.1 to 1 mW/mm^2, the values of the output luminance increased from 360 to 930 cd/m^2, clearly demonstrating the upconversion operation of the hybrid device at room temperature. This new structure allows us to pursue a pixelless upconversion imaging approach.

5.2.3 Hybrid Imaging Device

In section 5.2.2, a novel pixelless upconversion device based on the integration of an i-$In_{0.53}Ga_{0.47}As/C_{60}$ hybrid photovoltaic junction and an OLED was demonstrated. A same structure device with a larger size of 4×4 mm^2 is then fabricated for imaging test (Fig. 5.5) is fabricated as

imaing device. Compared to the p-i-n InGaAs/InP/OLED upconverter, the interconnection region of upconverter based on i-$In_{0.53}Ga_{0.47}As/C_{60}$ is completely depleted under operating bias, which can drastically reduce lateral carrier diffusion at the organic/inorganic interface while preserving effective electrical connection with OLED component.

The device characterizations include the proof-of-the-concept of room-temperature upconversion imaging operation, the measurement of upconversion efficiciency, and real-time optical upconversion imaging operation. The spatial resolution of this upconversion imaging device is analyzed by using a simplified model.

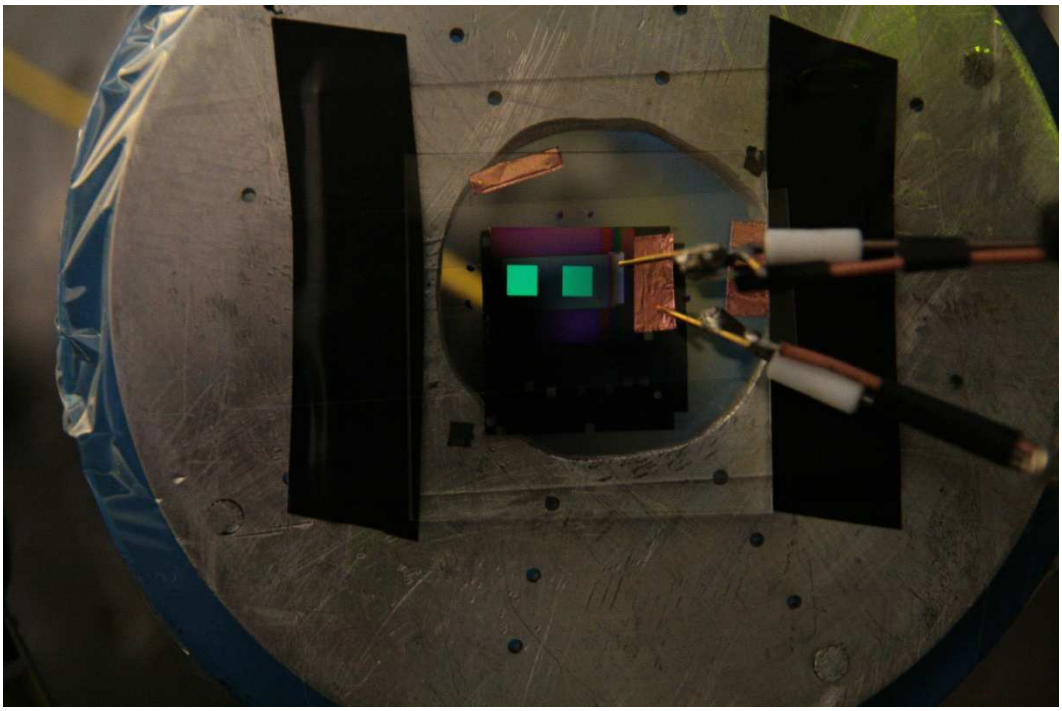

Figure 5.5 Working devices on the test stage.

The responsivity of the hybrid junction part and the OLED external power efficiency are obtained by measuring the photocurrent intensity (total current minus dark current) and OLED current-luminance efficiency of the integrated upconverters, respectively. Fig. 5.6 (a) shows the L-V curve of this upconversion device under 1.5-μm infrared illumination with 6 mW/cm^2 power density. To demonstrate the photovoltaic effect of $In_{0.53}Ga_{0.47}As/C_{60}$ junction, the total current of the working

device is measured with different input NIR power conditions [Fig. 5.6(b)]. Under dark conditions (no input NIR), the total current is very small at a bias of 8 V, then increases to 9 mA/cm^2 at bias of 16 V, indicating a substantial leakage current at higher reverse biases due to the large area of the device. Under NIR illumination, the total current of the device became evident at the bias of less than 4.0 V. As the NIR input power intensity increased from the 6 mW/cm^2 to 30 mW/cm^2, the total current values increased from 12.6 mA/cm^2 to 29 mA/cm^2, clearly demonstrating the photovoltaic effect of this larger-area hybrid junction. The overall external upconversion efficiency of this device is calculated to be ~0.57% W/W at a bias of 16 V (under 6 mW/cm^2 NIR illumination).

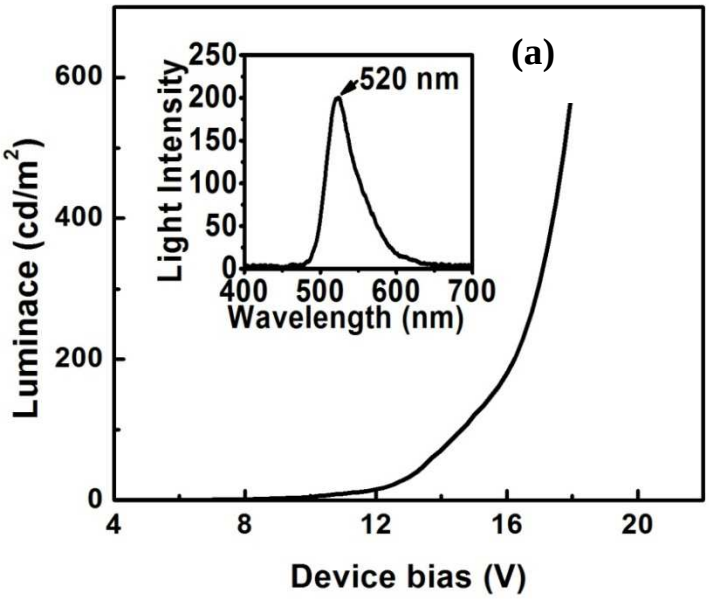

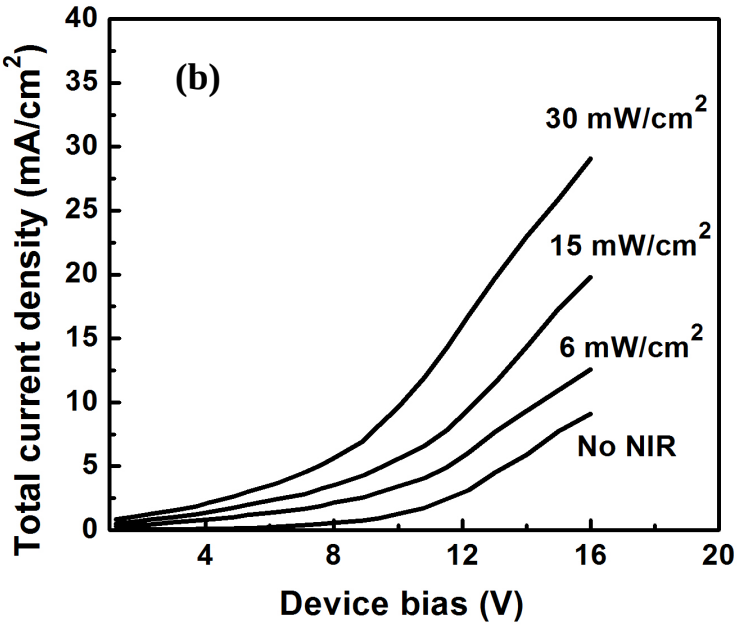

Figure 5.6. (a) Luminance-voltage (L-V) curve of upconverter under 1.5-μm infrared illumination with 6 mW/cm^2 power [inset: the emission spectrum from the OLED of the integrated upconverter peaked at 520 nm in wavelength (green light)]; (b) NIR-induced green light luminance as a function of device bias under different illumination conditions.

5.2.4 Upconversion Imaging Measurement System

To assess the pixelless imaging capability we use a back-to-back imaging setup (Fig. 5.7). Incoming 1.5-μm light is generated from high power laser diode. This laser output is first collimated to a uniform beam. This uniform laser beam passes the object aperture, so that the aperture is imaged onto the upconversion device. The output visible radiation is then collected by a Canon Macro Lens (EF 100mm) and re-imaged onto a digital camera, which is controlled by computer to capture, store, and manipulate the images (Fig. 5.8).

As for the laser system, a 1.5 W (working current =5A) high power infrared laser (SemiNex infrared laser) at a wavelength of 1.5 μm is selected. The reason to choose this high power laser is to obtain a better quality pattern image from the upconverter, due to the fact that infrared light input with higher power differentiates pattern from background light better. A heat-sink with an electric fan is deployed to cool down the laser in operation. The laser beam is stabilized in the experiment. The

lens and optical system are originally designed and deployed to yield a collimated infrared light beam with uniform distribution of light intensity.

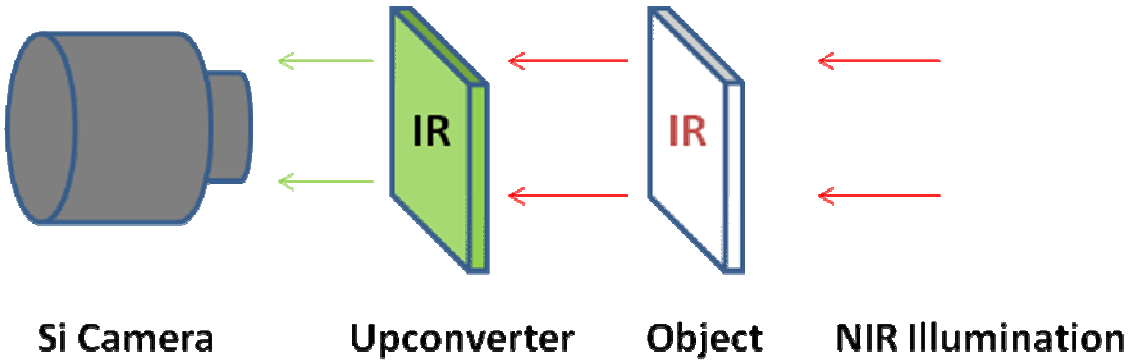

Figure 5.7 Schematic of setup for imaging test

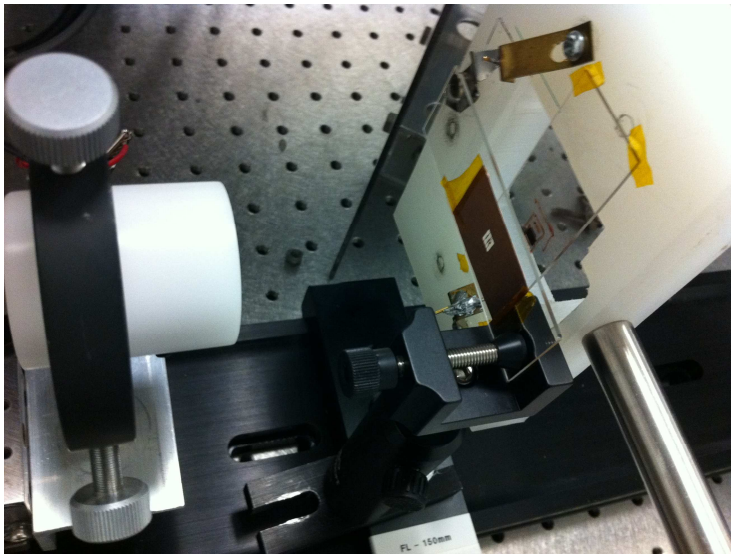

(a)

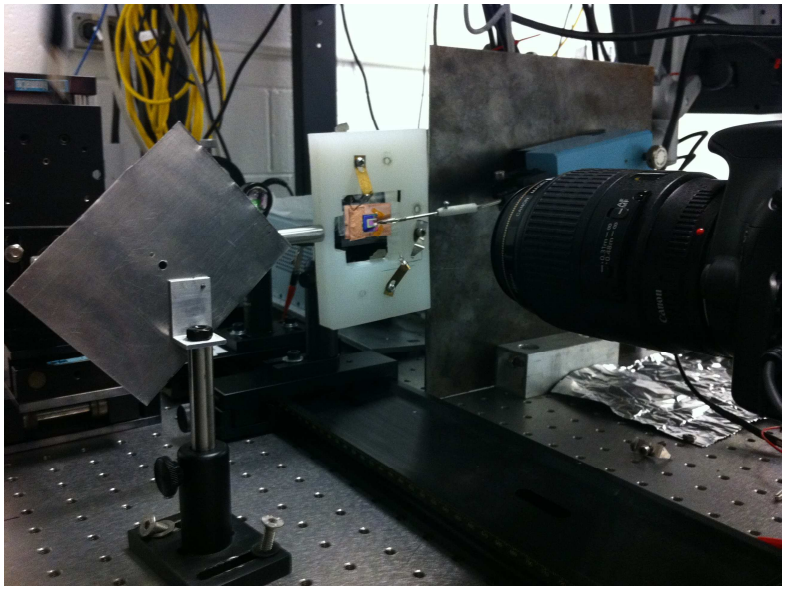

(b)

Figure 5.8 Imaging measurement setup (a) Laser and pattern, (b) Device and camera.

5.2.5 Pixelless Imaging Result

Fig. 5.9(a) is the image of the device biased at 10 V without NIR input, captured by the digital camera. The dark-current induced illumination is fairly uniform across the whole device area. Incoming 1.5-μm light is collimated (beam diameter ~ 2.1 mm) and shone onto the backside of the device. The output green radiation is captured from the top surface of the device [Fig. 5.9(b)]. Fig. 5.9(c) is the net upconverted image of the NIR laser beam by subtracting Fig. 5.9(a) from Fig. 5.9(b). Fig. 5.10 shows an example image that contains a letter “U” and is captured using the camera. When the device is negatively biased, images of the original apertures are clearly seen on the camera.

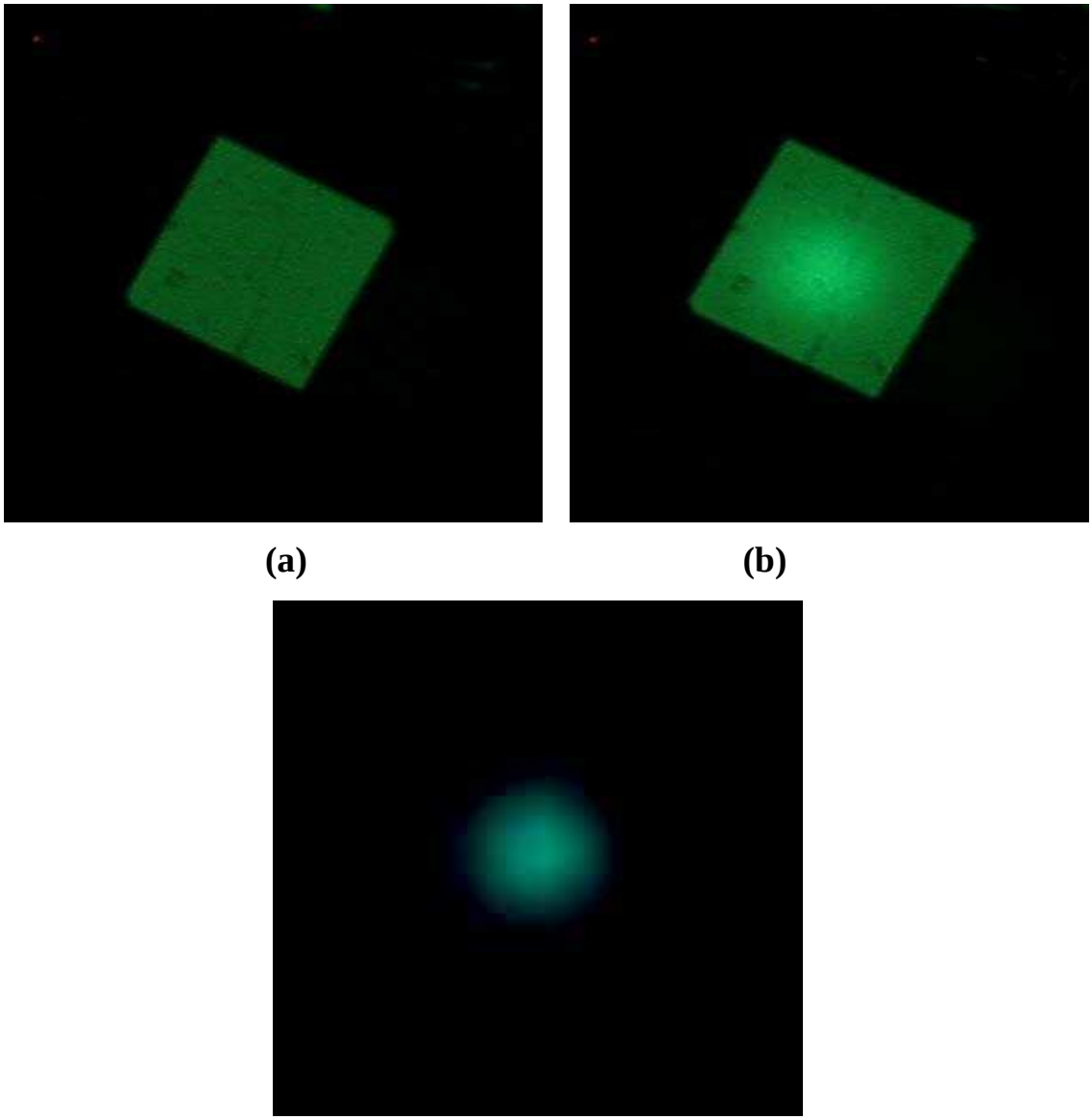

Figure 5.9 (a) A Camera captured image of the fabricated upconverter (4×4 mm^2) biased at 10 V in dark condition. The observed green illumination is from device dark current; (b) An output image of the upconverter under 1.5 µm NIR illumination from a NIR laser beam (beam diameter ~ 2.1 mm); (c) The net upconverted image of the NIR laser beam by subtracting (a) from (b).

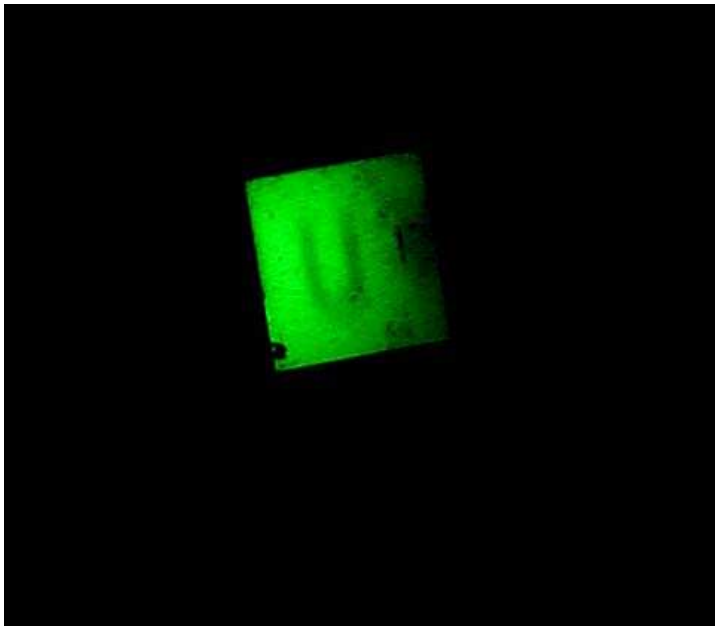

Figure 5.10 Camera image of letter “U” obtained from the pixelless upconversion device. The device is 4×4 mm^2 in size. The device was biased at -10 V at room temperature.

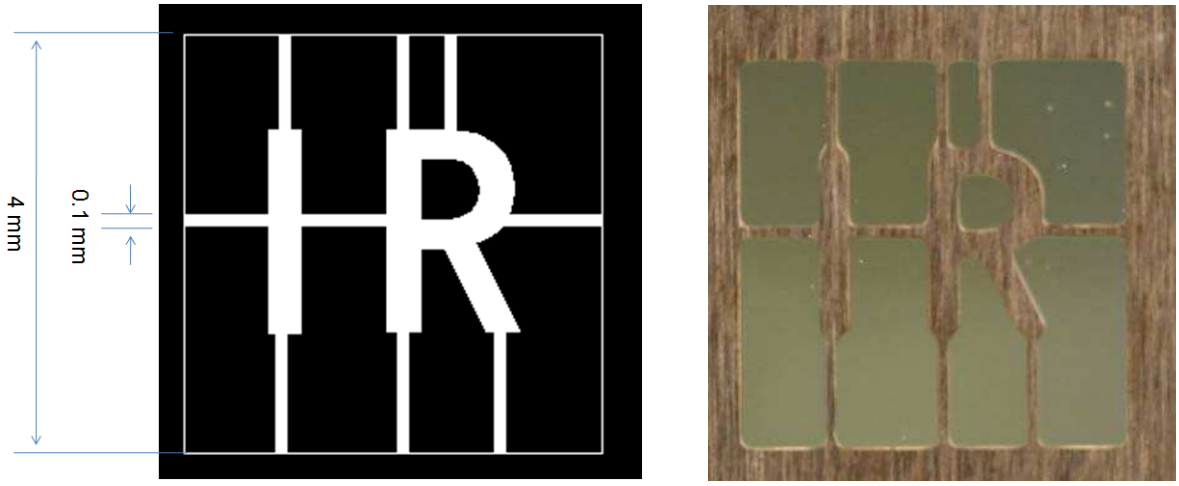

(a) **(b)**

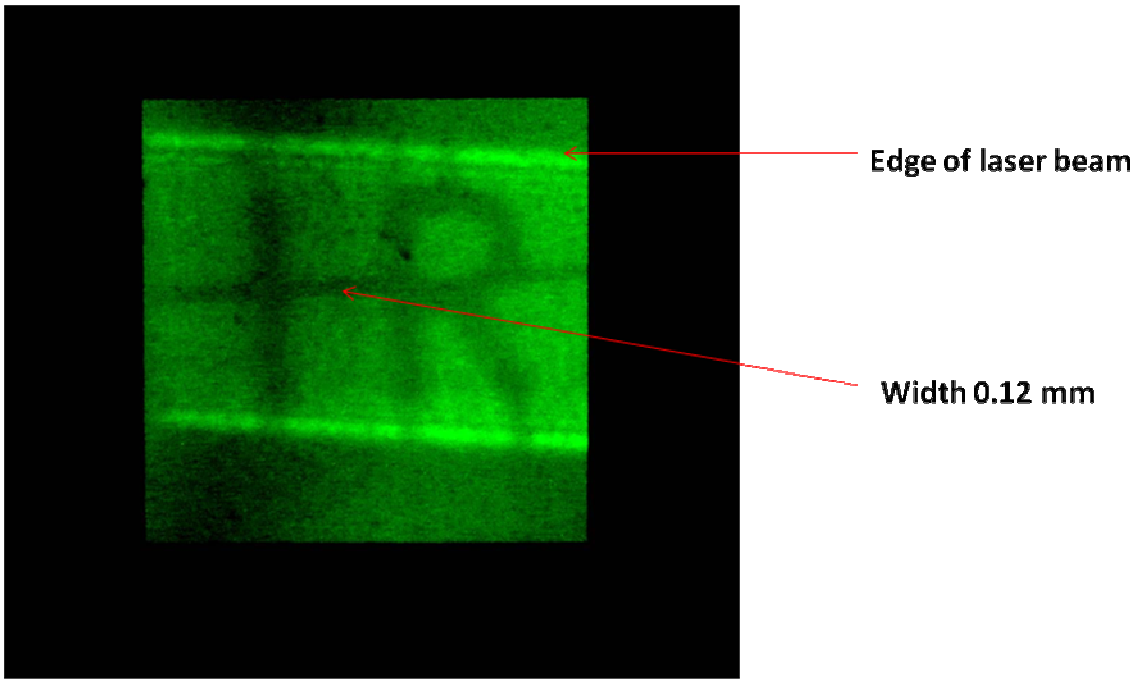

(c)

Figure 5.11 (a) The design file of characters "IR", (b) "IR" manufactured in the 0.2 mm thick brass sheet; (c) Near infrared image of letter "IR" obtained from the pixelless upconversion device. The device is 4×4 mm^2 in size. The device was biased at -10 V at room temperature.

For practical applications, the spatial resolution of the upconversion imaging devices is a critical parameter. To test the resolution, characters "IR" were designed with the smallest feature size of 0.1 mm, which was the connection between the small characters and the main sheet for easy manufacture [Fig.5.11(a)]. And then this design was made in the 0.2 mm thick brass sheet [Fig.5.11(b)]. For setup, the pattern was attached to the upconversion device back to back, which was still 4×4 mm^2 in size and was biased at -10 V at room temperature. From the Fig.5.11(c), the image exhibits good contrast for the letter to be easily recognized. The spatial resolution can be estimated using [(0.12 mm-0.1 mm)/2] = 10 µm, which was approaching the resolution limit of the camera here (7 µm). When the device bias was removed, the upconversion images disappeared. We therefore achieved room-temperature hybrid pixelless upconversion imaging operation by drastically suppressing the lateral carrier diffusion in the interconnection area while maintaining effective photovoltaic effect in

the hybrid junction in this proof of the concept organic/inorganic hybrid upconversion imaging device.

5.2.6 Theoretical Model

In the pixelless imaging device, there is no pixel structure to isolate the photogenerated current, so the spatial resolution will be limited by the current lateral spreading in the inorganic and organic layer. This section presents a theoretical study of the current diffusion inside the upconversion device. A schematic view and the operation principle of the pixelless imaging device are shown in Fig. 5.12. Infrared beam is illuminated from the bottom of device and absorbed along the *y* direction to generate electron-hole pairs. Under the applied bias, holes will move upward into the active region of OLED. To constrain the spatial distribution of the output photocurrent density reproducing the infrared image, the holes photoexcited from the *x* direction must be refrained to spread in the *x* direction during their drifting flow in the presence of the applied field.

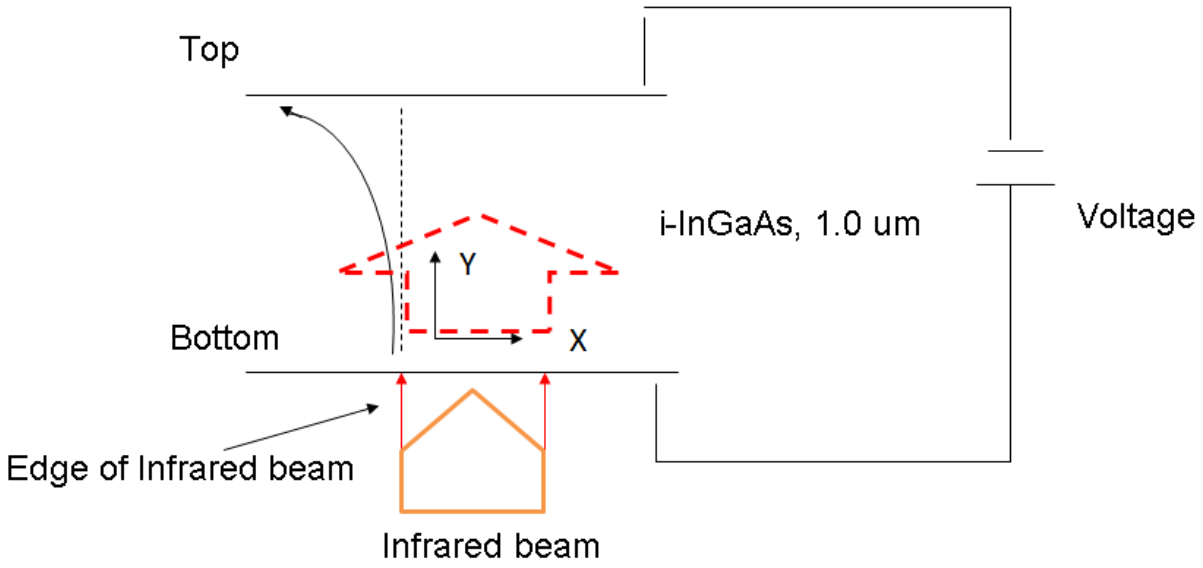

Figure 5.12 Schematic view of the pixelless imaging device

The hybrid i-$In_{0.53}Ga_{0.47}As/C_{60}$ junction operation is governed by the following processes: 1) photoexcitation of holes from the NIR absorption in intrinsic layer. 2) hole drift and diffusion in the direction of bias voltage 3) hole diffusion in the lateral plane (perpendicular to the bias field) (Fig. 5.12). The input light is assumed to be uniform and the two-dimensional equation is written as [58]

$$-\frac{\partial}{\partial y}(\upsilon_y P - D_y \frac{\partial P}{\partial y}) + D_x \frac{\partial^2 P}{\partial x^2} + G(y) - R = 0 \tag{5.2}$$

Here, υ_y is the hole saturation velocity in the direction of electrical field, D_y is the diffusion coefficients of the holes in the direction of electrical field and D_x the diffusion coefficiency in lateral plane, R is the carrier recombination rate and $G(x)$ is the rate of photoexcitation in the hybrid junction.

$$G(y) = \frac{P_{in}}{Ahv} \alpha e^{-\alpha y} \tag{5.3}$$

Here, P_{in} is the optical input power, A is device area, h is Planck's constant, v is the frequency of light, α is the absorption coefficient of $In_{0.53}Ga_{0.47}As$ (assumed to be 0.705 um^{-1} for this wavelength) [59].

The carrier generation-recombination process consists of Schokley-Read-Hall, Auger, radiative recombination terms. The equations are:

$$R^{SRH} = A(np - n_i^{\,2}) \tag{5.4}$$

$$R^{Auger} = (C_n n + C_p p)(np - n_i^{\,2}) \tag{5.5}$$

$$R^{SRH} = B(np - n_i^{\,2}) \tag{5.6}$$

Where A is the SRH recombination coefficient, C_n and C_p are the Auger recombination coefficients, and B is the Radiative recombination coefficient .

The numerical simulations have been performed with Sentaurus Device [60]. Fig. 5.13 shows the structure of the modeling device. The structure consists of a 0.5 µm heavily doped n-InP buffer layer, a 1 µm lighted doped n-type InGaAs absorption layer. The width of device, metal contact , input light beam, and bottom contact are 80 µm, 80 µm, 10 µm and 10 µm respectively. The input NIR light density is 10 mW/cm^2. A list of parameters used for the simulations is given in the Table 5.1.

Table 5.1 Parameters of InGaAs layer [61]

Parameters	***Units***	***InGaAs***
Band gap	eV	0.78
Hole mobility	cm^2/Vs	450
Electron SRH lifetime	s	1×10^{-6}
Hole SRH lifetime	s	1×10^{-6}
Electron Auger coefficient	cm^6/s	8.1×10^{-29}
Hole Auger coefficient	cm^6/s	8.1×10^{-29}
Radiative recombination coefficient	cm^3s^{-1}	1.43×10^{-10}

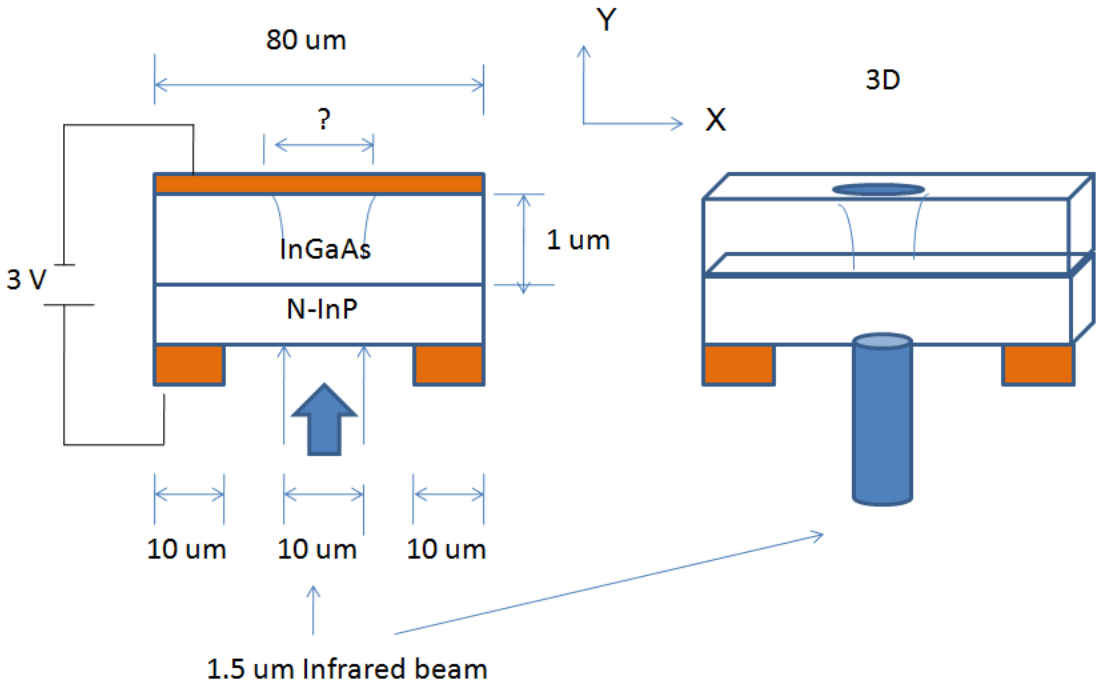

Figure 5.13 The structure of device model

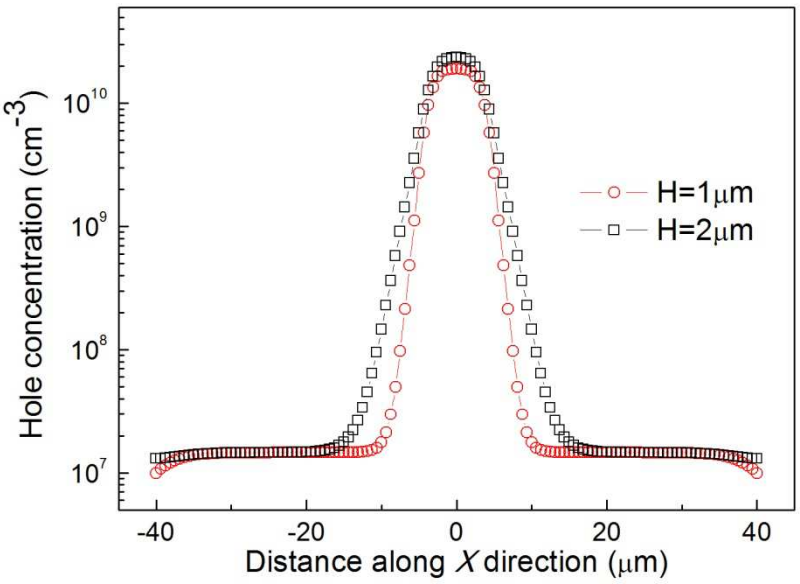

Figure 5.14 Photo-generated hole concentration on the top surface of InGaAs with different thickness (1 μm and 2 μm)

Fig. 5.14 shows the holes distribution on the top surface of the InGaAs (*x* direction) with different absorption layer thickness (1 μm, 2 μm). In the center of InGaAs surface (*x*=0), the hole concentration of device structure with 2 μm absorption layer is higher than that of device with 1 μm absorption layer, which is due to the fact that more injected infrared light is tansferred to generate photocarriers. The edge of hole spreading profile is also wider in the device with 2 μm thick InGaAs layer.

For more accurate evaluation, the edge of hole spreading (*x*) can be defined by the following equation

$$\frac{P_x}{P_0} = \frac{1}{10} \qquad (5.7)$$

Where, P_0 is the hole concentration at x=0, and P_x is the hole concentration at the edge. Under the same injection laser beam, the width of hole concentration profile is 11 μm for 1 μm thick InGaAs, but 12.5 μm for 2 μm thick InGaAs.

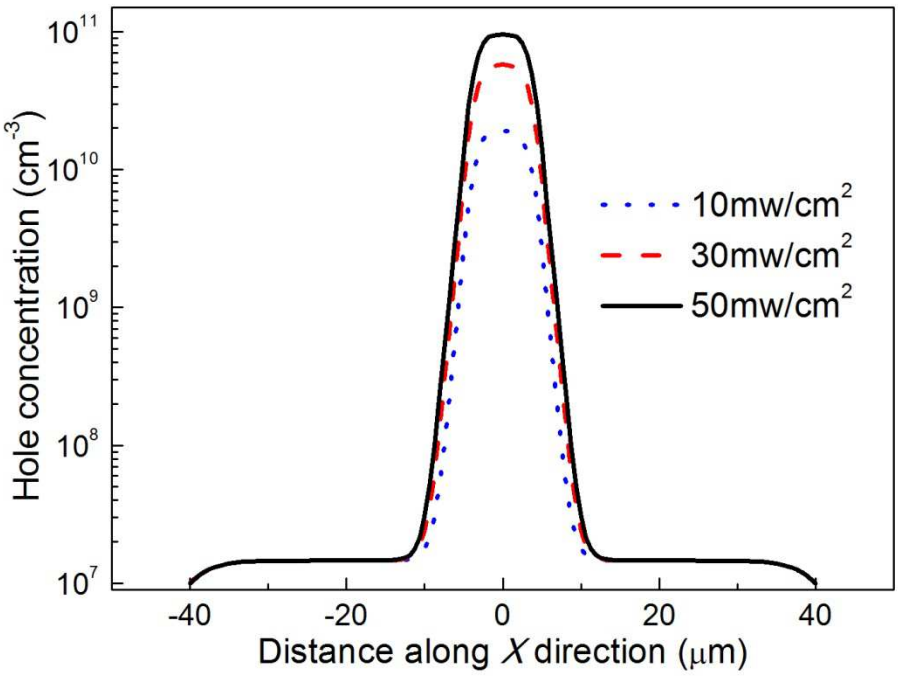

Figure 5.15 Photo-generated hole concentration on the top surface of InGaAs under different laser power densities (10 mW/cm^2, 30 mW/cm^2 and 50 mW/cm^2)

Table 5.2 Width of hole concentration profiles of laser beam with different density

Laser beam size	*Laser power density*	*Width of hole distribution profile*
10 μm	10 mW/cm^2	0.5 μm
10 μm	30 mW/cm^2	0.5 μm
10 μm	50 mW/cm^2	0.5 μm

To find the relationship of lateral spreading with respect to the laser power density, Fig. 5.15 shows the simulated result under different NIR laser illumination density (10 mW/cm^2, 30 mW/cm^2 and 50 mW/cm^2), the other device parameters are referred to Fig. 5.13. From this graph, the input laser power density affects the hole concentration in the centre area (x=0). if the edge of hole spreading profile is defined as the equation (5.7), the width of hole distribution profile of the three

curves are of the same value (Table 5.2). From the simulated result in Fig. 5.14 and 5.15, the spreading is mainly controlled by absorption layer thickness. With the 1 µm thick InGaAs layer, the spreading distance is calculated to be (11 µm-10 µm)/2= 0.5 µm.

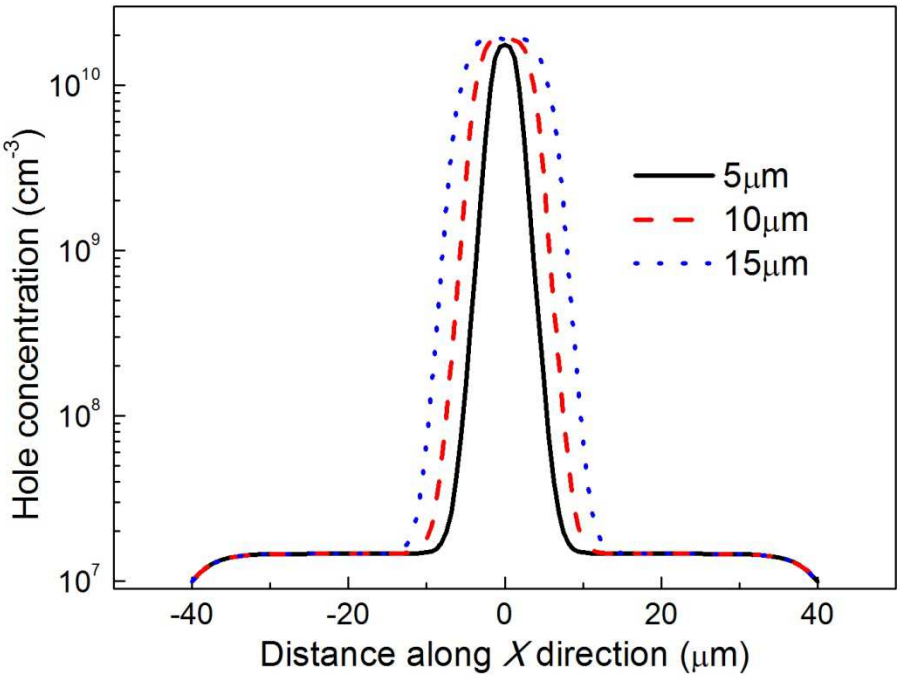

Figure 5.16 Photo-generated hole concentration on the top surface of InGaAs with laser beam sizes (5 µm, 10 µm and 15 µm)

Fig. 5.16 shows the hole distribution at the surface of InGaAs layer for different laser beam sizes (5 µm, 10 µm and 15 µm), the other parameters are as same as the model in Fig. 5.13. From this graph, the curve is almost shifting in *x* direction with the increase of laser beam size, and the spreading distance is the same with different laser beam size.

The holes passed the InGaAs layer are injected into OLED active layer. The potential hole lateral diffusion in the interfacial layer of C_{60} and CuPc may also lead to an additional smearing of the outgoing image. Due to the low mobility of C_{60} ($< 1\times10^{-4}$ cm^2/Vs) and CuPc layers ($< 1\times10^{-2}$ cm^2/Vs) and the very thin thickness (~100-200 nm), the lateral spreading in organic layer should be negligible [62-63].

However, the experimental resolution (10 μm) is larger than the theoretical prediction. The possible reasons could be the resolution limit of the digital camera and light scattering in the interface and interfacial states in the InGaAs/C_{60} junction. Photocarrier may be trapped at the interface and diffuse laterally, which could enhance the lateral diffusion. To optimize the device performance, different inorganic/organic heterojunctions and surface treatments can be analyzed to reduce the interface state. Secondly, light scattering due to the roughness of object, unpolished wafer substrate backside and OLED index mismatch should be minimized.

5.3 Conclusion

NIR hybrid pixelless device has been designed and demonstrated to capture the image of NIR laser beam and letters. This device is fabricated by direct tandem integration of an OLED with an i-InGaAs/C_{60} junction and an easily recognized image with the spatial resolution up to 10 μm is obtained. These experimental results show that the lateral carrier diffusion is successfully suppressed. In this chapter, the lateral photo-carrier diffusion inside the upconversion device is theoretically simulated and the simulation result shows the spreading distance in the InGaAs absorption layer can be controlled within 1 μm. In addition, due to the low mobility and very thin layer thickness, the carrier spreading inside the organic layers should be much lower than the carrier spreading in the InGaAs layer. These results show this i-InGaAs/ C_{60} heterojunction has great potentials for practical pixelless NIR imaging application and explore the utility of organic/inorganic hybrid semiconductor system in low cost and large area imaging devices.

Chapter 6
Summary and Contribution

Up-converting light from infrared bands to shorter wavelengths using compact structures has been attracting research interest. Near infrared optical upconverters in the eye-safe region around 1.5 µm are of particular interest because of their many potential applications, such as night vision, range finding, homeland security and semiconductor wafer inspection. Organic/inorganic hybrid up-conversion device is made by direct tandem integration of an inorganic InGaAs/InP Photodetector with an OLED. This device converts infrared light in the eye-safe region at 1.5 µm in wavelength to visible light, depending on different organic emissive materials used. This thesis work is summarized on the following aspects:

New device design is used to improve upconversion efficiency. Novel organic/inorganic hybrid devices with an embedded metal has successfully been designed and fabricated. The device was fabricated by direct tandem integration of an OLED with an inorganic InGaAs/InP p-i-n Photodetector. Efficient carrier injection from the inorganic Photodetector to the OLED was achieved by the insertion of a thin Au metal embedded mirror at the inorganic-organic interface. The upconversion efficiency was improved by more than 100%. The optimization of the embedded metal mirror structure of the hybrid devices lowered the turn-on voltage.

The overall upconversion efficiency can also be increased significantly, by introducing a gain mechanism into the photodetector section of the upconverter. A promising option to implement gain is a HPT. We integrated InGaAs-InP HPT with an OLED, which converts 1.5-µm Infrared light to visible light with a built-in electrical gain (~15). Further improvement based on new HPT design has been achieved recently with an electrical gain of 94. The overall upconversion efficiency is up to 1.55 W/W. This device functions not only as a wavelength converter, but also as an optical amplifier.

The demonstration of high performance 1.5 µm imaging devices is important for many military and civilian applications. With our upconversion approach, a NIR imaging device can be realized by using a single-mesa large-area pixelless imaging device, which doesn't need pixel array and therefore simplifies the device fabrication. The OLED output is spatially correlated with the input 1.5 µm scene and the lateral carrier diffusion is suppressed. The first organic/inorganic hybrid pixelless imaging with a function of converting infrared image to visible image was demonstrated with the spatial

resolution up to 10 μm. The lateral photocarrier diffusion was also theoretically simulated by 2D model.

List of Publications

Refereed Journal Publications:

1. J. Chen et al. " Organic/inorganic near-infrared pixelless imaging device", In preparation
2. Jianchen Tao, J. Chen, D. Ban, M. G. Helander and Z. Lu, "Infrared optical up-conversion devices", *Science of Advanced Materials*, In press (2011)
3. J. Chen, D. Ban, M. G. Helander, Z. Lu, and P. Poole, "Near-infrared inorganic/organic optical upconverter with an external power efficiency of >100%" *Advanced Materials*, vol.22, no.43, 4900-4904 (2010).
4. J. Chen, D. Ban, M. G. Helander, Z. Lu, M. Graf, P. Poole and H. C. Liu, "Near-infrared optical upconverter with integrated heterojunction phototransistor and organic light-emitting diode" *IEEE Photon. Technol. Lett.*, vol.21, no.19, 1447-1449 (2009).
5. J. Chen, D. Ban, M. G. Helander, Z. Lu, M. Graf, A. J. SpringThorpe and H. C. Liu, "Near infrared optical upconverter based on i-$In_{0.53}Ga_{0.47}As/C_{60}$ photovoltaic heterojunction" *Electron. Lett.*, vol.45, no.14, 753-755 (2009).
6. J. Chen, D. Ban, X. Feng, Z. Lu, S. Fathololoumi, A.J.SpringThorpe, H. C. Liu, "Near-infrared inorganic/organic hybrid optical upconversion device with an embedded mirror", *Physica Status Solidi C* 6, no.S1, S23-26 (2009).
7. J. Chen, D. Ban, X. Feng, Z. Lu, S. Fathololoumi, A.J.SpringThorpe, H. C. Liu, "Enhanced efficiency in near-Infrared inorganic/organic hybrid upconverter with an embedded mirror", *J.Appl.Phys.*, vol.103, no.10, 103112-1-5 (2008).

Refereed Conferences Presentations:

1. J. Chen, J. Tao, D. Ban, M. G. Helander, Z. Wang, J. Qiu and Z. Lu, "Organic/Inorganic Hybrid Pixelless Near Infrared Imaging Device," *Submitted to CLEO*-2012, San Jose, USA.
2. J. Chen, D. Ban, M. G. Helander, Z. Lu, P. Poole, "Organic/Inorganic Hybrid Optical Amplifier with Wavelength Conversion," *CLEO*-2011, May 1-6, 2011, Baltimore, USA.
3. J. Chen, D. Ban, M. G. Helander, Z. Lu, P. Poole, H. C. Liu, "Hybrid infrared optical upconversion devices with a built-in electrical gain," *SPIE Defense, Security, and Sensing* 2010, April 5-9, Orlando, FL, USA.
4. D. Ban, J. Chen, M. G. Helander, Z. Lu, M. Graf, A. J. SpringThorpe, P. Poole, H. C. Liu, "Infrared organic/inorganic optical upconverting devices," (invited), *SPIE ISPDI-2009*, June 17-19, 2009, Beijing, China.

5. J. Chen, D. Ban, M. G. Helander, Z. Lu, M. Graf, A. J. SpringThorpe, H. C. Liu, "Near Infrared optical upconverter based on i-$In_{0.53}Ga_{0.47}As/C_{60}$ Photovoltaic junction," *CLEO* 2009, May 31-Jun 05, 2009, Baltimore, USA.
6. J. Chen, D. Ban, X. Feng, Z. Lu, S. Fathololoumi, A.J.SpringThorpe, H. C. Liu, "Near-infrared inorganic/organic hybrid optical upconversion device with an embedded mirror", oral presentation in *ICOOPMA-2008*, July 20-25, 2008, Edmonton, Canada.

Patent

Dayan Ban, Zheng-hong Lu and Jun Chen,"Organic/Inorganic Hybrid Optical Amplifier with Wavelength Conversion", *US Provisional Patent*, Filed in Aug.2010.

Bibliography

[1] “Infrared Study Press Release” Jan.4, 2011. [Online]. Available:

http://www.flowresearch.com/Press_Releases/Website/InfraredStudyRelease.htm

[2] H. Luo, D. Ban, H. C. Liu, P. J. Poole, and M. Buchanan, “Pixelless imaging device using optical upconverter,” IEEE Electron Device Letters, vol. 25, pp. 129, 2004.

[3] D. Ban, H. Luo, H. C. Liu, A. J. SpringThorpe, R. Glew, Z. R. Wasilewski, and M. Buchanan, “ 1.5 to 0.87 μm optical upconversion device fabrication by wafer fusion,” Electronics Letters, vol. 39, pp. 1145, 2003.

[4] D. Ban, H. Luo, H. C. Liu, Z. R. Wasilewski, A. J. SpringThorpe, R. Glew, and M. Buchanan, “ Optimized GaAs/AlGaAs light-emitting diodes and high efficiency wafer-fused optical up-conversion devices,” J. Appl. Phys., vol. 96, pp. 5243, 2004.

[5] D. Ban, H. Luo, H. C. Liu, Z. R. Wasilewski, and M. Buchanan, “ Pixelless 1.5 μm up-conversion imaging device fabricated by wafer fusion,” IEEE Photonics Technology Letters, vol. 17, pp. 1477, 2005.

[6] M. Dutta, and M. A. Stroscio “Advanced semiconductor heterostructures”, World Scientific Publishing, pp.32, 2003.

[7] S.M.Sze, “ Physics of semiconductor devices”, 2rd Edition, Wiley Publishing, 1981.

[8] J. Piotrowski, and W. Gawron “ Ultimate performance of infrared photodetectors and figure of merit of detector material”, Infrared of Physics & Technology, vol.38, pp.63, 1997.

[9] A. Rogalski, “Quantum well photoconductors in infrared detector technology”, J. Appl. Phys. vol.93, pp.4355, 2003.

[10] I. M. Baker, and C. D. Maxey, “ Summary of HgCdTe 2D array technology in the UK”, J. Electron. Mater. vol.30, pp.682, 2003.

[11] D. Vennerberg, and Z. Lin, “Upconversion nanocrystals: Synthesis, properties, assembly and applications,” Science of Advanced Materials, vol.3, pp. 26, 2011.

[12] B. M. van der Ende, L. Aarts, and A. Meijerink, “Lanthanide ions as spectral converters for solar cells,” Physical Chemistry Chemical Physics, vol.11, pp. 11081, 2009.

[13] H.C. Liu, J. Li, Z.R.Wasilewski, and M.Buchan, “Integrated quantum well intersubband photodetector and light-emitting diode forthermal imaging,” SPIE, vol. 2552, pp. 336, 1995.

[14] H. Liu, M. Gao, and P. Poole, “1.5 μm up-conversion device”, Electronics Letters, vol.36, pp.1300, 2000.

[15] H. C. Liu, H. Luo, D. Ban, M. Buchanan, Z. R. Wasilewski, A. J. SpringThorpe, and P. J. Poole "Photon upconversion devices for imaging", Proceeding of SPIE, vol.6984, pp. 698431. 2008.

[16] H.C. Liu, L.B.Allard, M. Buchanan, Z.R. Wasilewski, “Pixelless infrared imaging device”, Electron.Lett.vol.33, pp.379, 1997.

[17] G. D. Zhou, “Fundamentals of Structural Chemistry”, World Scientific, 1993.

[18] http://www.orgworld.de/

[19] M. Pope, and C. E. Swenberg, “Electronic Processes in Organic Crystals and Polymer”, 2nd ed., New York: Oxford University Press, 1999.

[20] A. G. Brian, and C. H. Mark, “Comparing organic to inorganic photovoltaic cells: Theory, experiment, and simulation,” J. Appl. Phys., vol.93, pp. 3605, 2003.

[21] M. Cooke, “Excitonic prospects for UV,” III-Vs Review, vol.19, pp. 22. 2006.

[22] M.Pope, H.P. Kallmann and P. Magnante, “Electroluminescence in Organic Crystals,” J. Chem. Phys. vol.38, pp.2042, 1963.

[23] C.W.Tang and S.A. VanSlyke, “Organic electroluminescent diodes”, Appl. Phys. Lett., vol. 51, pp.913, 1987.

[24] H. Aziz, Z.D. Popovic, N. Hu, A. Hor, and G. Xu, “Degradation mechanism of small molecule-based organic light-emitting devices,” Science, vol. 283, pp.1900, 1999.

[25] H. Aziz, Y. Luo, G. Xu, and Z.D. Popovic, “Improving the stability of organic light-emitting devices by using a thin Mg anode buffer layer,” Appl. Phys. Lett. ,vol. 89, pp.103515, 2006.

[26] S.VanSlyke, C. Chen and C. Tang, “Organic electroluminescent devices with improved stability,” Appl.Phys.lett. vol.69, pp.2160, 1996.

[27] M. Mason, C.Tang, L.Hung, P.Raychaudhuri, J.Madathil, D. Giesen, L. Yan, Q.Le, Y. Gao, S. Lee, L. Liao, L. Cheng, W. Salaneck, D. Santos, and J. Bredas, “Interfacial chemistry of Alq_3 and LiF with reactive metals,” J. Appl. Phys., vol. 89, pp.2756, 2001.

[28] D.Grozea, A. Turak, X.Feng, Z. Lu, D. Johnson and R. Wood, “Chemical structure of Al/LiF/Alq interface in organic light-emitting diodes,” Appl. Phys. lett. vol.81, pp.3173, 2002.

[29] J. Ni, T. Tano, Y. Ichino, T. Hanada, T. Kamata, N. Takada, K. Yase, “ Organic light-emitting diode with TiOPc layer-a new multifunctional optoelectronic device,” Jpn. J. Appl. Phys., vol.40, pp.948, 2001.

[30] M. Chikamatsu, Y. Ichino, N. Takada, M. Yoshida, T. Kamata, K. Yase, “Light upconversion from near-infrared to blue using a photoresponsive organic light-emitting device,” Appl. Phys. Lett. , vol. 81, pp.769, 2002.

[31] D. Y. Kim, D. W. Song, N. Chopra, P. D. Somer, and F. So, “Organic infrared upconversion device,” Adv. Mater. , vol.22, pp. 2260, 2010.

[32] T. Rauch, M. Boberl, S. F. Tedde, J. Furst, M. V. Kovalenko, G. Hesser, U. Lemmer, W. Heiss and O. Hayden, “Near-infared imaging with quantum-dot-sensitized organic photodiodes,” Nat. Photonics, vol. 3, pp.332. 2009.

[33] P. Peumans, S. Uchida and S. R. Forrest, “Efficient bulk heterojunction photovoltaic cells,” Nature vol.425, pp.158, 2003.

[34] W. U. Huynh, J. J. Dittmer and A. P. Alivisatos,“ Hybrid nanorod-polymer solar cells,” Science , vol.295, pp. 2425, 2002.

[35] L. Wang, Myung-Han Yoon, Gang Lu, Yu Yang, Antonio Facchetti and Tobin J. Marks, “High-performance transparent inorganic-organic hybrid thin-film n-type transistors,” Nature Materials vol.5, pp.893, 2007.

[36] A. J. Steckl, J. Heikenfeld and S. C. Allen “Hybrid inorganic/organic light emitting materials and devices for displays and lighting,” Electroluminescence 2004, Toronto, Sept. 2004

[37] G. Cherkashinin, S. Krischok, M. Himmerlich, O. Ambacher and J. A. Schaefer "Electronic properties of C60/InP(001) heterostructures" J. Phys.: Condens. Matter, vol.18,pp. 9841, 2006

[38] D. Ban, S. Han, Z. Lu, T. Oogarah, A. J. SpringThorpe and H. C. Liu, “Near-infrared to visible light optical upconversio by direct tandem integration of organic light-emitting diode inorganic photodetector,” Appl. Phys. Lett., vol. 90, pp.093108, 2007.

[39] D. Ban, S. Han, Z. Lu, T. Oogarah, A. J. SpringThorpe and H. C. Liu, “Organic-inorganic hybrid optical upconverter,” IEEE Transaction on Electronic Devices, vol.54, pp.1645, 2007.

[40] Xiaodong Feng, “Development of 8-Hydroxyquinoline metal based organic-light emitting diodes” , PhD thesis, University of Toronto, 2008.

[41] L. Chang, C. Shiue, and M. Jeng, " High reflective p-GaN/Ag/Ti/Au Ohmic contacts for flip-chip light emitting diode (FCLED) applications", Applied Surface Science, vol.255, pp.6155, 2009.

[42] S. Han, Y. Yuan, and Z. H. Lu, "Highly-efficient organic light-emitting diodes with Metal/Fullerene anode," J. Appl. Phys., vol.100, pp.074504, 2006.

[43] V. Bulovic, V. B. Khalfin, G. Gu, P. E. Burrows, D. Z. Garbuzov, and S. R. Forrest, "Weak microcavity effects in organic light-emitting devices," Phys. Rev. B vol.58, pp.3730, 1998.

[44] G. D. Henshall, P. D. Greene, W. O. Bourne, D. R. P. Guy, D. D. Besgrove, N. Apsley, L. L. Taylor and S. J. Bass, " A 5×5 monolithic InGaAs/InP multiple quantum well spatial light modulator array," Semicond. Sci. Technol., vol. 5, pp.512, 1990.

[45] H. Kim, H. Kanjo, S. Tamura, and S. Arai, "1.5-m-wavelength distributed feedback lasers with deeply etched first-order vertical grating," Jpn. J. Appl. Phys. vol.41, pp. 7396, 2002.

[46] H. Luo, D. Ban, H. C. Liu, Z. R. Wasilewski and M. Buchanan, "Optical upconverter with integrated heterojunction phototransistor and light-emitting diode", Appl. Phys. Lett., vol. 88,pp. 073501, 2006.

[47] M. Lunardi, S. Chandrasekhar, and R. A. Hamn, "High-speed, High-Current-Gain P-n-p InP/InGaAs Heterojunction Bipolar Transistors," IEEE Electron Device Lett. vol.14, pp.19, 1993.

[48] Y. C. Jo, S. J. Joe, H. Kim, and P. Choi, "Optical Characteristics of Responsivity-Enhanced InGaAs/InP Heterojunction Phototransistors," Jpn. J. Appl. Phys. vol.44, pp.2537, 2005.

[49] K. P. Kim, K. S. Lee, T. W. Kim, D. H. Woo, J. H. Kim, J. H. Seo and Y. K. Kim, "Enhancement of the light extraction efficiency in organic light emitting diodes utilizing a porous alumina film," Thin Solid Films vol. 516, pp.3633, 2008.

[50] T. Moriizumi, and K. Takahashi, "Theoretical analysis of heterojunction phototransistors," IEEE Trans. Electron. Dev. vol.19, pp.152.1972.

[51] M. Konagai, K. Katsukawa, and K. Takahashi, " GaAlAs/GaAs heterojunction phototransistor with high current gain," J. Appl. Phys., vol.48, pp.4389, 1977.

[52] L. Y. Leu, J. T. Gardner, and S. R. Forrest, "A high-gain, high-bandwidth $In_{0.53}Ga_{0.47}As$/InP heterojunction phototransistor for optical communication," J. Appl. Phys., vol.69, pp.1052, 1991.

[53] SimWindows semiconductor device simulator (http://www.simwindows.com).

[54] D. Y. Kim, K. R. Choudhury, J. W. Lee, D. W. Song, G. Sarasqueta, P. D. Somer, and F. So, " PdSe nanocrystal-based infrared-to-visible up-conversion device". Nano letter, vol.11, pp.2109, 2011.

[55] E. Lee " Simulation of the thin-film thicknes distribution for an OLED thermal evaporation process," Vacuum, vol.83, pp.848, 2009.

[56] Kojima N., Yamaguchi M. and Ishikawa N.:" Analysis of Photovoltaic properties of C_{60}-Si heterojunction solar cells," Japn.J. Appl.Phys., Part 1, vol.39, pp.1176, 2000.

[57] Cho S., Yoo K., Jeong K., Whang C., Yi Y. and Noh M.: "Interfacial electronic structure of N, N'-bis(1-naphthyl)-N, N'-diphenyl-1, 1'-biphenyl-4, 4'-diamine/copper phthalocyanine:C_{60} composite/Au studied by ultraviolet photoemission spectroscopy," Appl. Phys. Lett., vol.91, pp. 052102, 2007

[58] V. Ryzhii, H.C. Liu, I. Khmyrova, M. Ryzhii, "Analysis of integrated quantum-well infrared photodetector and light-emitting diode for implementing pixelless imaging devices", IEEE Journal of quantum electronics, vol. 33, pp.1527, 1997.

[59] X. G. Zheng, J. Hsu, X. Sun, J. B. Hurst, X. Li, S. Wang, A. L. H. Jr., J. C. Campbell, A. S. Huntington, and L. A. Coldren, " A 12×12 InGaAs-InAlAs Avalanche Photodiode Array", IEEE J.Quantum Electron., vol.38, pp1536, 2002.

[60] Synopsys Sentaurus Device Simulation , USA 2008

[61] X.D.Wang, W.D. Hu, X. S. Chen, W. Lu, H. J.Tang, T.Li, and H.M. Gong, " Dark current simulation of InP/$In_{0.53}Ga_{0.47}As$/InP p-i-n photodiode", Opt. Quant Electron, vol.40, pp.1261, 2008.

[62] R. Konenkamp, G. Priebe, and B. Pietzak, " Carrier mobilities and influence of oxygen in C_{60} films. Phys. Rev. B, vol. 60, pp.11804, 1999.

[63] M. Ofuji, K. Ishikawa, H. Takezoe, K. Inaba, and K. Omote, "Phthalocyanine thin film field effect transistors," Appl. Phys. Lett., vol.86, pp.062114, 2005.